2007

# The study of electromagnetic wave propagation in photonic crystals via planewave based transfer (scattering) matrix method with active gain material applications

Ming Li
*Iowa State University*

# The study of electromagnetic wave propagation in photonic crystals via planewave based transfer (scattering) matrix method with active gain material applications

by

**Ming Li**

A dissertation submitted to the graduate faculty
in partial fulfillment of the requirements for the degree of
DOCTOR OF PHILOSOPHY

Major: Condensed Matter Physics

Program of Study Committee:
Kai-Ming Ho, Major Professor
Gary Tuttle
Jianwei Qiu
Joseph Shinar
Joerg Schmalian

Iowa State University
Ames, Iowa
2007

To my grand father and grand mother

# Table of Contents

## Acknowledgments

Six years have been passed since my first day at the lovely mid-west small town Ames, and twelve years since my first day at Department of Physics, Xiamen University. It is so long and lonely journey to reach the goal that it is mission impossible without my family's financial and spiritual supports. I am grateful in heart to my grandparents, parents and aunt.

During my PhD study at Iowa State University, my adviser Dr. Kai-Ming Ho gives me enormous help and valuable advices not only in academic research but also in personal life. I have learnt a lot from his deep understanding and sharp vision at photonic crystal research fields, as well as his broad knowledge at other areas. Here I would like to sincerely thank him.

Also during my PhD study, I learnt a lot from my study committee faculties: Dr. Joerg Schmalian taught me four graduate courses which made the foundation of my physics knowledge; Dr. Gary Tuttle taught me one graduate course and many microwave experiments skills; Dr. Joseph Shinar's OLED presentations gave me a lot of hints for applications of my research; and Dr. Jianwei Qiu's advices made me think deeper and more fundamental in the theory of my research. I would like to thank my study committee members for their help. I would also like to thank Dr. Dave Turner for valuable discussion and help at parallel computation.

Sometimes doing research is frustrating, and you will need buddies to back you up. Dr. Jiangrong Cao (*Canon USA*) and Dr. Xinhua Hu (*Ames Lab*) are two such good buddies to discuss with. Their help and friendship are very important to me; and the TMM/GTMM package will not be possible to finish without their help. Last I would like to thank all my friends at Ames who make my life not so boring, especially my girl friend Ruixue who always encourages me and supports my study.

This work was performed at Ames Laboratory under Contract No. DE-AC02-07CH11358 with the U.S. Department of Energy. The United States government has assigned the DOE Report number IS-T 2889 to this thesis.

## Abstract

In this dissertation, a set of numerical simulation tools are developed under previous work to efficiently and accurately study one-dimensional (1D), two-dimensional (2D), 2D slab and three-dimensional (3D) photonic crystal structures and their defects effects by means of spectrum (transmission, reflection, absorption), band structure (dispersion relation), and electric and/or magnetic fields distribution (mode profiles). Further more, the lasing property and spontaneous emission behaviors are studied when active gain materials are presented in the photonic crystal structures. Various physical properties such as resonant cavity quality factor, waveguide loss, propagation group velocity of electromagnetic wave and light-current curve (for lasing devices) can be obtained from the developed software package.

First, the planewave based transfer (scattering) matrix method (TMM) is described in every detail along with a brief review of photonic crystal history (Chapter 1 and 2). As a frequency domain method, TMM has the following major advantages over other numerical methods: (1) the planewave basis makes Maxwell's Equations a linear algebra problem and there are mature numerical package to solve linear algebra problem such as Lapack and Scalapack (for parallel computation). (2) Transfer (scattering) matrix method make 3D problem into 2D slices and link all slices together via the scattering matrix ( **S** matrix) which reduces computation time and memory usage dramatically and makes 3D real photonic crystal devices design possible; and this also makes the simulated domain no length limitation along the propagation direction (ideal for waveguide simulation). (3) It is a frequency domain method and calculation results are all for steady state, without the influences of finite time span convolution effects and/or transient effects. (4) TMM can treat dispersive material (such as metal at visible light) naturally without introducing any additional computation; and meanwhile TMM can also deal with anisotropic material and magnetic material (such as perfectly matched layer) naturally from its algorithms. (5) Extension of TMM to deal with

active gain material can be done through an iteration procedure with gain material expressed by electric field dependent dielectric constant.

Next, the concepts of spectrum interpolation (Chapter 3), higher-order incident (Chapter 4) and perfectly matched layer (Chapter 5) are introduced and applied to TMM, with detailed simulation for 1D, 2D, and 3D photonic crystal examples. Curvilinear coordinate transform is applied to the Maxwell's Equations to study waveguide bend (Chapter 6). By finding the phase difference along propagation direction at various $XY$ plane locations, the behaviors of electromagnetic wave propagation (such as light bending, focusing etc) can be studied (Chapter 7), which can be applied to diffractive optics for new devices design.

Numerical simulation tools for lasing devices are usually based on rate equations which are not accurate above the threshold and for small scale lasing cavities (such as nano-scale cavities). Recently, we extend the TMM package function to include the capacity of dealing active gain materials. Both lasing (above threshold) and spontaneous emission (below threshold) can be studied in the frame work of our Gain-TMM algorithm. Chapter 8 will illustrate the algorithm in detail and show the simulation results for 3D photonic crystal lasing devices.

Then, microwave experiments (mainly resonant cavity embedded at layer-by-layer woodpile structures) are performed at Chapter 9 as an efficient practical way to study photonic crystal devices. The size of photonic crystal under microwave region is at the order of centimeter which makes the fabrication easier to realize. At the same time due to the scaling property, the result of microwave experiments can be applied directly to optical or infrared frequency regions. The systematic TMM simulations for various resonant cavities are performed and consistent results are obtained when compared with microwave experiments. Besides scaling the experimental results to much smaller wavelength, designing potential photonic crystal devices for application at microwave is also an interesting and important topic.

Finally, we describe the future development of TMM algorithm such as using localized functions as basis to more efficiently simulate disorder problems (Chapter 10). Future applications of photonic crystal concepts are also discussed at Chapter 10.

Along with this dissertation, *TMM Photonic Crystal Package User Manual* and *Gain TMM Photonic Crystal Package User Manual* written by me, Dr. Jiangrong Cao (Canon USA) and Dr. Xinhua Hu (Ames Lab) focus more on the programming detail, software user interface, trouble shooting, and step-by-step instructions. This dissertation and the two user manuals are essential documents for TMM software package beginners and advanced users. Future software developments, new version releases and FAQs can be tracked through my web page: http://www.public.iastate.edu/~mli/

In summary, this dissertation has extended the planewave based transfer (scattering) matrix method in many aspects which make the TMM and Gain-TMM software package a powerful simulation tool in photonic crystal study. Comparisons of TMM and GTMM results with other published numerical results and experimental results indicate that TMM and GTMM is accurate and highly efficient in photonic crystal device simulation and design.

# Chapter 1. General introduction

## 1.1 History of photonic crystal

The history of human development is the history of how people can utilize and control the properties of materials, nature or man made. At the very beginning age of civilization, human being learnt how to use and manipulate with the mechanical property of stone to make stereotype tools for everyday life. We call this period Stone Age. Later on, people studied how to get metal and alloy from ore. Metal and alloy have better mechanical properties and the application of those materials towards agriculture made the human society development possible. Even more recent invention of steam locomotive was based on how to improve the mechanical movement which made modern civilization possible. In most of the mankind history, we are improving on how to control or utilize the mechanical properties of materials.

Although the electrical and optical properties were noticed by us long time ago, the theoretical study of fundamental electrical and optical phenomena is not done until around two hundred years ago due to the tiny size of electron, photon and atomic structure.

Maxwell introduced his famous equations at 1864 to systematically describe the behavior of electromagnetic wave. In 1926, Schrödinger published his quantum mechanics paper to describe how electrons behave. In the middle of $20^{th}$ century, with the efforts of both theoretical and experimental physicists, we can control the motion of electrons by introducing defects into pure crystals or semiconductors. After we had the ability to control the electrical properties, the electrical engineering industry development is possible and it has profound impact on our daily life. [1-5]

Nature crystal is a periodic arrangement of atoms which gives periodic potential to electrons inside the crystal. Block's theory can be applied to Schrödinger's equation and the solution of Schrödinger's equation reveals the possible ways to control the motion of electrons. However there are no nature available "photonic" crystals to provide a similar way to control photon or electromagnetic wave as crystal to electrons. Can you image it that it is not until 1987, more than 100 years after Maxwell's Equation, that the concept of photonic crystal was introduced by Eli Yablonovitch[6] and Sajeev John[7]? And it is only after three years for the concept to be finally confirmed by K.M. Ho[8] and coworker. But after the 1987 concept breakthrough and 1990 concept confirmation, both theory and experiment are booming based on the idea of photonic crystal. Various applications, such as low-loss waveguide and high Q resonant cavity, are proposed in recent years and some are close to the stage of mass production. The application of photonic crystal devices will be tremendous in people's everyday life. Even the simplest way to control light propagation, the internal refraction, has already changed the entire communication industry via the invention of optical fiber. With the new concept of photonic crystal, the better quality photonic crystal fibers are on the market.

Now let's look back what people were doing after the 1987 concept breakthrough. A lot of physicist both from theoretical and experimental joined the research field of photonic crystal. But at the first a few years, people were struggling to prove the photonic crystal concept by obtaining consistent results of experimental and numerical simulation. Experimental physicists first adopted the cut-and-try method which basically depends on the lucky of the proposed geometry structure. But after many tedious works, the so called full band gap structures were still illusions. At the same time, theoretical physicists adopted the method to solve scalar wave functions for electrons to study electromagnetic wave. Due to the vector nature of electromagnetic wave and Maxwell's Equations, the scalar wave approaches failed. At 1990, Kai-Ming Ho[9] and coworker introduced planewave expansion methods to solve the vector Maxwell's Equations and successfully predicted that diamond structure will have full

band gap. Later on, Eli Yablonovitch made the first photonic crystal at microwave region based on the predicted diamond structure. The concept of photonic crystal then was firmly established and numerous fabrication techniques and numerical simulation methods were introduced in this fast developing research field.

Now it is already twenty years after the 1987 concept breakthrough, photonic crystal has been studied intensively. However, with the exception of photonic crystal fibers, very few concepts have been able to pass from the scientific research stage to high throughputs mainstream products. Besides the challenges in manufacturing, one of the main reasons behind this situation is the lack of efficient and versatile numerical computation tools for photonic crystal devices simulation, especially three-dimensional structures with defects. Our planewave based transfer (scattering) matrix method is proved to be an efficient and accurate numerical simulation tool for photonic crystal through this thesis via various structures and applications.

## 1.2 Comparison between crystal and photonic crystal

The status of photons in photonic crystal and the status of electrons in crystal have many similarities: both systems are eigenvalue problem; the geometry periodicity in both systems leads to the application of Bloch Theorem which leads to the concept of band and band structure; in both systems the introduction of defects makes possible of controlling the corresponding electric or optical properties. Based on those similarities, many concepts and strategies in quantum mechanics and solid state physics can be borrowed to the research field of photonic crystal, such as reciprocal lattice and Brillouin zone. However, there are two major differences between electron and photon: (1) there is no interaction between photons (for linear optics) while there are electron-electron interaction; (2) there is no characteristic length for photons and the band structure can be scaled to any length scale while there is a nature length scale for electrons.[1-2]

In principle, photonic crystals are periodic arrangement of dielectric material in one direction, two directions or all three directions in space, and we call them 1D, 2D or 3D photonic crystal correspondingly. In general cases periodic structures do not guarantee the existence of full photonic band gap in which no propagating modes exist for any directions. In later part of this thesis, we use planewave based transfer (scattering) matrix method to study the spectrum, band structure and mode profiles for various photonic crystal structures. With the extension of transfer (scattering) matrix method to active gain materials, lasing and spontaneous emission with the present of photonic crystal background can be studied.

**References:**


1. John D. Joannopoulos, *Photonic crystal – Molding the Flow of Light*, Princeton University Press, 1995
2. Steven G Johnson, *Photonic crystal – The road from theory to practice*, Kluwer Academic Publishers, 2002
3. Neil W. Ashcroft and N. David Mermin, *Solid State Physics*, Brooks Cole Press, 1976
4. M. Born and E. Wolf, *Principles of Optics*, 7th edition, Cambridge University Press, 1999
5. J. D. Jackson , *Classical Electrodynamics*, 3rd edition, Wiley & Sons Press, 2004
6. E. Yablonovitch, "Inhibited Spontaneous Emission in Solid-State Physics and Electronics," *Phys. Rev. Lett.* **58**, 2059 (1987)
7. S. John, "Strong Localization of Photons in Certain Disordered Dielectric Superlattices", *Phys. Rev. Lett.* **58**, 2486 (1987)
8. K. M. Ho, C. T. Chan, and C. M. Soukoulis, "Existence of a photonic gap in periodic dielectric structures", *Phys. Rev. Lett.* **65**, 3152 (1990)

# Chapter 2. The planewave based transfer (scattering) matrix method - core algorithms

This chapter contains very detailed derivation of how to get the scatter matrix (S matrix) for general 3D structures from the Maxwell's Equations and acts like a literature review part. Most of the content has been published by Dr. Zhi-Yuan Li at a set of journal papers which are listed at the reference part of this chapter. After the S matrix is ready, transmittance, reflectance and absorptance can be obtained directly through the scattering matrix algorithm. Photonic crystal band structure and electric and magnetic field distribution (mode profile) at any given location can also be obtained with a few more steps. The first several sections on how to get the S matrix may be looked through quickly and those sections of how to use calculated S matrix to get spectrum, band structure or mode profile may be focused in detail first. Then topics on how to get the S matrix can be revisited in more detail.[1-10]

## 2.1 Maxwell's Equations

The most general case of macroscopic Maxwell's Equations in Gaussian Unit is Eq. (2.1) and (2.2) where field vectors $\mathbf{E}$, $\mathbf{D}$, $\mathbf{H}$, and $\mathbf{B}$ are function of time and space. In most of this thesis, we only deal with passive and non-magnetic material, i.e. there are no free charge and no free current (Eq. (2.3)) and $\mu(\mathbf{r}) = 1$. With this simplification we can get the Maxwell's Equations only involve $\mathbf{E}$ and $\mathbf{H}$ field (Eq. (2.4)). Further more, with the assumption that $\mathbf{E}$ and $\mathbf{H}$ field are harmonic in time (Eq. (2.5)), we can separate the space variable and time variable and focus on the space variation of $\mathbf{E}$ and $\mathbf{H}$ field at given frequency (Eq. (2.6)). Now we introduce wave vector $k_0$ (Eq. (2.7)) and the first two Maxwell's Equations becomes Eq. (2.8). The angular frequency or wave vector is then acting like one input parameter and every angular frequency follows the identical calculation procedure. This is

the feature of frequency domain method: there will be no relation across different frequencies and no time dependence which will lead to the steady status solutions.

$$\begin{aligned}
&\nabla \times \mathbf{E} = -\frac{1}{c}\frac{\partial \mathbf{B}}{\partial t} \\
&\nabla \times \mathbf{H} = \frac{1}{c}\frac{\partial \mathbf{D}}{\partial t} + \frac{4\pi}{c}\mathbf{J} \\
&\nabla \bullet \mathbf{D} = 4\pi\rho \\
&\nabla \bullet \mathbf{B} = 0
\end{aligned} \tag{2.1}$$

$$\begin{aligned}
&\mathbf{D} = \varepsilon_0 \varepsilon(\mathbf{r})\mathbf{E} \\
&\mathbf{B} = \mu_0 \mu(\mathbf{r})\mathbf{H} \\
&\mu(\mathbf{r}) = 1 \\
&\mu_0 = 1 \quad , \quad \varepsilon_0 = 1 \\
&c = 2.997 \times 10^{10} cm \bullet s^{-1}
\end{aligned} \tag{2.2}$$

$$\mathbf{J} = 0 \ , \ \rho = 0 \tag{2.3}$$

$$\begin{aligned}
&\nabla \times \mathbf{E} = -\frac{1}{c}\frac{\partial \mathbf{H}}{\partial t} \\
&\nabla \times \mathbf{H} = \frac{\varepsilon(\mathbf{r})}{c}\frac{\partial \mathbf{E}}{\partial t} \\
&\nabla \bullet \varepsilon(\mathbf{r})\mathbf{E} = 0 \\
&\nabla \bullet \mathbf{H} = 0
\end{aligned} \tag{2.4}$$

$$\begin{aligned}
&\mathbf{E} = \mathbf{E}(\mathbf{r})e^{-\mathbf{i}\omega t} \\
&\mathbf{H} = \mathbf{H}(\mathbf{r})e^{-\mathbf{i}\omega t}
\end{aligned} \tag{2.5}$$

$$\begin{aligned}
&\nabla \times \mathbf{E}(\mathbf{r}) = \mathbf{i}\frac{\omega}{c}\mathbf{H}(\mathbf{r}) \\
&\nabla \times \mathbf{H}(\mathbf{r}) = -\mathbf{i}\frac{\omega}{c}\varepsilon(\mathbf{r})\mathbf{E}(\mathbf{r}) \\
&\nabla \bullet \varepsilon(\mathbf{r})\mathbf{E}(\mathbf{r}) = 0 \\
&\nabla \bullet \mathbf{H}(\mathbf{r}) = 0
\end{aligned} \tag{2.6}$$

$$k_0 = \frac{\omega}{c} = \frac{2\pi f}{c} = \frac{2\pi}{\lambda_0} \tag{2.7}$$

$$\begin{aligned} \nabla \times \mathbf{E}(\mathbf{r}) &= \mathbf{i}k_0 \mathbf{H}(\mathbf{r}) \\ \nabla \times \mathbf{H}(\mathbf{r}) &= -\mathbf{i}k_0 \varepsilon(\mathbf{r}) \mathbf{E}(\mathbf{r}) \end{aligned} \tag{2.8}$$

Eq. (2.8) are actually vector differential equations and there are altogether six equations when we write the field vector out with respect to their components (Eq. (2.9)).

$$\begin{aligned} &\frac{\partial E_z}{\partial y} - \frac{\partial E_y}{\partial z} = \mathbf{i}k_0 H_x \qquad \frac{\partial H_z}{\partial y} - \frac{\partial H_y}{\partial z} = \mathbf{i}k_0 \varepsilon(\mathbf{r}) E_x \\ &-\frac{\partial E_z}{\partial x} + \frac{\partial E_x}{\partial z} = \mathbf{i}k_0 H_y \,, -\frac{\partial H_z}{\partial x} + \frac{\partial H_x}{\partial z} = \mathbf{i}k_0 \varepsilon(\mathbf{r}) E_y \\ &\frac{\partial E_y}{\partial x} - \frac{\partial E_x}{\partial y} = \mathbf{i}k_0 H_z \qquad \frac{\partial H_y}{\partial x} - \frac{\partial H_x}{\partial y} = \mathbf{i}k_0 \varepsilon(\mathbf{r}) E_z \end{aligned} \tag{2.9}$$

We can express $H_z$ and $E_z$ in term of $E_x$, $E_y$, $H_x$ and $H_y$ (Eq. (2.10)) and eliminate $H_z$ and $E_z$ from Eq. (2.9) and get equations involving $E_x$, $E_y$, $H_x$ and $H_y$ only (Eq. (2.11))

$$\begin{aligned} H_z &= \frac{1}{\mathbf{i}k_0} \left( \frac{\partial E_y}{\partial x} - \frac{\partial E_x}{\partial y} \right) \\ E_z &= \frac{1}{\mathbf{i}k_0 \varepsilon(\mathbf{r})} \left( \frac{\partial H_y}{\partial x} - \frac{\partial H_x}{\partial y} \right) \end{aligned} \tag{2.10}$$

Equation set (2.11) is our starting point to solve the macroscopic Maxwell's Equations at periodic dielectric medium (i.e. photonic crystal structures) via the planewave based transfer (scattering) matrix method. To solve this partial differential equation set, our approach is to expand the field components and dielectric function into reciprocal space (Fourier space) which makes a set of difficult partial differential equations into relatively easier linear algebra problems; or we call it planewave based approach.

$$
\begin{aligned}
\frac{\partial E_x}{\partial z} &= \frac{\partial}{\partial x}[-\frac{1}{\mathbf{i}k_0\varepsilon(\mathbf{r})}(\frac{\partial H_y}{\partial x}-\frac{\partial H_x}{\partial y})]+\mathbf{i}k_0 H_y \\
\frac{\partial E_y}{\partial z} &= \frac{\partial}{\partial y}[-\frac{1}{\mathbf{i}k_0\varepsilon(\mathbf{r})}(\frac{\partial H_y}{\partial x}-\frac{\partial H_x}{\partial y})]-\mathbf{i}k_0 H_x \\
\frac{\partial H_x}{\partial z} &= \frac{\partial}{\partial x}[\frac{1}{\mathbf{i}k_0}(\frac{\partial E_y}{\partial x}-\frac{\partial E_x}{\partial y})]-\mathbf{i}k_0\varepsilon(\mathbf{r})E_y \\
\frac{\partial H_y}{\partial z} &= \frac{\partial}{\partial y}[\frac{1}{\mathbf{i}k_0}(\frac{\partial E_y}{\partial x}-\frac{\partial E_x}{\partial y})]+\mathbf{i}k_0\varepsilon(\mathbf{r})E_x
\end{aligned}
\qquad (2.11)
$$

## 2.2 Fourier space expansion

Now let's suppose electromagnetic wave is propagating along Z axis towards a trunk of photonic crystal. Inside the photonic crystal, the dielectric distribution at any XY plane (perpendicular to Z axis) is periodic in both X and Y directions (for 3D photonic crystal) or uniform in one direction and periodic in the other direction (for 2D photonic crystal) or uniform in both X and Y directions (for 1D photonic crystal). Actually uniform distribution at any direction is equivalent to have arbitrary periodicity along this direction, and in principle the dielectric distribution functions have double periodicity along X and Y directions in any Z axis positions (Figure 2-1).

Then the XY unit cell is defined as the minimum repeat area in the XY plane, and if the dielectric constant is uniform along X or Y axis, the length of XY unit cell along that direction can be arbitrary. The edge of unit cell is defined as the lattice constant ($\mathbf{a_1}$, $\mathbf{a_2}$) with the lattice points represent by $\mathbf{R} = m_1\mathbf{a_1} + m_2\mathbf{a_2}$ where $m_1$ and $m_2$ are integers. The reciprocal lattice points are then defined as $\mathbf{G} = n_1\mathbf{b_1} + n_2\mathbf{b_2}$ where $n_1$ and $n_2$ are integers and ($\mathbf{b_1}$, $\mathbf{b_2}$) the reciprocal lattice constant. With the requirement of $e^{\mathbf{iG\cdot R}} = 1$ or $\mathbf{G\cdot R} = 2N\pi$ (Block's Theorem), $\mathbf{b_1} = 2\pi/\mathbf{a}_1$ and $\mathbf{b_2} = 2\pi/\mathbf{a}_2$ can be obtained. Then any periodic function $f(\mathbf{r}) = f(\mathbf{r}+\mathbf{R})$ can be expressed as $f(\mathbf{r}) = \sum f_{\mathbf{G}} e^{\mathbf{iG\cdot r}}$ where $f_{\mathbf{G}}$ is the Fourier coefficient

for each reciprocal lattice $\mathbf{G}$. Or write in more detailed way at Eq. (2.12). Here we assume $\mathbf{a}_1$ and $\mathbf{a}_2$ are along X and Y axis respectively (orthogonal lattice constant), but in general $\mathbf{a}_1$ and $\mathbf{a}_2$ can be along any directions.

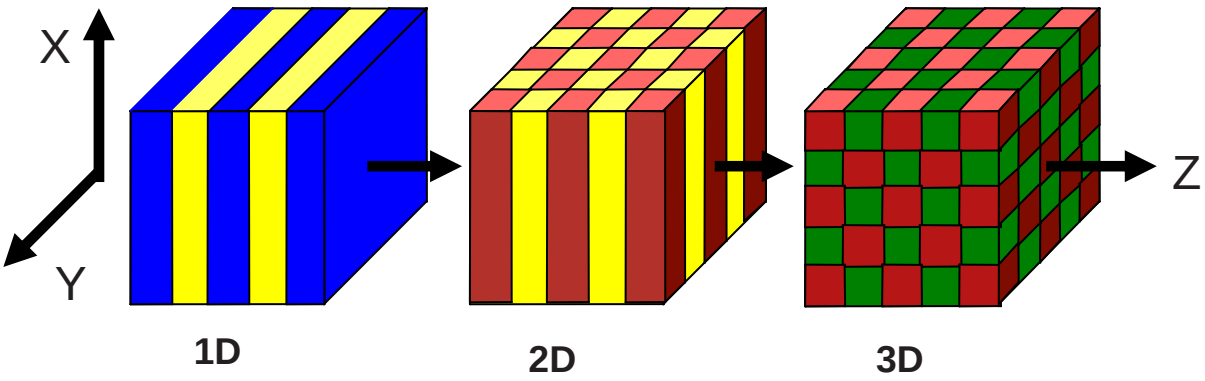


Figure 2-1: Dielectric distribution function of double periodicity along X and Y directions

$$f(x,y)=\sum_{n_1=-\infty}^{\infty}\sum_{n_2=-\infty}^{\infty} f_{G_{n_1,n_2}} e^{\mathbf{i}(n_1\frac{2\pi}{a_1}x+n_2\frac{2\pi}{a_2}y)}$$
$$f_{G_{n_1,n_2}}=\frac{(2\pi)^2}{a_1a_2}\int_0^{a_1}\int_0^{a_2} f(x,y)e^{-\mathbf{i}(n_1\frac{2\pi}{a_1}x+n_2\frac{2\pi}{a_2})}dxdy \qquad (2.12)$$

The reciprocal of dielectric distribution function $1/\varepsilon(\mathbf{r})$ is a periodic function and can be expressed in Fourier space (Eq. (2.13)). In the real calculation, the sum over $m$ and $n$ must be truncate to finite terms, for example: $-N_x \le m \le N_x$ , $-N_y \le n \le N_y$ with $N_0=(2N_x+1)(2N_y+1)$ called the total number of planewave.

When a plane electromagnetic wave is incident from the left hand side on a photonic crystal slab with incident wave vector $\mathbf{k_0}=(k_{0x},k_{0y},k_{0z})$. The electromagnetic field at any arbitrary point $\mathbf{r}$ can be written into the superposition of plane waves with vector $\mathbf{E_{mn}}$ and $\mathbf{H_{mn}}$ the unknown expansion coefficients (Eq. (2.14)); or expressed in term of scalar field components $E_{mn,x}, E_{mn,y}, H_{mn,x}, H_{mn,y}$ and truncated to finite total planewave numbers at Eq. (2.15).

$$\frac{1}{\varepsilon(r+R)} = \frac{1}{\varepsilon(r)}$$

$$\frac{1}{\varepsilon(r)} = \sum_{m=-Nx}^{Nx} \sum_{n=-Ny}^{Ny} \varepsilon_{mn}^{-1} e^{\mathbf{i}(m\frac{2\pi}{a_1}x + n\frac{2\pi}{a_2}y)}$$

$$= \sum_{m=-Nx}^{Nx} \sum_{n=-Ny}^{Ny} \varepsilon_{mn}^{-1} e^{\mathbf{i}(G_{mn,x}x + G_{mn,y}y)} \tag{2.13}$$

$$\varepsilon_{mn}^{-1} = \frac{(2\pi)^2}{a_1 a_2} \int_0^{a_1} \int_0^{a_2} \frac{1}{\varepsilon(x,y)} e^{-\mathbf{i}(m\frac{2\pi}{a_1}x + n\frac{2\pi}{a_2}y)} dxdy$$

$$G_{mn,x} = m\frac{2\pi}{a_1}, \quad G_{mn,y} = n\frac{2\pi}{a_2}$$

$$\mathbf{E}(\mathbf{r}) = \sum_{m=-\infty}^{\infty} \sum_{n=-\infty}^{\infty} \mathbf{E_{mn}}(z) e^{\mathbf{i}(k_{mn,x}x + k_{mn,y}y)}$$

$$\mathbf{H}(\mathbf{r}) = \sum_{m=-\infty}^{\infty} \sum_{n=-\infty}^{\infty} \mathbf{H_{mn}}(z) e^{\mathbf{i}(k_{mn,x}x + k_{mn,y}y)} \tag{2.14}$$

$$k_{mn,x} = k_{0x} + G_{mn,x} = k_{0x} + m\frac{2\pi}{a_1}$$

$$k_{mn,y} = k_{0y} + G_{mn,y} = k_{0y} + n\frac{2\pi}{a_2}$$

$$E_x(\mathbf{r}) = \sum_{m=-N_x}^{N_x} \sum_{n=-N_y}^{N_y} E_{mn,x}(z) e^{\mathbf{i}(k_{mn,x}x + k_{mn,y}y)}$$

$$E_y(\mathbf{r}) = \sum_{m=-N_x}^{N_x} \sum_{n=-N_y}^{N_y} E_{mn,y}(z) e^{\mathbf{i}(k_{mn,x}x + k_{mn,y}y)}$$

$$H_x(\mathbf{r}) = \sum_{m=-N_x}^{N_x} \sum_{n=-N_y}^{N_y} H_{mn,x}(z) e^{\mathbf{i}(k_{mn,x}x + k_{mn,y}y)} \tag{2.15}$$

$$H_y(\mathbf{r}) = \sum_{m=-N_x}^{N_x} \sum_{n=-N_y}^{N_y} H_{mn,y}(z) e^{\mathbf{i}(k_{mn,x}x + k_{mn,y}y)}$$

## 2.3 Transforming partial differential equations to linear equations

With Eq. (2.13) and (2.15) ready, we plug them into the Maxwell's Equations for each component (Eq. (2.11)). Here, we will derive the first equation at Eq. (2.11) to Fourier space; the other three equations at Eq. (2.11) can be derived similarly.

First, we write out a set of equations of partial derivative of $E_x$, $H_y$, $H_x$ in Fourier space (Eq. (2.16)) and with the last two equations at Eq. (2.16) we can obtain Eq. (2.17).

$$\begin{aligned}
\frac{\partial E_x}{\partial z} &= \sum_{i=-\infty}^{\infty}\sum_{j=-\infty}^{\infty}\frac{\partial}{\partial z}E_{ij,x}e^{\mathbf{i}\left(k_{ij,x}x+k_{ij,y}y\right)} \\
\frac{\partial H_y}{\partial x} &= \sum_{i=-\infty}^{\infty}\sum_{j=-\infty}^{\infty}\mathbf{i}k_{ij,x}H_{ij,y}e^{\mathbf{i}\left(k_{ij,x}x+k_{ij,y}y\right)} \\
\frac{\partial H_x}{\partial y} &= \sum_{i=-\infty}^{\infty}\sum_{j=-\infty}^{\infty}\mathbf{i}k_{ij,y}H_{ij,x}e^{\mathbf{i}\left(k_{ij,x}x+k_{ij,y}y\right)}
\end{aligned} \tag{2.16}$$

$$\frac{\partial H_y}{\partial x}-\frac{\partial H_x}{\partial y}=\sum_{i=-\infty}^{\infty}\sum_{j=-\infty}^{\infty}\mathbf{i}\left(k_{ij,x}H_{ij,y}-k_{ij,y}H_{ij,x}\right)e^{\mathbf{i}\left(k_{ij,x}x+k_{ij,y}y\right)} \tag{2.17}$$

$$\begin{aligned}
&\frac{1}{\mathbf{i}k_0\varepsilon(\mathbf{r})}\left(\frac{\partial H_y}{\partial x}-\frac{\partial H_x}{\partial y}\right)= \\
&\frac{1}{\mathbf{i}k_0}\left(\sum_{i=-\infty}^{\infty}\sum_{j=-\infty}^{\infty}\varepsilon_{ij}^{-1}e^{\mathbf{i}\left(G_{ij,x}x+G_{ij,y}y\right)}\right)\left(\sum_{i=-\infty}^{\infty}\sum_{j=-\infty}^{\infty}\mathbf{i}\left(k_{ij,x}H_{ij,y}-k_{ij,y}H_{ij,x}\right)e^{\mathbf{i}\left(k_{ij,x}x+k_{ij,y}y\right)}\right) \\
&=\frac{1}{k_0}\sum_{i=-\infty}^{\infty}\sum_{j=-\infty}^{\infty}\sum_{m=-\infty}^{\infty}\sum_{n=-\infty}^{\infty}\varepsilon_{ij}^{-1}e^{\mathbf{i}\left(G_{ij,x}x+G_{ij,y}y\right)}\left(k_{mn,x}H_{mn,y}-k_{mn,y}H_{mn,x}\right)e^{\mathbf{i}\left(k_{mn,x}x+k_{mn,y}y\right)} \\
&=\frac{1}{k_0}\sum_{i=-\infty}^{\infty}\sum_{j=-N_y}^{\infty}\sum_{m=-\infty}^{\infty}\sum_{n=-\infty}^{\infty}\varepsilon_{ij}^{-1}\left(k_{mn,x}H_{mn,y}-k_{mn,y}H_{mn,x}\right)e^{\mathbf{i}\left(\left(k_{mn,x}+G_{ij,x}\right)x+\left(k_{mn,y}+G_{ij,y}\right)y\right)}
\end{aligned} \tag{2.18}$$

$$
\begin{aligned}
&k_{mn,x} + G_{ij,x} = k_{(m+i)(n+j),x} = k_{m'n',x} \\
&k_{mn,y} + G_{ij,y} = k_{(m+i)(n+j),y} = k_{m'n',y} \\
&with: \quad m' = m + i, n' = n + j \\
&-\infty < m < \infty \Leftrightarrow -\infty < m' < \infty \\
&-\infty < n < \infty \Leftrightarrow -\infty < n' < \infty
\end{aligned}
\tag{2.19}
$$

With Eq. (2.17) and Eq. (2.13) ready, we can rewrite the term under the partial derivative of right hand side of the first Maxwell's Equation (Eq. (2.11)) into Fourier space notation (Eq. (2.18)). With redefined indices of Eq. (2.19), Eq. (2.18) can be rewritten as Eq. (2.20).

$$
\begin{aligned}
&\frac{1}{\mathbf{i}k_0\varepsilon(\mathbf{r})}\left(\frac{\partial H_y}{\partial x} - \frac{\partial H_x}{\partial y}\right) \\
&= \frac{1}{k_0}\sum_{i=-\infty}^{\infty}\sum_{j=-\infty}^{\infty}\sum_{m=-\infty}^{\infty}\sum_{n=-\infty}^{\infty}\varepsilon_{ij}^{-1}\left(k_{mn,x}H_{mn,y} - k_{mn,y}H_{mn,x}\right)e^{\mathbf{i}\left(k_{mn,x}x + k_{mn,y}y\right)} \\
&= \frac{1}{k_0}\sum_{i=-N_x}^{\infty}\sum_{j=-N_y}^{\infty}\sum_{m'=-\infty}^{\infty}\sum_{n'=-\infty}^{\infty}\varepsilon_{ij}^{-1}\left(k_{(m'-i)(n'-j),x}H_{(m'-i)(n'-j),y} - k_{(m'-i)(n'-j),y}H_{(m'-i)(n'-j),x}\right)e^{\mathbf{i}\left(k_{m'n',x}x + k_{m'n',y}y\right)} \\
&= \frac{1}{k_0}\sum_{i=-\infty}^{\infty}\sum_{j=-\infty}^{\infty}\sum_{m=-\infty}^{\infty}\sum_{n=-\infty}^{\infty}\varepsilon_{ij}^{-1}\left(k_{(m-i)(n-j),x}H_{(m-i)(n-j),y} - k_{(m-i)(n-j),y}H_{(m-i)(n-j),x}\right)e^{\mathbf{i}\left(k_{mn,x}x + k_{mn,y}y\right)}
\end{aligned}
\tag{2.20}
$$

$$
\begin{aligned}
&m - i = i', n - j = j', i = m - i', j = n - j' \\
&-\infty < i < \infty \Leftrightarrow -\infty < i' < \infty \\
&-\infty < j < \infty \Leftrightarrow -\infty < j' < \infty
\end{aligned}
\tag{2.21}
$$

$$
\begin{aligned}
&\frac{1}{\mathbf{i}k_0\varepsilon(\mathbf{r})}\left(\frac{\partial H_y}{\partial x} - \frac{\partial H_x}{\partial y}\right) \\
&= \frac{1}{k_0}\sum_{i'=-\infty}^{\infty}\sum_{j'=-\infty}^{\infty}\sum_{m=-\infty}^{\infty}\sum_{n=-\infty}^{\infty}\varepsilon_{(m-i')(n-j')}^{-1}\left(k_{i'j',x}H_{i'j',y} - k_{i'j',y}H_{i'j',x}\right)e^{\mathbf{i}\left(k_{mn,x}x + k_{mn,y}y\right)} \\
&= \frac{1}{k_0}\sum_{i=-\infty}^{\infty}\sum_{j=-\infty}^{\infty}\sum_{m=-\infty}^{\infty}\sum_{n=-\infty}^{\infty}\varepsilon_{(m-i)(n-j)}^{-1}\left(k_{ij,x}H_{ij,y} - k_{ij,y}H_{ij,x}\right)e^{\mathbf{i}\left(k_{mn,x}x + k_{mn,y}y\right)}
\end{aligned}
\tag{2.22}
$$

With further redefined indices at Eq. (2.21), we can reach Eq. (2.22). So the right hand side of the first Maxwell's Equations (Eq. (2.11)) can be expressed as Eq. (2.23). Finally, according to the first equation at Eq. (2.11), we can get the relation between $E_{ij,x}$ and $H_{ij,x}$,

$H_{ij,y}$, $\varepsilon_{ij}^{-1}$ (Eq. (2.24)). Similarly, all four equations at Eq. (2.11) can be transformed into the $i, j$ components equation set (Eq. (2.25)) with $\delta_{im,jn} = 1$ for $i = m$, and $\delta_{im,jn} = 0$ otherwise.

$$\begin{aligned}
&\frac{\partial}{\partial x}\left[-\frac{1}{\mathbf{i}k_0\varepsilon(\mathbf{r})}\left(\frac{\partial H_y}{\partial x}-\frac{\partial H_x}{\partial y}\right)\right]+\mathbf{i}k_0 H_y \\
&=-\frac{\mathbf{i}}{k_0}\sum_{i=-\infty}^{\infty}\sum_{j=-\infty}^{\infty}\sum_{m=-\infty}^{\infty}\sum_{n=-\infty}^{\infty}k_{mn,x}\varepsilon^{-1}_{(m-i)(n-j)}\left(k_{ij,x}H_{ij,y}-k_{ij,y}H_{ij,x}\right)e^{\mathbf{i}\left(k_{mn,x}x+k_{mn,y}y\right)} \\
&+\mathbf{i}k_0\sum_{i=-\infty}^{\infty}\sum_{j=-\infty}^{\infty}H_{ij,y}e^{\mathbf{i}\left(k_{ij,x}x+k_{ij,y}y\right)} \\
&=-\frac{\mathbf{i}}{k_0}\sum_{i=-\infty}^{\infty}\sum_{j=-\infty}^{\infty}\left[\sum_{m=-\infty}^{\infty}\sum_{n=-\infty}^{\infty}k_{ij,x}\varepsilon^{-1}_{(i-m)(j-n)}\left(k_{mn,x}H_{mn,y}-k_{mn,y}H_{mn,x}\right)\right]e^{\mathbf{i}\left(k_{ij,x}x+k_{ij,y}y\right)} \\
&+\mathbf{i}k_0\sum_{i=-\infty}^{\infty}\sum_{j=-\infty}^{\infty}H_{ij,y}e^{\mathbf{i}\left(k_{ij,x}x+k_{ij,y}y\right)}
\end{aligned} \tag{2.23}$$

$$\frac{\partial E_{ij,x}}{\partial z}=-\frac{\mathbf{i}k_{ij,x}}{k_0}\sum_{mn}\varepsilon^{-1}_{i-m,j-n}(H_{mn,y}k_{mn.x}-H_{mn,x}k_{mn,y})+\mathbf{i}k_0H_{ij,y} \tag{2.24}$$

Now we define two column vectors (Eq. (2.26)) to represent the unknown coefficients of $E_{ij,x}$, $E_{ij,y}$, $H_{ij,x}$ and $H_{ij,y}$ at Eq. (2.25). Then the equation set of unknown coefficients (Eq. (2.25)) can be expressed in a concise format (Eq. (2.27)) where matrix $T_1$ and $T_2$ are defined at Eq. (2.28).

$$\begin{aligned}
\frac{\partial E_{ij,x}}{\partial z}&=-\frac{\mathbf{i}k_{ij,x}}{k_0}\sum_{mn}\varepsilon^{-1}_{i-m,j-n}(H_{mn,y}k_{mn.x}-H_{mn,x}k_{mn,y})+\mathbf{i}k_0H_{ij,y} \\
\frac{\partial E_{ij,y}}{\partial z}&=-\frac{\mathbf{i}k_{ij,y}}{k_0}\sum_{mn}\varepsilon^{-1}_{i-m,j-n}(H_{mn,y}k_{mn.y}-H_{mn,x}k_{mn,x})-\mathbf{i}k_0H_{ij,x} \\
\frac{\partial H_{ij,x}}{\partial z}&=\frac{\mathbf{i}k_{ij,x}}{k_0}\sum_{mn}\delta_{im,jn}(k_{mn,x}E_{mn.y}-k_{mn,y}E_{mn,x})-\mathbf{i}k_0\sum_{mn}\varepsilon_{i-m,j-n}E_{mn.y} \\
\frac{\partial H_{ij,y}}{\partial z}&=\frac{\mathbf{i}k_{ij,x}}{k_0}\sum_{mn}\delta_{im,jn}(k_{mn,x}E_{mn.y}-k_{mn,y}E_{mn,x})+\mathbf{i}k_0\sum_{mn}\varepsilon_{i-m,j-n}E_{mn.x}
\end{aligned} \tag{2.25}$$

$$E = (\ldots,\ E_{ij,x},\ E_{ij,y},\ \ldots)^T$$
$$H = (\ldots,\ H_{ij,x},\ H_{ij,y},\ \ldots)^T \tag{2.26}$$

$$\frac{\partial}{\partial z}E = T_1 H,\ \frac{\partial}{\partial z}H = T_2 E \tag{2.27}$$

$$T_1^{ij,mn} = \frac{\mathbf{i}}{k_0}\begin{pmatrix} k_{ij,x}\varepsilon^{-1}_{i-m,j-n}k_{mn,y} & -k_{ij,x}\varepsilon^{-1}_{i-m,j-n}k_{mn,x} + k_0^2\delta_{im,jn} \\ k_{ij,y}\varepsilon^{-1}_{i-m,j-n}k_{mn,y} - k_0^2\delta_{im,jn} & -k_{ij,y}\varepsilon^{-1}_{i-m,j-n}k_{mn,x} \end{pmatrix}$$
$$T_2^{ij,mn} = \frac{\mathbf{i}}{k_0}\begin{pmatrix} -k_{ij,x}\delta_{im,jn}k_{mn,y} & k_{ij,x}\delta_{im,jn}k_{mn,x} - k_0^2\varepsilon_{i-m,j-n} \\ -k_{ij,y}\delta_{im,jn}k_{mn,y} + k_0^2\varepsilon_{i-m,j-n} & k_{ij,y}\delta_{im,jn}k_{mn,x} \end{pmatrix} \tag{2.28}$$

If we use finite planewave number: $-N_x \le i \le N_x$ , $-N_y \le j \le N_y$ , we can define several planewave related variables: $N_t = N_0 = (2N_x+1)(2N_y+1)$ , $N_p = 2N_t$ and $N_s = 4N_t$ . The dimension of the unknown coefficient vector $E$ and $H$ is $N_p \times 1$; and the dimension of matrix $T_1$ and $T_2$ is $N_p \times N_p$ . From Eq. (2.27), we can get a single 2nd order differential equation (Eq. (2.29)) with dimension of matrix $P$ and $Q$ $N_p \times N_p$ . As $Q$ is a matrix of dimension $N_p \times N_p$ , the eigenvalue and eigenvector of $Q$ can be found by linear algebra through Eq. (2.30). With the eigenvalue $\beta^2$ calculated, Eq. (2.29) can be expressed by Eq. (2.31) with each element of the unknown coefficients in vector $E$ function of coordinate $z$ .

$$\frac{\partial^2}{\partial z^2}E = \left(T_1 T_2\right)E = PE = -QE$$
$$with:\quad P = T_1 T_2 = -Q \tag{2.29}$$

$$QE = \beta^2 E \tag{2.30}$$

$$\frac{\partial^2}{\partial z^2}E + \beta^2 E = 0 \tag{2.31}$$

$$\frac{\partial^2}{\partial z^2}E_l + \beta_l^2 E_l = 0 \tag{2.32}$$

$$E_l(z) = E_l^+ e^{\mathbf{i}\beta_l z} + E_l^- e^{-\mathbf{i}\beta_l z} = E_l^+(z) + E_l^-(z) \qquad (2.33)$$

Typically, for a matrix of dimension $N_p \times N_p$, there are will be $N_p$ eigenvalues and $N_p$ set of eigenvectors. So $\beta^2$ and $E$ will have $N_p$ different set and we distinguish them by a subscript $l$ with $l = [1, N_p]$ (Eq. (2.32)). The solution of each eigenvector (from Eq. (2.32)) has two propagating modes and can be written as Eq. (2.33). The $N_p$ eigenvalues and $N_p$ set of eigenvector of $Q$ can be arranged as Eq. (2.34) and the $N_p \times N_p$ matrix $S$ is defined.

$$S = \begin{pmatrix} \vdots & \vdots & \cdots & \vdots & \vdots \\ E_{ij,x,1} & E_{ij,x,2} & \cdots & E_{ij,x,N_p-1} & E_{ij,x,N_p} \\ E_{ij,y,1} & E_{ij,y,2} & \cdots & E_{ij,y,N_p-1} & E_{ij,y,N_p} \\ \vdots & \vdots & \cdots & \vdots & \vdots \end{pmatrix} \begin{matrix} \uparrow \\ \\ N_p \\ \\ \downarrow \end{matrix}$$

$$\Updownarrow \quad \Updownarrow \quad \Updownarrow \quad \Updownarrow \quad \Updownarrow$$

$$\beta^2 = (\beta_1^2 \quad \beta_2^2 \quad \cdots \quad \beta_{N_p-1}^2 \quad \beta_{N_p}^2)$$

$$\leftarrow \; - \; - \; N_p \; - \; - \; \rightarrow \qquad (2.34)$$

Now we have a bunch of information inside the matrix S. First electric field components $E_x$ and $E_y$ can be obtained through the Fourier coefficients (i.e. $N_p$ element column vector $E$). While $E$ satisfies Eq. (2.29) and matrix $Q$'s elements are function of Fourier components of $\varepsilon$ and $1/\varepsilon$ (i.e. the real space structure of the macroscopic medium) with $Q$'s eigenvalues and eigenvectors listed at Eq. (2.34). In general, any field Fourier coefficient at vector $E$ is the superposition of all the eigenvectors and there are two propagating directions for each eigenvector (Eq. (2.33)). So $E$ can be expressed in term of the superposition of two set of propagation eigenvectors (Eq. (2.35)) or in a more concise form Eq. (2.36). Here $E^+(z)$ and $E^-(z)$ are both $N_p \times 1$ vectors of unknown coefficients which represents the weight of each of $N_p$ sets of eigenmodes or eigenvectors. Those coefficients are kept unknown until we have an initial incident condition for $z = 0$, for example a planewave incident is defined as

one of the eigenmodes in the uniform medium. With the initial incident condition set, those coefficients can be obtained for other locations in stead of the incident surface and in turn the field vector can be obtained through those coefficients and the eigenmodes (eigenvectors) of the medium by transfer or scattering matrix which will be discussed later.

$$E=\begin{pmatrix}\vdots\\ E_{ij,x}\\ E_{ij,y}\\ \vdots\end{pmatrix}_{N_p}=\begin{pmatrix}\vdots & \vdots & \cdots & \vdots & \vdots\\ E_{ij,x,1} & E_{ij,x,2} & \cdots & E_{ij,x,2N0-1} & E_{ij,x,2N0}\\ E_{ij,y,1} & E_{ij,y,2} & \cdots & E_{ij,y,2N0-1} & E_{ij,y,2N0}\\ \vdots & \vdots & \cdots & \vdots & \vdots\\ & & & & \end{pmatrix}\begin{pmatrix}\vdots\\ E_l^+(z)\\ \vdots\end{pmatrix}_{N_p}+$$
$$\begin{pmatrix}\vdots & \vdots & \cdots & \vdots & \vdots\\ E_{ij,x,1} & E_{ij,x,2} & \cdots & E_{ij,x,2N0-1} & E_{ij,x,2N0}\\ E_{ij,y,1} & E_{ij,y,2} & \cdots & E_{ij,y,2N0-1} & E_{ij,y,2N0}\\ \vdots & \vdots & \cdots & \vdots & \vdots\\ & & & & \end{pmatrix}\begin{pmatrix}\vdots\\ E_l^-(z)\\ \vdots\end{pmatrix}_{N_p} \tag{2.35}$$

$$E=S(E^++E^-)=(S,S)\begin{pmatrix}E^+\\ E^-\end{pmatrix} \tag{2.36}$$

The magnetic field's Fourier coefficient vector $H$ (Eq. (2.26)) can be expressed in term of $E^+$ and $E^-$ via the first equation of Eq. (2.27) after one step transformation (Eq.(2.37)). Here in the equation, the operation of $T_1^{-1}\otimes\boldsymbol{\beta}$ means the $l^{th}$ column of $T_1^{-1}$ will multiple $\beta_l$ for each column.

$$\begin{aligned}H&=T_1^{-1}\frac{\partial}{\partial z}E=T_1^{-1}(S,S)\frac{\partial}{\partial z}\begin{pmatrix}E^+\\ E^-\end{pmatrix}\\ &=\mathbf{i}T_1^{-1}\otimes\boldsymbol{\beta}(S,-S)\begin{pmatrix}E^+\\ E^-\end{pmatrix}=(T,-T)\begin{pmatrix}E^+\\ E^-\end{pmatrix}\end{aligned} \tag{2.37}$$

Then we can combine Eq. (2.36) and (2.37) to get a more concise expression of relation between field Fourier coefficient and the weight of eigenmodes in Eq. (2.38).

$$\begin{pmatrix} E(z) \\ H(z) \end{pmatrix} = \begin{pmatrix} S & S \\ T & -T \end{pmatrix} \begin{pmatrix} E^{+}(z) \\ E^{-}(z) \end{pmatrix} \tag{2.38}$$

We agree it is a lengthy and boring derivation to get Eq. (2.38), but there are still a few steps from here to the final transfer (scattering) matrix algorithm.

$$\begin{pmatrix} E^{+}(z+h) \\ E^{-}(z+h) \end{pmatrix} = \begin{pmatrix} e^{i\beta h} & 0 \\ 0 & e^{-i\beta h} \end{pmatrix} \begin{pmatrix} E^{+}(z) \\ E^{-}(z) \end{pmatrix} \tag{2.39}$$

The left hand side and right hand side of Eq. (2.38) are for the same $z$ position. If the macroscopic medium is uniform along $z$ axis, then the eigenmodes (eigenvectors) (i.e. $S$ or $T$) remain the same and weight of the each eigenmode will remain the same but with additional phase factor which is illustrated at Eq. (2.39). We usually set the incident surface position as the $z = 0$ and the incident wave vector is a set of numbers, for example the zero order planewave incidence only have $i = 0, j = 0$ elements nonzero and all other elements are set to zero.

## 2.4 Fourier space Maxwell's Equations for uniform medium

At previous section, we discussed in detail on how to get the relation (Eq. (2.38)) between the field Fourier coefficients ($E$ and $H$) and the weight of eigenmodes ($E^{+}$ and $E^{-}$) for any XY double-periodic structures while uniform along $z$ axis direction. Now in this section, we are going to deal with an easier case, the structure of XY plane is uniform medium. For uniform medium, we do not need to do Fourier transformation to the dielectric function. The Maxwell's Equations (Eq. (2.8)) for uniform medium can be written as Eq. (2.40) where $\varepsilon$ is the dielectric constant of the uniformed medium. Now with one step further (Eq. (2.41)), we

can get the vector wave equation expressed as Eq. (2.42) where $n = \sqrt{\varepsilon}$ , the refractive index of the uniform medium. Then the planewave solution can be found from Eq. (2.42).

$$\begin{aligned}
&\mathbf{H}(\mathbf{r}) = \frac{1}{\mathbf{i}k_0}\nabla \times \mathbf{E}(\mathbf{r}) \\
&\nabla \times \left( \frac{1}{\mathbf{i}k_0}\nabla \times \mathbf{E}(\mathbf{r}) \right) = -\mathbf{i}k_0 \varepsilon \mathbf{E}(\mathbf{r})
\end{aligned} \tag{2.40}$$

$$\begin{aligned}
&\nabla \times \left( \nabla \times \mathbf{E}(\mathbf{r}) \right) = k_0^2 \varepsilon \mathbf{E}(\mathbf{r}) \\
&\nabla \times \left( \nabla \times \mathbf{E}(\mathbf{r}) \right) = \nabla \left( \nabla \bullet \mathbf{E}(\mathbf{r}) \right) - \nabla^2 \mathbf{E}(\mathbf{r}) \\
&\nabla \bullet \mathbf{D}(\mathbf{r}) = \nabla \bullet \varepsilon \mathbf{E}(\mathbf{r}) = \varepsilon \nabla \bullet \mathbf{E}(\mathbf{r}) = 0
\end{aligned} \tag{2.41}$$

$$\begin{aligned}
&\nabla^2 \mathbf{E}(\mathbf{r}) + \left( nk_0 \right)^2 \mathbf{E}(\mathbf{r}) = 0 \\
&\mathbf{H}(\mathbf{r}) = \frac{1}{\mathbf{i}k_0}\nabla \times \mathbf{E}(\mathbf{r}) \\
&k_0^2 = \frac{\omega^2}{c^2} = k_{0x}^2 + k_{0y}^2 + k_{0z}^2 \\
&\beta_{ij}^2 = \left( nk_0 \right)^2 - k_{ij,x}^2 - k_{ij,y}^2
\end{aligned} \tag{2.42}$$

If the same definition of column vector of $E$ and $H$ (Eq. (2.26)) is used, then the relation of $E$ and $H$ are expressed at Eq. (2.43), with $S_0$ unit matrix and $T_0$ block diagonal matrix.

$$\begin{aligned}
&\begin{pmatrix} E(z) \\ H(z) \end{pmatrix} = \begin{pmatrix} S_0 & S_0 \\ T_0 & -T_0 \end{pmatrix} \begin{pmatrix} E_0^+(z) \\ E_0^-(z) \end{pmatrix} \equiv \begin{pmatrix} S_0 & S_0 \\ T_0 & -T_0 \end{pmatrix} \begin{pmatrix} \Omega^+(z) \\ \Omega^-(z) \end{pmatrix} \\
&S_0 = I \\
&T_0^{ij} = \frac{1}{k_0 \beta_{ij}} \begin{pmatrix} -k_{ij,x} k_{ij,y} & k_{ij,x}^2 - \beta_{ij}^2 \\ -k_{ij,y}^2 + \beta_{ij}^2 & k_{ij,x} k_{ij,y} \end{pmatrix}
\end{aligned} \tag{2.43}$$

After the above relation is obtained, we can go to the next stage of building transfer and scattering matrix along the propagation direction for uniform or XY double periodicity structures.

## 2.5 Building the transfer matrix and scattering matrix

The transfer (scattering) matrix method is based on the linkage between neighborhood tangential field vectors. For any arbitrary 3D problem, we can always cut the 3D problem to 2D slices along the propagation direction and assume the dielectric distribution is only a function of coordinate $x$ and $y$ within each 2D slice (i.e. the dielectric material along $z$ direction is constant). Some structures can satisfy this assumption exactly and naturally, for example: the layer-by-layer woodpile structure in which each layer has the same dielectric distribution along $z$ direction. Some structure can approximately satisfy this assumption if the slices are thin enough along the $z$ direction, for example: those structures with continuous change dielectric distribution along $z$ direction.

At Figure 2-2 the scheme of transfer matrix method is illustrated. For each 2D slices, we assume there are two infinitely thin air (or any other uniform medium) films around it. These artificial air films will make no impact on the problem because the thickness of them is set to be zero. The purpose of those artificial air films is to connect tangential component of the electromagnetic field throughout the whole structure. And in turn get the transfer matrix and scattering matrix of the whole structure.

The fact that the tangential components of electric and magnetic field are continues is the key to get the field vector connected between neighbors. At the air films and within the slices of left hand side of slice $i$ (position $z_{i-1}$), we have the boundary condition matched at Eq. (2.44). At the air films and within the slices of right hand side of slice $i$ (position $z_i$), we have the boundary condition matched at Eq. (2.45). Also there is a connection between the vector within the slice's left and right boundary Eq. (2.46) in which the thickness of the slice is $h$.

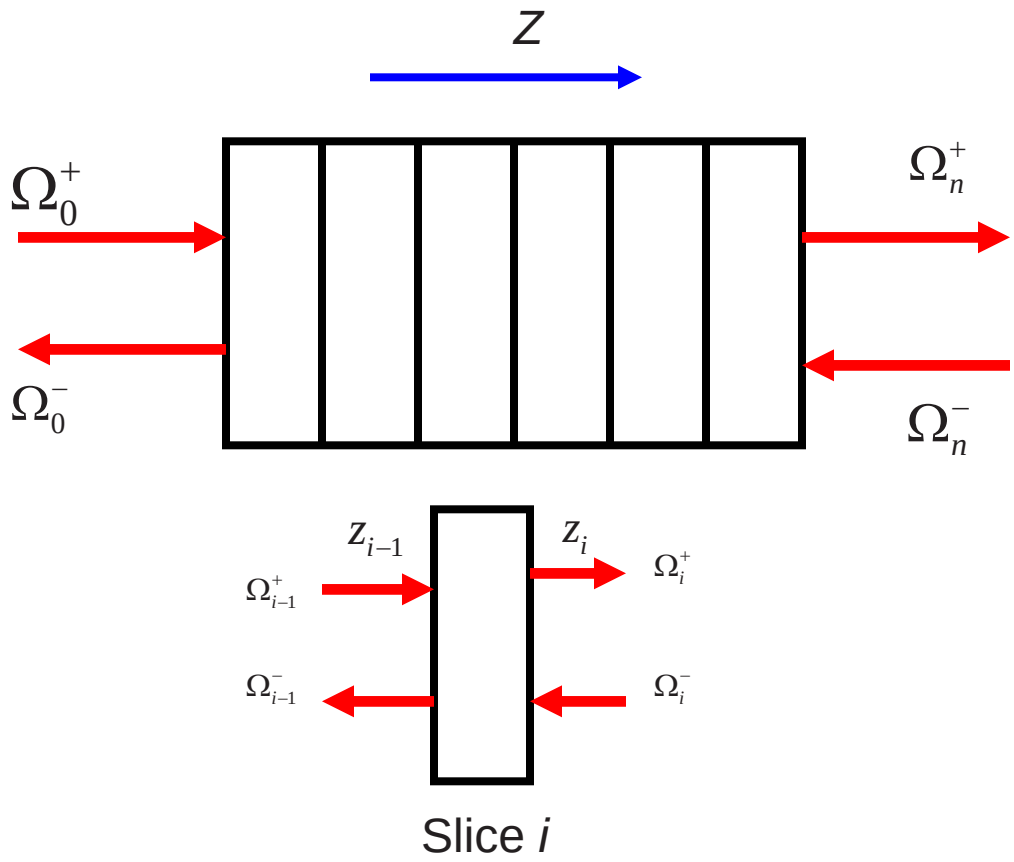


Figure 2-2: Scheme of transfer (scattering) matrix method

$$\begin{pmatrix} S_0 & S_0 \\ T_0 & T_0 \end{pmatrix}\begin{pmatrix} \Omega_{i-1}^+ \\ \Omega_{i-1}^- \end{pmatrix} = \begin{pmatrix} S_i & S_i \\ T_i & T_i \end{pmatrix}\begin{pmatrix} E_i^+(z_{i-1}) \\ E_i^-(z_{i-1}) \end{pmatrix} \tag{2.44}$$

$$\begin{pmatrix} S_i & S_i \\ T_i & T_i \end{pmatrix}\begin{pmatrix} E_i^+(z_i) \\ E_i^-(z_i) \end{pmatrix} = \begin{pmatrix} S_0 & S_0 \\ T_0 & T_0 \end{pmatrix}\begin{pmatrix} \Omega_i^+ \\ \Omega_i^- \end{pmatrix} \tag{2.45}$$

$$\begin{pmatrix} E_i^+(z_{i+1}) \\ E_i^-(z_{i+1}) \end{pmatrix} = \begin{pmatrix} e^{i\beta h} & 0 \\ 0 & e^{-i\beta h} \end{pmatrix}\begin{pmatrix} E_i^+(z_i) \\ E_i^-(z_i) \end{pmatrix} \tag{2.46}$$

$$with: \quad z_{i+1} = z_i + h$$

From the above three equations, we can eliminate $E_i^+$ and $E_i^-$, and get a relation between the left air film and the right air film at Eq. (2.47). We can define $\mathbf{T}_i$ as the transfer matrix for

the $i$ th slice. And the overall transfer matrix ($\mathbf{T}$ matrix) for the whole structure is given by Eq. (2.49).

$$\begin{pmatrix} \Omega_i^+ \\ \Omega_i^- \end{pmatrix} = \begin{pmatrix} a_{11} & a_{12} \\ a_{21} & a_{22} \end{pmatrix}^{-1} \begin{pmatrix} e^{i\beta h} & 0 \\ 0 & e^{-i\beta h} \end{pmatrix} \begin{pmatrix} a_{11} & a_{12} \\ a_{21} & a_{22} \end{pmatrix} \begin{pmatrix} \Omega_{i-1}^+ \\ \Omega_{i-1}^- \end{pmatrix}$$

$$a_{11} = \frac{1}{2}(S_i^{-1}S_0 + T_i^{-1}T_0), \quad a_{22} = a_{11} \tag{2.47}$$

$$a_{12} = \frac{1}{2}(S_i^{-1}S_0 - T_i^{-1}T_0), \quad a_{21} = a_{12}$$

$$\mathbf{T}_i = \begin{pmatrix} t_{11}^i & t_{12}^i \\ t_{21}^i & t_{22}^i \end{pmatrix} = \begin{pmatrix} a_{11} & a_{12} \\ a_{21} & a_{22} \end{pmatrix}^{-1} \begin{pmatrix} e^{i\beta h} & 0 \\ 0 & e^{-i\beta h} \end{pmatrix} \begin{pmatrix} a_{11} & a_{12} \\ a_{21} & a_{22} \end{pmatrix} \tag{2.48}$$

$$\begin{pmatrix} \Omega_i^+ \\ \Omega_i^- \end{pmatrix} = \mathbf{T}_i \begin{pmatrix} \Omega_i^+ \\ \Omega_i^- \end{pmatrix}$$

$$\mathbf{T} = \mathbf{T}_n \mathbf{T}_{n-1} \mathbf{T}_{n-2} \bullet\bullet\bullet \mathbf{T}_1 \tag{2.49}$$

But the $\mathbf{T}$ matrix has been proved to be numerically unstable when the structure along the propagation direction is thick, which is due to the fact that the evanescent wave components in the planewave expansion will increase exponentially if entire $\mathbf{T}$ matrixes are multiplied. In other word, the exponential increase term accumulation makes the poor numerical stability for $\mathbf{T}$ matrix.

One solution to the $\mathbf{T}$ matrix problem is adopting the scattering matrix ($\mathbf{S}$ matrix) method expressed at Eq. (2.50). The overall $\mathbf{S}$ matrix can be found by connecting $\mathbf{S}$ matrix at each slice through an iteration algorithm. Suppose the first $n-1$ $\mathbf{S}$ matrix is $\mathbf{S^{n-1}}$ and the $\mathbf{S}$ matrix for the $n$ th slice is $\boldsymbol{s}^{\mathbf{n}}$, then the $\mathbf{S}$ matrix for the total $n$ slices will be $\mathbf{S^n}$ which is given by Eq. (2.51). In the real calculation, we first set $\mathbf{S}$ matrix to be $I$, the identity matrix, which represents $\mathbf{S}$ matrix of an air slice, then use the iteration algorithm to get the total

$\mathbf{S}$ matrix of the first slices and $I$. Then apply the iteration algorithm to all the other slices to get the total $\mathbf{S}$ matrix for the whole structure.

$$
\begin{aligned}
p_1 &= [a_{11} - e^{i\beta h} a_{12} a_{11}^{-1} e^{i\beta h} a_{12}]^{-1} \\
p_2 &= a_{11}^{-1} e^{i\beta h} a_{12} \\
t_1 &= a_{11}^{-1} e^{i\beta h} a_{12} [a_{11} - e^{i\beta h} a_{12} a_{11}^{-1} e^{i\beta h} a_{12}]^{-1} \\
t_2 &= -a_{12}
\end{aligned}
$$

$$
\mathbf{S}_i = \begin{pmatrix} s_{11}^i & s_{12}^i \\ s_{21}^i & s_{22}^i \end{pmatrix} = \begin{pmatrix} p_1 t_1 + p_2 t_2 & p_1 t_2 + p_2 t_1 \\ p_1 t_2 + p_2 t_1 & p_1 t_1 + p_2 t_2 \end{pmatrix} \tag{2.50}
$$

$$
\begin{pmatrix} \Omega_i^+ \\ \Omega_{i-1}^- \end{pmatrix} = \mathbf{S}_i \begin{pmatrix} \Omega_{i-1}^+ \\ \Omega_i^- \end{pmatrix}
$$

$$
\begin{aligned}
\boldsymbol{S}_{11}^n &= \boldsymbol{s}_{11}^n [I - \boldsymbol{S}_{12}^{n-1} \boldsymbol{s}_{21}^n]^{-1} \boldsymbol{S}_{11}^{n-1} \\
\boldsymbol{S}_{12}^n &= \boldsymbol{s}_{12}^n + \boldsymbol{s}_{11}^n \boldsymbol{S}_{12}^{n-1} [I - \boldsymbol{s}_{21}^n \boldsymbol{S}_{12}^{n-1}]^{-1} \boldsymbol{S}_{22}^n \\
\boldsymbol{S}_{21}^n &= \boldsymbol{s}_{21}^{n-1} + \boldsymbol{S}_{22}^{n-1} \boldsymbol{s}_{21}^n [I - \boldsymbol{S}_{12}^{n-1} \boldsymbol{s}_{21}^n]^{-1} \boldsymbol{S}_{11}^{n-1} \\
\boldsymbol{S}_{22}^n &= \boldsymbol{S}_{22}^{n-1} [I - \boldsymbol{s}_{21}^n \boldsymbol{S}_{12}^{n-1}]^{-1} \boldsymbol{s}_{22}^n
\end{aligned} \tag{2.51}
$$

Finally, we obtained a numerical stable scattering matrix $\mathbf{S}$ for the whole structure. And the $\mathbf{S}$ matrix has the internal electrodynamics properties of this particular structure. Tile now, we are only transforming the Maxwell's Equations with certain dielectric distribution. There are still no initial conditions or boundary conditions (except the XY double periodicity) applied to our structure. For different purpose, such as spectrum, band diagram or mode profile, we can apply desired initial condition and boundary condition to the $\mathbf{S}$ matrix.

## 2.6 Using scattering matrix for various applications

In this section, we will discuss several direct applications from the calculated $\mathbf{S}$ matrix to get the spectrum, the band structure and the electric and magnetic field distributions (mode

profiles). Detailed derivations are supplied with actual calculation examples from published results. More applications can be added to this transfer (scattering) matrix scheme for future development.

### 2.6.1 Spectrum from S matrix

Now let's review Figure 2-2 and suppose that the **S** matrix for the whole structure is known. Then we have relation Eq. (2.52) which connects the field column vector at left and right side of the photonic crystal structure. To get the spectrum, we need a boundary condition: the incident electromagnetic wave $E_0$ can be expressed by $\Omega_0^+$ (for a simple planewave incident only the center element ($i = 0, j = 0$) is set to 1 and all the other elements are set to 0) and $\Omega_n^-$ is set to zero because there are no propagating waves to the structure from left hand side. With this boundary condition and the knowledge of **S** matrix, we can get the column vector $\Omega_n^+$ and $\Omega_0^-$ which represent the transmission and reflection field component vectors.

$$\begin{pmatrix} \Omega_n^+ \\ \Omega_0^- \end{pmatrix} = \mathbf{S} \begin{pmatrix} \Omega_0^+ \\ \Omega_n^- \end{pmatrix} \qquad (2.52)$$
$$E_t = S_{11}E_0, E_r = S_{21}E_0$$

After the transmission and reflection coefficient are obtained, we can get the electric field and magnetic field. The transmittance or reflectance rate is the ratio of energy flux of transmission wave or reflection wave toward incident wave.

The energy flux is proportional to the Poynting vector $\mathbf{P} = \mathbf{E} \times \mathbf{H}$. The ratio of Poynting vector magnitude gives the transmittance or reflectance. The absorptance is defined as one minus the transmittance minus the reflectance. Those relations are summarized at Eq. (2.53) with the summation of $ij$ for lateral wave vector $k_{ij,x}^2 + k_{ij,y}^2 \le k_0^2$ in which all the modes are propagation mode.

$$\mathbf{H} = \frac{\mathbf{k} \times \mathbf{E}}{k_0}$$
$$T = \frac{\mathbf{E^t} \times \mathbf{H^t}}{\mathbf{E}_0 \times \mathbf{H}_0} = \sum_{ij} \frac{|E_{ij}^t|^2 |\beta_{ij}|}{|E_0|^2 |k_{0z}|} \qquad (2.53)$$
$$R = \frac{\mathbf{E^r} \times \mathbf{H^r}}{\mathbf{E}_0 \times \mathbf{H}_0} = \sum_{ij} \frac{|E_{ij}^r|^2 |\beta_{ij}|}{|E_0|^2 |k_{0z}|}$$
$$A = 1 - T - R$$

To show an example of our transfer (scattering) matrix calculation result, we select one text book structure: 10 layers of alternating slabs, one has dielectric constant 13 and the other has dielectric constant 1, both has thickness $0.5a$ where $a$ is the lattice constant.

Figure 2-3 is our transfer (scattering) matrix result which shows a band gap between normalized frequencies around 0.15 to 0.25 which is consistent with the text book result.

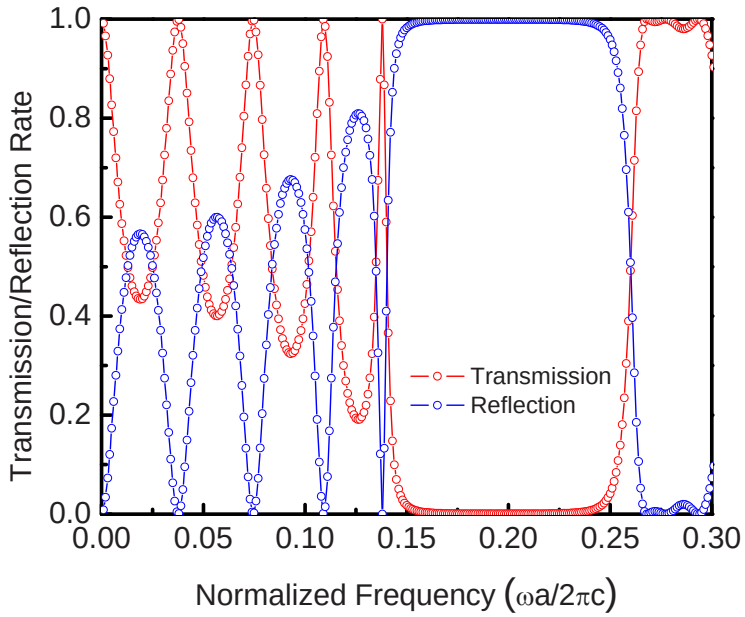


Figure 2-3: Spectrum of 1D photonic crystal

### 2.6.2 Band structure from S matrix

There are several methods to get band structure from the **S** matrix, Dr. Zhi-Yuan Li mentioned three different schemes. Here I only discuss the one which is used in my transfer (scattering) matrix simulation package. To get the photonic band structure, we need impose a periodic boundary condition along the stacking direction (i.e. the selected wave propagation direction) to simulate infinite structure,. According to Bloch's theorem, the relation of field components at position $\mathbf{r}$ and position $\mathbf{r}+\mathbf{R}$ satisfies Eq. (2.54) with $\mathbf{R}$ the periodicity.

$$u(\mathbf{r}+\mathbf{R}) = e^{i\mathbf{k}\cdot\mathbf{R}}u(\mathbf{r}) \tag{2.54}$$

If we take the desired direction alone $\mathbf{a_3}$ as the role of $\mathbf{R}$ to calculate the band diagram alone this particular direction, then the $\mathbf{S}$ matrix between point $\mathbf{r}$ and point $\mathbf{r}+\mathbf{R}$ can be obtained according previous sections. After the $\mathbf{S}$ matrix is ready, we can write out the field components at position $\mathbf{r}$ and $\mathbf{r}+\mathbf{a}_3$ as in Eq. (2.56) from the Bloch's theorem. Rearrange Eq. (2.55) and Eq. (2.56), we can get Eq. (2.57) which is a standard generalized eigen-problem $Ax = \lambda Bx$ with $A$ and $B$ are both square matrices.

$$\begin{pmatrix} \Omega_1^+ \\ \Omega_0^- \end{pmatrix} = \mathbf{S} \begin{pmatrix} \Omega_0^+ \\ \Omega_1^- \end{pmatrix} \tag{2.55}$$

$$\begin{pmatrix} \Omega_1^+ \\ \Omega_1^- \end{pmatrix} = e^{i\mathbf{k}\cdot\mathbf{a}_3} \begin{pmatrix} \Omega_0^+ \\ \Omega_0^- \end{pmatrix} \tag{2.56}$$

$$\begin{pmatrix} S_{11} & 0 \\ S_{21} & -I \end{pmatrix} \begin{pmatrix} \Omega_0^+ \\ \Omega_0^- \end{pmatrix} = e^{i\mathbf{k}\cdot\mathbf{a}_3} \begin{pmatrix} I & -S_{12} \\ 0 & -S_{21} \end{pmatrix} \begin{pmatrix} \Omega_0^+ \\ \Omega_0^- \end{pmatrix} \tag{2.57}$$

In this approach, normalized frequency $\omega$ and lateral Bloch's vector $k_x$ and $k_y$ are given explicitly as input parameters, while $k_z$ is left to be determined; or in function form: $k_z = f(\omega, k_x, k_y)$. To find $k_z$, we adopted a widely used "on shell" approach: for propagating mode, $k_z$ must be a real number which imply that the eigenvalue of $e^{\mathbf{ik}\cdot\mathbf{a}_3}$ must be a complex number of unity modulus. In the calculation, first we solved the eigenvalue problem Eq. (2.57), then pick up all the eigenvalues of module equals one, and then get $k_z$ from corresponding eigenvalues.

When we solve the band diagram by this approach, the material to build the photonic crystal can be dispersive which due to the fact that each solution is for individual frequency point. One disadvantage of this approach is that: for each direction along the Brillouin Zone, we need calculate **S** matrix and solve eigenvalue problem individually which means we need to cut the 3D photonic crystal through different directions to get a complete band diagram. To illustrate the usage of our simulation package, we repeat the calculation of 1D photonic crystal with alternating material slab: one layer with dielectric constant 13 and thickness $0.2a$ and the other layer with dielectric constant 1 and thickness $0.8a$ where $a$ is the lattice constant. Consistent result is obtained when compared with our TMM results.

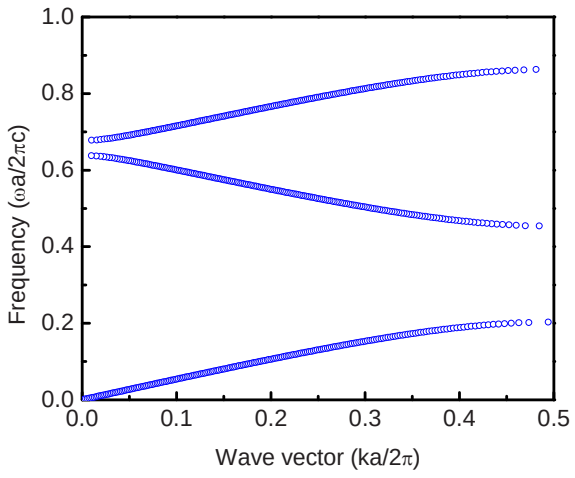


Figure 2-4: Band diagram of 1D photonic crystal

### 2.6.3 Field mode profile from S matrix

One other property we are interested in is the field mode profile across the photonic crystal structures. To get the electromagnetic field distribution at any intermediate plane within the photonic crystal structure, we need to use the two-side **S** matrix formulation. For any given intermediate plane $Z_a$, the whole photonic crystal structure is divided into two parts: the front part and the back part with each part have one **S** matrix: $\mathbf{S}_1$ for front part and $\mathbf{S}_2$ for back part. Figure 2-5 gives a sketch of the two-side **S** matrix scheme.

We can find that the arbitrary intermediate field vectors $E_a^+$ and $E_a^-$ are related to the $E_0$, $E_t$ and $E_r$ through Eq. (2.58) from which we can get Eq. (2.59).

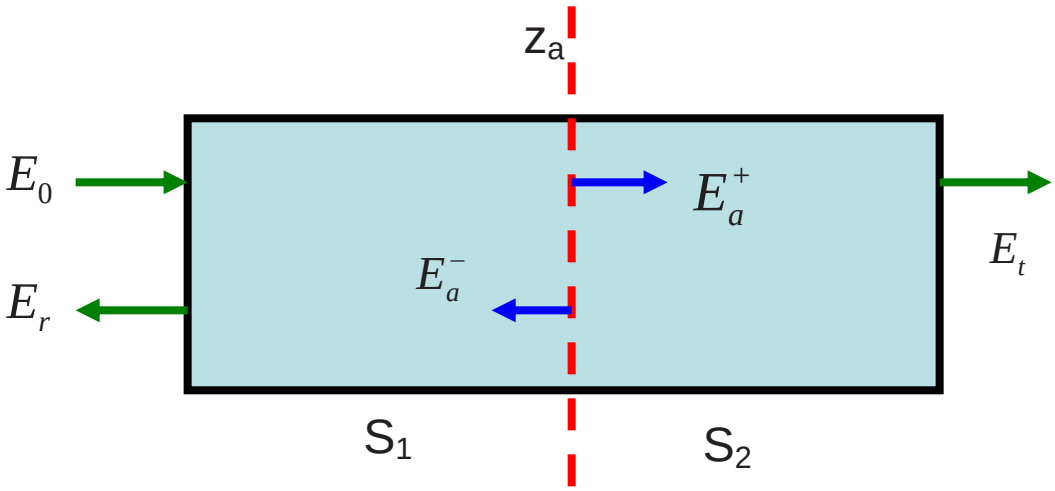


Figure 2-5: Two-side S matrix scheme

$$\begin{pmatrix} E_a^+ \\ E_r \end{pmatrix} = \begin{pmatrix} S_1^{11} & S_1^{12} \\ S_1^{21} & S_1^{22} \end{pmatrix} \begin{pmatrix} E_0 \\ E_a^- \end{pmatrix}$$
$$\begin{pmatrix} E_t \\ E_a^- \end{pmatrix} = \begin{pmatrix} S_2^{11} & S_2^{12} \\ S_2^{21} & S_2^{22} \end{pmatrix} \begin{pmatrix} E_a^+ \\ 0 \end{pmatrix} \qquad (2.58)$$

$$\begin{aligned} E_a^+ &= S_1^{11}E_0 + S_1^{12}E_a^- \\ E_r &= S_1^{21}E_0 + S_1^{22}E_a^- \\ E_t &= S_2^{11}E_a^+ \\ E_a^- &= S_2^{21}E_a^+ \end{aligned} \tag{2.59}$$

Combining first and forth equation of Eq. (2.59), we can get the first equation of Eq. (2.60) which is a standard linear algebra problem ( $Ax = B$ ) and can be solved easily. After getting $E_a^+$ , we can use the second equation of Eq. (2.60) to calculate $E_a^-$ .

$$\begin{aligned} (I - S_1^{12}S_2^{21})E_a^+ &= S_1^{11}E_0 \\ E_a^- &= S_2^{21}E_a^+ \end{aligned} \tag{2.60}$$

$E_a^+$ and $E_a^-$ are the column vectors of $E_{ij,x}^{\pm}$ for the desired slices, or the plane perpendicular to the propagation direction. Then we can use Eq. (2.61) to calculate the electric field of $x$ and $y$ components which are at the infinite thin air film adjacent to the desired plane. According to the boundary condition, the tangential component is continuous, the electric field of $x$ and $y$ components at the photonic crystal structure are the same as in the infinite thin air film.

$$\begin{aligned} E_x(\mathbf{r}) &= \sum_{m=-N_x}^{N_x}\sum_{n=-N_y}^{N_y}\left(E_{mn,x}^+ + E_{mn,x}^-\right)e^{\mathbf{i}(k_{mn,x}x+k_{mn,y}y)} \\ E_y(\mathbf{r}) &= \sum_{m=-N_x}^{N_x}\sum_{n=-N_y}^{N_y}\left(E_{mn,y}^+ + E_{mn,y}^-\right)e^{\mathbf{i}(k_{mn,x}x+k_{mn,y}y)} \\ E_z(\mathbf{r}) &= \sum_{m=-N_x}^{N_x}\sum_{n=-N_y}^{N_y}\left(E_{mn,z}^+ + E_{mn,z}^-\right)e^{\mathbf{i}(k_{mn,x}x+k_{mn,y}y)} \end{aligned} \tag{2.61}$$

To get electric field $z$ component at the air film, we need use Maxwell's Equations $\nabla\bullet\mathbf{D} = \nabla\bullet\varepsilon_0\mathbf{E} = 0$ which leads to $\nabla\bullet\mathbf{E} = 0$ . So $E_{ij,z}$ can be found easily by Eq. (2.62).

$$E_{ij,z} = \frac{1}{k_{ij,z}}\left(k_{ij,x}E_{ij,x} + k_{ij,y}E_{ij,y}\right) \tag{2.62}$$

But $E_z(\mathbf{r})$ inside the photonic crystal structure is not same as in the infinite air film. To get correct $E_z(\mathbf{r})$ inside the photonic crystal structure we need apply the boundary condition of the continuity of $D_z$ field: $D_{z0} = D_{z1} \Rightarrow \varepsilon_0 E_{z0} = \varepsilon_1 E_{z1} \Rightarrow E_{z1} = \varepsilon_1^{-1}\varepsilon_0 E_{z0}$ . But we can not apply this condition directly in real space; instead we need to apply it to the Fourier space. Here we use the Fourier expansion of $\varepsilon_{ij}^{-1}$ instead of $\varepsilon_{ij}$ for this problem. Finally we can get the electric field $z$ component vector as the last equation of (2.63), then we can apply the last equation of (2.61) to get the electric field distribution of $E_z(\mathbf{r})$ inside the photonic crystal structures.

For magnetic field $H$, we can first try to obtain the $H$ field vector of $x, y$ components at air film through the $E$ field vector by Eq. (2.64). Then the $z$ component can be figured out by $\nabla \bullet \mathbf{H} = 0$ or Eq. (2.65). Then follow the similar procedure as Eq. (2.61) to get the magnetic field distribution inside the photonic crystal of all three components.

$$\begin{aligned}
&\sum_{ij} E_{ij,z}^{PhC}(z)e^{\mathbf{i}(k_{ij,x}x+k_{ij,y}y)} \\
&= \varepsilon_0 \sum_{ij} E_{ij,z}^{air}(z)e^{\mathbf{i}(k_{ij,x}x+k_{ij,y}y)} \sum_{ij} \varepsilon_{ij}^{-1} e^{\mathbf{i}(k_{ij,x}x+k_{ij,y}y)} \\
&= \sum_{ij}\sum_{mn} \varepsilon_{i-m,j-n}^{-1} E_{mn,z}^{air}(z)e^{\mathbf{i}(k_{ij,x}x+k_{ij,y}y)} \\
&\Rightarrow E_{ij,z}^{PhC}(z) = \sum_{mn} \varepsilon_{i-m,j-n}^{-1} E_{mn,z}^{air}(z)
\end{aligned} \tag{2.63}$$

$$\begin{aligned}
\begin{pmatrix} H_{ij,x}^{+} \\ H_{ij,y}^{+} \end{pmatrix} &= \frac{1}{k_0\beta_{ij}} \begin{pmatrix} -k_{ij,x}k_{ij,y} & k_{ij,x}^2 - \beta_{ij}^2 \\ -k_{ij,y}^2 + \beta_{ij}^2 & k_{ij,x}k_{ij,y} \end{pmatrix} \begin{pmatrix} E_{ij,x}^{+} \\ E_{ij,y}^{+} \end{pmatrix} \\
\begin{pmatrix} H_{ij,x}^{-} \\ H_{ij,y}^{-} \end{pmatrix} &= \frac{-1}{k_0\beta_{ij}} \begin{pmatrix} -k_{ij,x}k_{ij,y} & k_{ij,x}^2 - \beta_{ij}^2 \\ -k_{ij,y}^2 + \beta_{ij}^2 & k_{ij,x}k_{ij,y} \end{pmatrix} \begin{pmatrix} E_{ij,x}^{-} \\ E_{ij,y}^{-} \end{pmatrix}
\end{aligned} \tag{2.64}$$

$$H_{ij,z} = \frac{1}{k_{ij,z}}\left(k_{ij,x}H_{ij,x} + k_{ij,y}H_{ij,y}\right) \qquad (2.65)$$

Now I am going to close this review chapter of introduction for transfer (scattering) matrix method. It is only the core knowledge of this numerical tool. There are a lot of other aspects to make this method a good simulation tool, such as applying structure symmetry, introducing perfectly matched layer boundary condition instead of periodic boundary condition, pre calculation analysis and post calculation analysis, various input waves instead zero order plane wave (for example higher-order plane wave, Gaussian wave, waveguide eigenmode etc.) and the flexibility to deal with different materials (such as dispersive, anisotropic, or magnetic materials). Some of those topics will be discussed in this thesis and some are not. It is still a developing method, and new concepts and strategies are very likely to be introduced soon.

**References:**


1. John D. Joannopoulos, *Photonic crystal – Molding the Flow of Light*, Princeton University Press, 1995
2. Steven G Johnson, *Photonic crystal – The road from theory to practice*, Kluwer Academic Publishers, 2002
3. J. D. Jackson , *Classical Electrodynamics*, 3rd edition, Wiley & Sons Press, 2004
4. M. Born and E. Wolf, *Principles of Optics*, 7th edition, Cambridge University Press, 1999
5. Z. Li and L. Lin, "Photonic band structures solved by a plane-wave-based transfer-matrix method", *Phys. Rev. E* **67**, 046607, (2003)
6. L. Lin, Z. Li and K. Ho, "Lattice symmetry applied in transfer-matrix methods for photonic crystals ", *J. Appl. Phys.* **94**, 811 (2003)

7. Z.Y. Li and K.M. Ho, "Application of structural symmetries in the plane-wave-based transfer-matrix method for three-dimensional photonic crystal waveguides", *Phys. Rev. B* **68**, 245117 (2003)
8. Z.Y. Li and K.M. Ho, "Light propagation in semi-infinite photonic crystals and related waveguide structures", *Phys. Rev. B* **68**, 155101 (2003)
9. Z.Y. Li and K.M. Ho, "Analytic modal solution to light propagation through layer-by-layer metallic photonic crystals", *Phys. Rev. B* **67**, 165104 (2003)
10. Z.Y. Li and K.M. Ho, "Bloch mode reflection and lasing threshold in semiconductor nanowire laser arrays", *Phys. Rev. B* **71**, 045315 (2005)

# Chapter 3. Interpolation for spectra calculation

One of the most important applications of photonic crystal is introducing point defects (i.e. cavity) into the pure photonic crystal structure to make a photonic crystal resonant cavity which can be widely used in solid state laser (acting as the resonant cavity) and communication industry. The advantage of photonic crystal resonant cavity compared with conventional resonant cavity is: first due to the present of photonic crystal background, the Q value can be very large; second the size of the resonant cavity can be very small and compact. Those two properties is the key to improve the solid state laser performance and properties. And how to efficiently and accurately get the exact resonant peak frequency, the Q value and electric field mode profiles are essential for laser resonant cavity design.

The planewave based transfer (scattering) matrix method is a frequency domain method and spectra can be calculated at any arbitrary resolutions, i.e. arbitrary small or large frequency steps. There are maybe several resonant peaks inside the photonic band gap frequency region, and we have no idea where those resonant modes located and what is the Q value before the whole spectra is obtained. To get all possible resonant modes, very high spectra resolution is required, ideally continues spectra are preferred. The calculation for each frequency data point is almost identical, so increase the resolution will increase the calculation time linearly. We can not get continues spectra due to the calculation time limitation. Typically, getting around less than 100 frequency data points in the band gap range of the spectra is acceptable in term of time consumption for 3D structures.

For a typical transmission spectrum through a GaN woodpile photonic crystal structure with the band gap ranges from around 0.50 $\mu m$ to 0.60 $\mu m$, if the resonant mode of Q value is around 10,000 and resonant frequency 0.55 $\mu m$, then we need at least the spectrum to have a

resolution of $5.5\times10^{-5}\ \mu m$ or 1818 data points to barely see this resonant peak. A Q value of 10,000 is only moderate in photonic crystal cavities, recently S. Noda reported a photonic crystal cavity with Q value as large as 1,000,000. To get a way out of this challenge, we introduced interpolation into our planewave based transfer (scattering) matrix method. In this chapter, the theoretical foundation is discussed with one example of application of this concept to the woodpile layer-by-layer photonic crystal cavities.

## 3.1 Why interpolation works?

As we have already known that all the spectra from Maxwell's Equations are Lorentzian shape which can be determined by several parameters, one naturally asked question is can we use as few as possible spectrum data points to get an acceptable estimate of those parameters and in turn get the analytical form of the spectrum? There are two types of methods to answer the above question, one is interpolation and the other is regression.

Regression is a statistic way to figure out the unknown parameter by minimizing the fitting error. Typically a large set of data is required to get good results. In our case, we know the spectra are Lorentzian and we have to use the so called non-linear regression strategy. It may help a little bit in the analysis with adequate data points, but this is not we want to do. Can we just use a few data points while still get accurate results? The answer goes to interpolation. Interpolation uses only very few data points but with the knowledge of what the function form (with a few undecided parameters). It just like solve a function with unknown variables: for example if there are 2 unknown parameters $(a,b)$ in one function $y = f(a,b,x)$ with the form $f(a,b,x)$ explicit, we can only use two set of $(x,y)$ to get the unknown parameter. But this is only true for those two set of $(x,y)$ are exactly acquired from experiments or calculation. Error is usually introduced for experiments and certain numerical simulations. The biggest difference between regression and interpolation is: the interpolated function will go through each data points while the regressed function may or may not go through each

data points. There are two key points to use interpolation for the planewave based transfer (scattering) matrix method spectra data points: first we know the exact spectra functions form (Lorentzian shape); second each data points are accurate enough.

Now let's start from the most general form of the superposition of multiple peak Lorentzian functions Eq. (3.1) with $\{a_i, b_i, c_i, d_i\}$ total $4m$ independent unknown parameters. With a few steps, the multiple peak Lorentzian function can be written in term of rational function Eq. (3.2) with total of $4m+1$ unknown parameters. With one additional redundancy parameter, we can adopt a widely used, robust and efficient interpolation / extrapolation algorithm for diagonal rational functions. The Bulirsch-Stoer algorithm of the Neville type produces the so called diagonal rational function with the degrees of numerator and denominator equal (if m is even) or with the degree of the denominator larger by one (if m is odd).

One other advantage of using the diagonal rational function interpolation is that in real transmission spectra, there are may be some non-Lorentzian feature which can be handled by rational function instead of Lorentzian function (detailed discussion will be on later sections).

$$f(x) = \sum_{i=1}^{m} \left( a_i + \frac{b_i}{(x - c_i)^2 + d_i^2} \right) \tag{3.1}$$

$$\begin{aligned} f(x) &= \sum_{i=1}^{m} \left( \frac{a_i x^2 - 2a_i c_i x + (a_i c_i^2 + a_i d_i + b_i)}{x^2 - 2c_i x + d_i^2} \right) \\ &= \sum_{i=1}^{m} \left( \frac{P_{3,i} x^2 + P_{4,i} x + P_{5,i}}{x^2 + P_{1,i} x + P_{2,i}} \right) \\ &= \frac{\sum_{i=0}^{2m} p_i x^i}{x^{2m} + \sum_{i=0}^{2m-1} q_i x^i} \end{aligned} \tag{3.2}$$

## 3.2 An example of application of interpolation

This section is modified from a paper published at *Optics Letters* Vol. **31**. No. 2 (page 262) at January 2006 with title: "High-efficiency calculations for three-dimensional photonic crystal cavities", by M. Li, Z. Li, K. Ho, J. Cao, and M. Miyawaki.

Experimental and numerical studies of photonic crystals (PC) have been experiencing exponential growth for more than a decade and numerous scientific and engineering advances have been made. However, with the exception of PC fibers,[1] very few concepts have been able to pass from the scientific research stage to high throughputs mainstream products. Besides the challenges in manufacturing, one of the main reasons behind this situation is the lack of efficient and versatile numerical simulation tools for PC structures, especially defective three-dimensional (3D) PC structures which can be used for waveguides[2,3,4] and resonant cavities.[5,6] There are already established numerical simulation methods.[7,8,9] However, serious consideration of the trade-off between the targeted result accuracy (e.g. resolutions etc.) and the projected computation time is still a daily dilemma faced by researchers working on 3D PC devices. In this letter, we present methods that can minimize this trade-off for cavity embedded 3D PCs. The approach includes a planewave-based transfer matrix method (TMM)[10] and a robust rational function interpolation/extrapolation implementation.[11,12] A significant increase in speed with high numerical accuracy for modeling 3D PC cavity modes was demonstrated based on this approach.

When an incident electromagnetic wave is directed toward a slab of 3D PC, the transmission rate through it should be exponentially attenuated across the whole frequency range of the directional band gap, which contains the full photonic band gap.[13] When there is a cavity mode in the 3D PC slab, the resonant transmission through the cavity will result in a

Lorentzian shape peak in the transmission power spectrum. The peak frequency corresponds to the cavity mode's frequency, and the ratio between the peak frequency and the FWHM (full-width half-maximum) of the peak corresponds to the mode's Q value.[14,15] The stationary electromagnetic field distribution through out the volume is the cavity mode shape, when the incident light is set at the cavity mode's resonant frequency. Therefore, one can in principle characterize every aspects of individual cavity modes based on such transmission calculations. At first sight, however, since we do not know the number of cavity modes and their frequency positions, it appears that for high Q cavity modes corresponding sharp transmission spectral peaks, a large number of frequencies have to be calculated to resolve all the modes in the band gap.

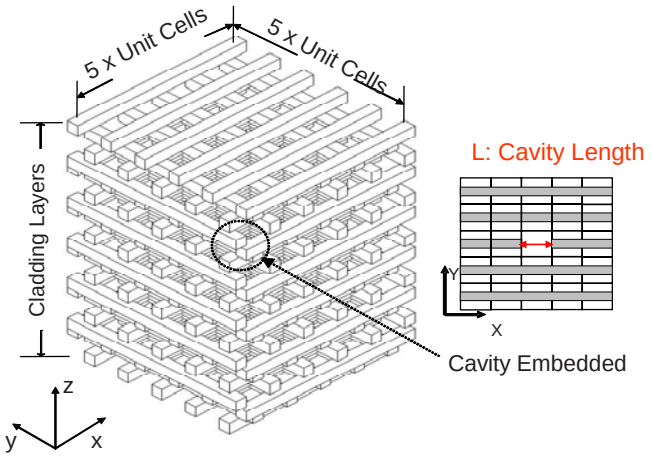


Figure 3-1: A 5-by-5 sized PC cavity supercell structures (left) and cross-section of the cavity layer (right)

To solve this practical challenge, an interpolation/extrapolation strategy was deployed. Unlike the complex frequency domain root searching approach employed before (e.g. reference 16, and similar method has been used in 2D slab PC cavity structures), we utilized a fully global deterministic real frequency domain rational function interpolation/extrapolation formalism: the Stoer-Bulirsch algorithm which does not require explicit initial conditons.[11,12] A sum of Lorentzian peaks which is the general form that any

resonant transmission spectrum should follow is simply a sub-class of diagonal rational functions. Therefore, ideally one can analytically extract every spectral detail at any resolution, once the spectral values at M=4N+1 frequency points are known, for a spectrum that contains equal or less than N resonant peaks. The sampling of those M frequency points can be arbitrary. This fact eliminates the great practical challenge of searching narrow bandwidth resonant peaks across the wide bandwidth span of a photonic band gap.

As a demonstration, we performed numerical simulation for a 3D layer-by-layer PC structure[17] illustrated in Figure 3-1. The refractive index of the rod material is set at 3.015. Both *w/a* and *d/a* ratios are 0.3019, where *w* is the width of each rod in the x-y plane, *d* is the thickness of each rod along the z-orientation, and *a* is the pitch between rods in each layer or is referred as lattice constant in some literatures.[10] The left side of Figure 3-1 is a 3D illustration of a 5-by-5 sized supercell embedded with an optical cavity, where the supercell size is 5*a*×5*a* in the x-y plane. In this study, to characterize the numerical influences of finite supercell sizes, we calculated multiple supercell sizes, including 3-by-3, 4-by-4, 5-by-5 and 6-by-6. All structures in this study (except otherwise specified) have 22 layers along the z-orientation and the optical cavity is formed by removing a section of rod in exactly one lattice constant (*a*) in the $12^{th}$ layer, which is illustrated by a cross-section diagram shown on the right side of Figure 3-1.

The transmission spectrum for the 3-by-3 unit cells with a z-oriented incident beam (both x- and y- polarizations) at 21 discrete sampling frequencies was calculated by TMM, shown as the scattered square symbols in Figure 3-2. Firstly, 13 evenly spaced frequency points were calculated, and the estimated error term from the interpolation of those 13 points indicated more data points were required around normalized frequency 0.44 and 0.445. Then 8 additional frequency points were calculated around 0.44 and 0.445, and interpolation repeated with a total of 21 frequency points. The y-polarization incident does not show any resonant feature throughout the whole directional band gap. The solid blue line in Figure 3-2

is the result of the 100,000 output points for the x-polarization from the 21 data interpolation. The green line in Figure 3-2 is the estimated error term generated by the interpolation routine itself. [11,12] This estimated error term not only provides a direct gauge of the reliability of each interpolation, but also provide a direct indication of where to add more input data points if necessary.

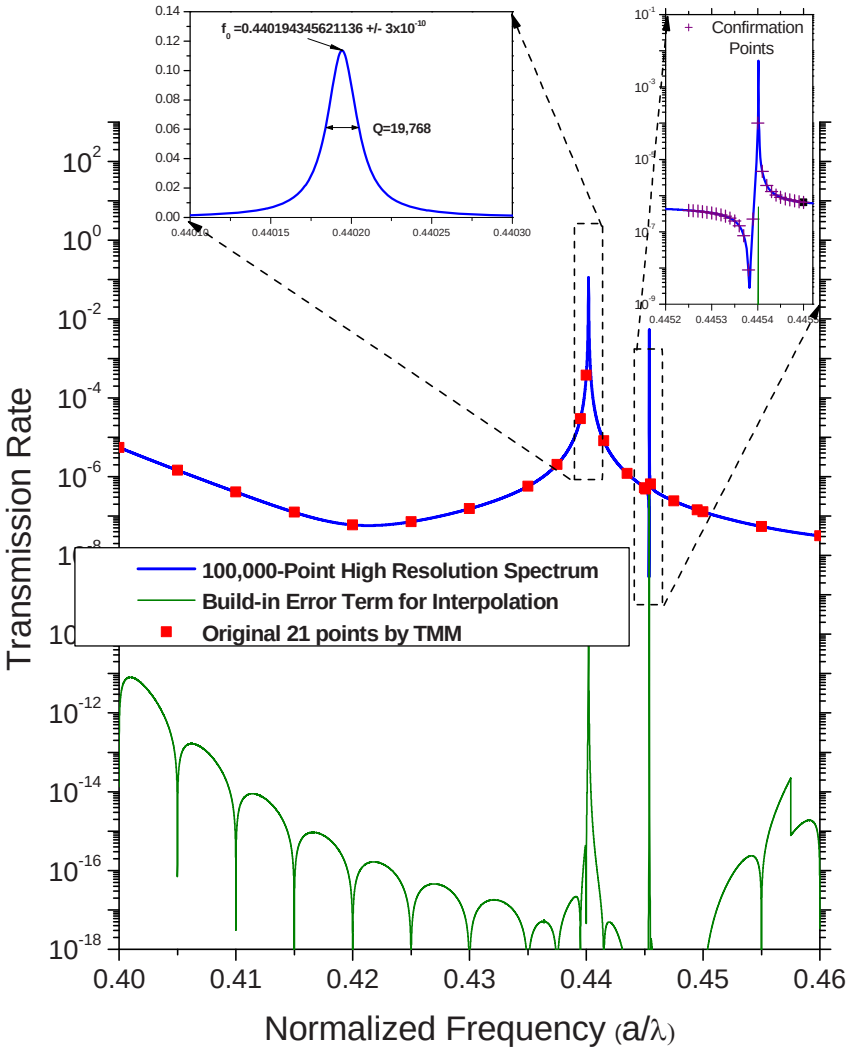


Figure 3-2: The z-directional transmission spectrum (blue line) across the full bandgap range with its estimated error term (green line). The upper-left inset shows a zoom-in linear plot of the Lorentzian resonant transmission peak, with its peak frequency and Q value labeled. The upper-right inset shows a zoom-in view of an asymmetric transmission feature, with 26 confirmation TMM frequency points (purple crosses).

The upper-right inset of Figure 3-2 is a zoom-in view of a sharp and non-Lorentzian feature near the normalized frequency 0.4454. It also shows 26 independent confirmation frequency points (purpule crosses) calculated by TMM. The numerically perfect match between these 26 confirmation data points and the 100,000-point high resolution spectrum (blue line) is a direct proof of the accuracy of the rational function interpolation procedure. This non-Lorentzian feature is not a localized cavity mode which is confirmed by its mode shape calculated in TMM.[18] Namely, its mode shape reveals strong concentration of the electromagnetic field at the two air/PC interfaces, instead of the cavity itself. Although we don't have definite analysis of this specific resonance yet, these non-Lorentzian resonant features are not rare and are also observed in other simpler grating systems.[19]

Such numerically stable and high accuracy performance of the interpolation routine is partially due to the fact that TMM is a frequency domain calculation method. Unlike time domain simulation methods (e.g. Finite-Difference Time-Domain (FDTD)), the individual power spectrum data point calculated from frequency domain methods is the stationary result after the evolution of infinitely long time, without the influences of finite time span convolution effects and/or transient effects. This is the reason why such interpolation can numerically work across a wide bandwidth (e.g. covering the full band gap range in one run), while methods such as the Pade approximation used in conjunction with FDTD programs can only cover much smaller bandwidth for each run in order to correct the convolution effects.[20] The upper-left inset of Figure 3-2 shows a zoom-in view of the Lorentzian peak near normalized frequency 0.4402, which corresponds to a localized cavity mode of interest. Plotted in linear scale at the spectral resolution $\Delta f=6\times10^{-7}$, the exact details of the cavity mode are resolved and characterized as its resonant frequency $f_0= 0.440194$ and Q value of $1.98\times10^4$ as labeled in the inset.

To characterize the influences of the finite supercell sizes prescribed by TMM, we also calculated the transmission spectra when increasing the supercell size from 3×3 unit cells

through 6×6 unit cells. Figure 3-3 shows high resolution ($\Delta f$=6×10$^{-7}$) spectra for the 4 different supercell sizes. The cavity mode properties (resonant frequency and Q value) extracted from the spectra (in Figure 3-3) are shown in Figure 3-4 (a). For supercell sizes larger than 4×4 unit cells, the cavity mode resonant frequency has already stabilized within an uncertainty range of ±0.1%. Also shown in Figure 3-4(a) is the Q value which stabilizes between 1×10$^4$ and 5×10$^4$ even quicker than the resonant frequency. Due to the periodic boundary condition used in TMM, the change of the super cell size is a change of the cavity layer's specific geometry. Figure 3-4 (a) shows that the Q value is not sensitive to the specific geometries of optical cavities embedded in 3D PCs. This result is in agreement with results reported in reference 6 and 21: the Q values of cavities with different sizes and shapes embedded in the same 3D PC structure do not change too much.

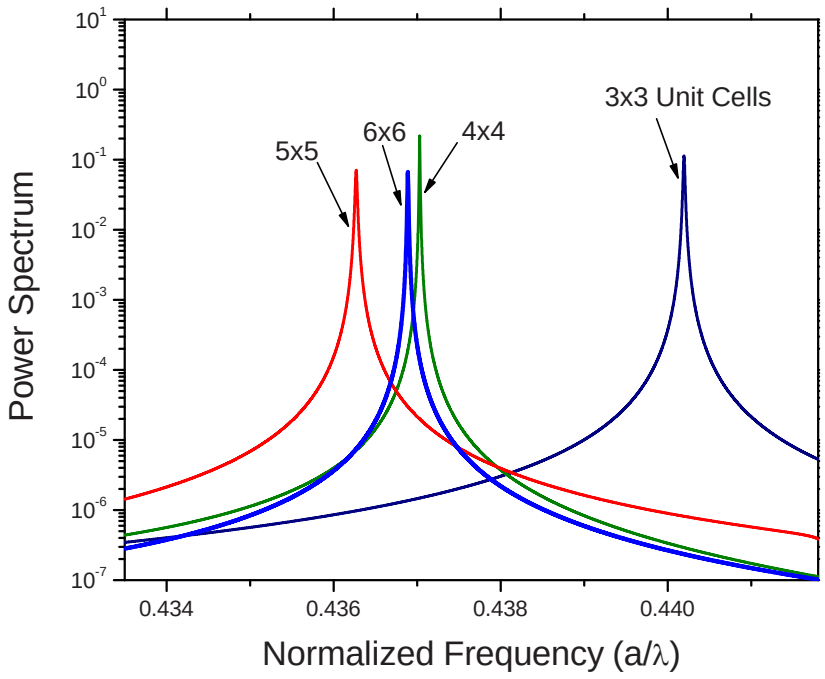


Figure 3-3: The spectra for varying supercell sizes

This is quite different from the usual behavior of 2D membrane PC cavities where radiation loss into the light cone plays a pivotal role in the cavity loss.[22,23] In 3D layer-by-layer PC cavities, the most significant factor determining the Q values is the number of cladding layers along the z-orientation.[6,21] Figure 3-4 (b) shows the Q value of cavity mode increase monotonically and almost exponentially as the number of cladding layers increasing along the z-orientation.

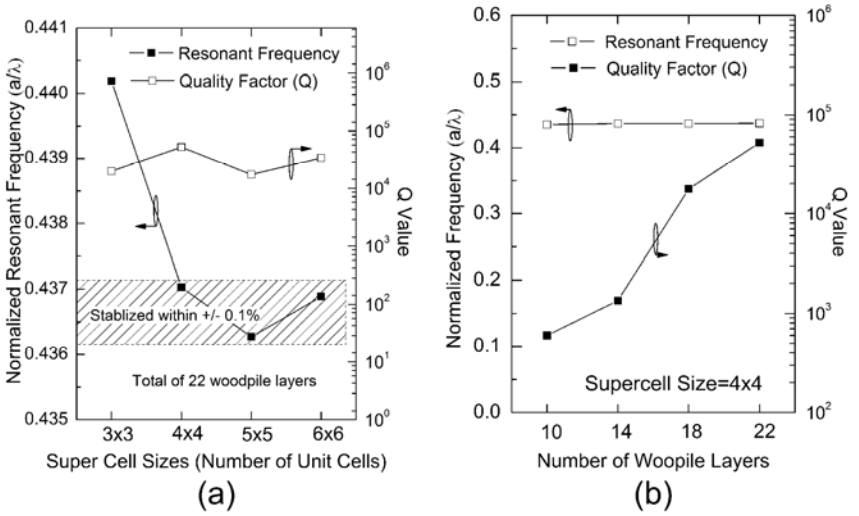


Figure 3-4: (a) Extracted from the spectra in Figure 3-3, the cavity resonant mode frequency and Q value vary and stabilize, as supercell size increases. (b) The cavity mode resonant frequency and Q value are plotted as functions of total number of layers along the z direction.

Our method uses relatively moderate computer resources. For instance, the whole high resolution spectrum through the 5-by-5 structure shown in Figure 3-3 can be obtained in less than three hours with a 24-CPU (Intel Xeon$^{TM}$ 3.0 GHz) computer cluster. The interpolation takes less than one second. Another advantage is that increasing the total number of layers along the z-direction does not increase the computation effort very much due to the repeating layer structure pattern. In conclusion, we have proposed and numerically demonstrated a highly efficient numerical modeling method for 3D PC cavity structures, based on a combination of TMM and rational function interpolation, which can be used at other 2D or 3D PC structures.

## 3.3 Origin of Lorentzian resonant peaks

Although it is well known that the resonant peaks of electromagnetic wave inside photonic crystal are Lorentzian form. It is not trivial from first sight; actually it is the property of general wave equations. When there is interference between continuous modes and localized modes, more complicate Fano peaks may be present.

Both Lorentzian peaks and Fano peaks can be interpolated through our rational function interpolation discussed in the first section of this chapter. In this section, detailed derivation of the origin of Lorentzian resonant peaks is discussed.

We start from general wave propagation case. The loss (i.e. lifetime, quality factor, Q) of a resonant mode can be understood as the summation of the coupling of this resonant mode to all radiation modes outside the cavity (Eq. (3.3)) where $n$ is summarizing over all radiation modes, which include the outward propagating waveguide modes, if waveguides are used in the vicinity of the cavity.

$$\frac{1}{Q_{tot}} = \sum_{n} \frac{1}{Q_n} \tag{3.3}$$

In a coupling Q experiment, the right hand side of Eq.(3.3) can be divided into two parts which are expressed at Eq. (3.4) where the first term stands for all of the injection channels (modes) being used in the coupling Q experiment, and the second term stands for all other radiation modes, where no injection are presented.

$$\frac{1}{Q_{tot}} = \sum_{n=1}^{c} \frac{1}{Q_n} + \sum_{n \neq 1 \sim c} \frac{1}{Q_n} \tag{3.4}$$

So, let's simplify the notations and rewritten as Eq. (3.5) where $Q_c$ and $Q_{rec}$ are injection channels coupling Q and the Q for rest of the radiation modes.

$$\frac{1}{Q_{tot}} = \sum_{n=1}^{c} \frac{1}{Q_n} + \sum_{n\neq 1\sim c} \frac{1}{Q_n} = \frac{1}{Q_c} + \frac{1}{Q_{rec}} \tag{3.5}$$

Therefore, according to the general definition of Q, without any injection, the energy in a cavity resonant mode decays with time (Eq. (3.6)) where $W(t)$ is the energy in the resonant mode, $\omega_0$ is the central frequency of the resonant mode itself with the combined effect of all coupling loss mechanisms.

$$W(t) = W(t)\big|_{t=0} \cdot e^{-\frac{\omega_0 t}{Q_{tot}}} \tag{3.6}$$

It can be proven that the power spectrum coupled into the cavity mode will be Eq.(3.7) which is a Lorentzian line with peak value expressed at Eq. (3.8) and FWHM expressed at Eq. (3.9).

$$S(\omega) = \frac{1}{Q_c \cdot Q_{res}} \cdot \frac{1}{\frac{1}{4}\cdot\left(\frac{1}{Q_c}+\frac{1}{Q_{res}}\right)^2 + \frac{(\omega-\omega_0)^2}{\omega_0^2}} \tag{3.7}$$

$$S_{\max} = S(\omega)\big|_{\omega=\omega_0} = \frac{4}{Q_c \cdot Q_{res}} \cdot \frac{1}{\left(\frac{1}{Q_c}+\frac{1}{Q_{res}}\right)^2} \tag{3.8}$$

$$\Delta\omega = \omega_0 \cdot \left(\frac{1}{Q_c} + \frac{1}{Q_{res}}\right) \equiv \frac{\omega_0}{Q_{tot}} \tag{3.9}$$

Now let's go back to prove Eq. (3.7) by starting from the general oscillation problem expressed at Eq. (3.10) where $S_+$ is the injection channels' amplitude. $|S_+|^2$ is the normalized power flow delivered by this supermode, for example in the unit of Watt. Then we use letter $a$ to represent the amplitude of the resonant mode we are coupling to. Or, it's the peak value on the resonant mode profile. And it's normalized that $|a|^2$ equals the total energy in the mode in the unit of Joule. Eq. (3.10) is a lossy oscillator ($1/\tau_{tot}$), driven by an external source

($\kappa \cdot S_+$) where $\kappa$ is the coupling strength between the injection channels and the resonant mode. When the driven term is turned on at frequency $\omega$ with the time dependence of $e^{j\omega t}$, the solution of equation Eq. (3.10) is found at Eq. (3.11)

$$\frac{da}{dt} = j\omega_0 a - \frac{1}{\tau_{tot}} \cdot a + \kappa \cdot S_+ \tag{3.10}$$

$$a = \frac{\kappa \cdot S_+}{j(\omega - \omega_0) + \frac{1}{\tau_{tot}}}$$
$$|\kappa| = \sqrt{\frac{2}{\tau_c}} \tag{3.11}$$

Then Eq. (3.10) can be simplified to Eq. (3.12) given the arbitrary constant phase difference between $S_+(t)$ and $a(t)$ can be fixed to make the constant $\kappa$ be a real number. Simultaneously, the phase constant for $S_-(t)$ is also fixed due to this choice. With the energy conservation relation (Eq. (3.13)) and Eq. (3.14), we can obtain Eq. (3.15).

$$\frac{da}{dt} = j\omega_0 a - \frac{1}{\tau_{tot}} \cdot a + \sqrt{\frac{2}{\tau_c}} \cdot S_+ \tag{3.12}$$

$$|S_+|^2 - |S_-|^2 = \frac{d|a|^2}{dt} + \frac{2}{\tau_{res}} \cdot |a|^2 \tag{3.13}$$

$$S_-(t) = \beta \cdot S_+(t) + \sqrt{\frac{2}{\tau_c}} \cdot a(t) \tag{3.14}$$

$$S_-(t) = -S_+(t) + \sqrt{\frac{2}{\tau_c}} \cdot a(t) \tag{3.15}$$

Finally with Eq. (3.11) and Eq. (3.15), the reflection coefficient of the resonator system can be written as Eq. (3.16) and the power spectrum coupled into the cavity system can be found as Eq. (3.17), i.e. we proved Eq. (3.7).

$$\frac{S_-}{S_+} = \frac{(1/\tau_c) - (1/\tau_{res}) - j(\omega - \omega_0)}{(1/\tau_c) + (1/\tau_{res}) + j(\omega - \omega_0)} \tag{3.16}$$

$$S(\omega) = 1 - \left|\frac{S_-}{S_+}\right|^2 = 1 - \left|\frac{(1/\tau_c) - (1/\tau_{res}) - j(\omega - \omega_0)}{(1/\tau_c) + (1/\tau_{res}) + j(\omega - \omega_0)}\right|^2$$
$$= \frac{1}{Q_c \cdot Q_{res}} \cdot \frac{1}{\frac{1}{4}\cdot\left(\frac{1}{Q_c} + \frac{1}{Q_{res}}\right)^2 + \frac{(\omega - \omega_0)^2}{\omega_0^2}} \qquad (3.17)$$

**References:**


1. J. C. Knight, T. A. Birks, P. St. J. Russel, and D. M. Atkin, "All-silica single-mode fiber with photonic crystal cladding," *Opt. Lett.* **21**, 1547 (1996)
2. A. Mekis, J.C. Chen, I. Kurland, S. Fan, P. R. Villeneuve, and J.D. Joannopoulous "High transmission through sharp bends in photonic crystal waveguides," *Phys. Rev. Lett.* **77**, 3787 (1996)
3. SY Lin, E Chow, V Hietala, PR Villeneuve, and JD Joannopoulos, "Experimental demonstration of guiding and bending of electromagnetic waves in a photonic crystal," *Science* **282**, 274 (1998)
4. A. Chutinan, and S. Noda, "Highly confined waveguides and waveguide bends in three-dimensional photonic crystal," *Appl. Phys. Lett.* **75**, 3739 (1999)
5. E. Özbay, G. Tuttle, M. Sigalas, C. M. Soukoulis, and K. M. Ho, "Defect structures in a layer-by-layer photonic band-gap crystal," *Phys. Rev. B* **51**, 13961 (1995)
6. M. Okano, A. Chutinan, and S. Noda, "Analysis and design of single-defect cavities in a three-dimensional photonic crystal," *Phys. Rev. B* **66**, 165211 (2002)
7. J. B. Pendry, "Photonic Band Structures," *J. Mod. Optic.* **41**, 209 (1994)
8. A. Taflove, and S. C. Hagness, *Computational Electrodynamics*, Artech House, MA, 2000
9. M. G. Moharam and T. K. Gaylord, "Rigorous coupled-wave analysis of planar-grating diffraction, " *J. Opt. Soc. Am* **71** 811 (1981)
10. L. L. Lin, Z. Y. Li and K. M. Ho, "Lattice symmetry applied in transfer-matrix methods for photonic crystals," *J. Appl. Phys.* **94**, 811 (2003)
11. W. H. Press, *Numerical Recipes*, Cambridge University Press, Cambridge, UK, 1992

12. J. Stoer and R. Bulirsch, *Introduction to Numerical Analysis*, Springer-Verlag, New York, 1980
13. E. Yablonovitch, "Inhibited Spontaneous Emission in Solid-State Physics and Electronics," *Phys. Rev. Lett.* **58**, 2059 (1987)
14. R. B. Adler, L. J. Chu, R. M. Fano, *Electromagnetic Energy Transmission and Radiation*, John Wiley & Sons, New York, 1960
15. H. A. Haus, *Waves and Fields in Optoelectronics*, Prentice-Hall, New Jersey, 1984
16. Ph. Lalanne, J.P. Hugonin, and J.M. Gerard, "Electromagnetic study of the quality factor of pillar microcavities in the small diameter limit", *Appl. Phys. Lett.* **84**, 4726, (2004)
17. K. M. Ho, C. T. Chan, C. M. Soukoulis, R. Biswas and M. Sigalas, "Photonic band gaps in three dimensions: new layer-by-layer periodic structures," *Solid State Commun.* **89**, 413 (1994)
18. Ming Li, J.R. Cao, X. Hu, M. Miyawaki, and K.M. Ho, "Fano Peaks in the Band Gap of 3D Layer-by-layer Photonic Crystal", to be published.
19. S. Fan, and J.D. Joannopoulos, "Analysis of Guided Resonances in Photonic Crystal Slabs", *Phys. Rev. B* **65**, 235112 (2002)
20. S. Dey and R. Mittra, "Efficient computation of resonant frequencies and quality factors of cavities via a combination of the Finite-Difference Time-Domain technique and the Pade approximation," *IEEE Microw. Guided W.* **8**, 415 (1998)
21. S. Ogawa, M. Imada, S. Yoshimoto, M. Okano, S. Noda, "Control of Light Emission by 3D Photonic Crystals, " *Science* **305**, 227 (2004)
22. O. Painter, K. Srinivasan, J. D. O'Brien, A. Scherer, and P. D. Dapkus, "Tailoring of the resonant mode properties of optical nanocavities in two-dimensional photonic crystal slab waveguides," *J. Opt. A-Pure Appl. Op.* **3**, S161 (2001)
23. K. Srinivasan and O. Painter, "Momentum space design of high-Q photonic crystal cavities," *Opt. Express* **10**, 670 (2002)

# Chapter 4. Higher-order planewave incidence

Photonic crystal itself is a structure with high symmetries due to its repeating pattern. The planewave input may also have certain symmetries. Then the solution of the Maxwell's Equations via the planewave based transfer (scattering) matrix method may have symmetry properties and it can lead to degeneracy phenomena. For example if we use the zero order plane wave incidence to excite photonic crystal cavity with certain symmetry, not all the resonant modes can be excited. In this chapter, we apply the general group theory to our method to study this problem and introduce the concept of higher-order incidence as a solution. One detailed example of the higher-order incidence is applied towards our classical layer-by-layer woodpile photonic crystal cavity array.

## 4.1 Planewave incidence

As discussed at the section 2.6.1 to get spectra from the calculated **S** matrix, we must use certain incidence wave as input. And this incidence wave is represented by a column vector $E_0$ of $N_p$ elements (Eq. (2.52)). The simplest and widely used incidence is the zero order planewave incidence with two polarizations – **s** polarization (or called **e** polarization) and **p** polarization (or called **h** polarization). The zero order **e** polarization is defined as $E^0_{00,x} = -1, E^0_{00,y} = 0$ and all other elements are zero at vector $E_0$ . The zero order **h** polarization is defined as $E^0_{00,x} = 0, E^0_{00,y} = 1$ and all other elements are zero at vector $E_0$.

Even with zero order incidence towards three dimensional photonic crystals, the relationship between the incident angles ($\theta, \varphi$), polarization angle ($\alpha$) and the physical position of photonic crystal is usually complex. To make those relations clear, we define the convention used in our method in this section.

First, the physical real space coordinate is defined at Figure 4-1; the rod of the layer-by-layer woodpile photonic crystal structure has its rods parallel to $X$ or $Y$ axis according to different layers. The origin point $O$ should be at the center of the first layer of the photonic crystal, but to illustrate more detail, I shift the photonic crystal to the first quadrant of $XY$ plane.) The $Z$ axis is the cladding layer (through origin $O$ and point out the paper in Figure 4-1). In the illustration figure the woodpile layer-by-layer photonic crystal structure has all its layers with $Z$ axis position larger than zero.

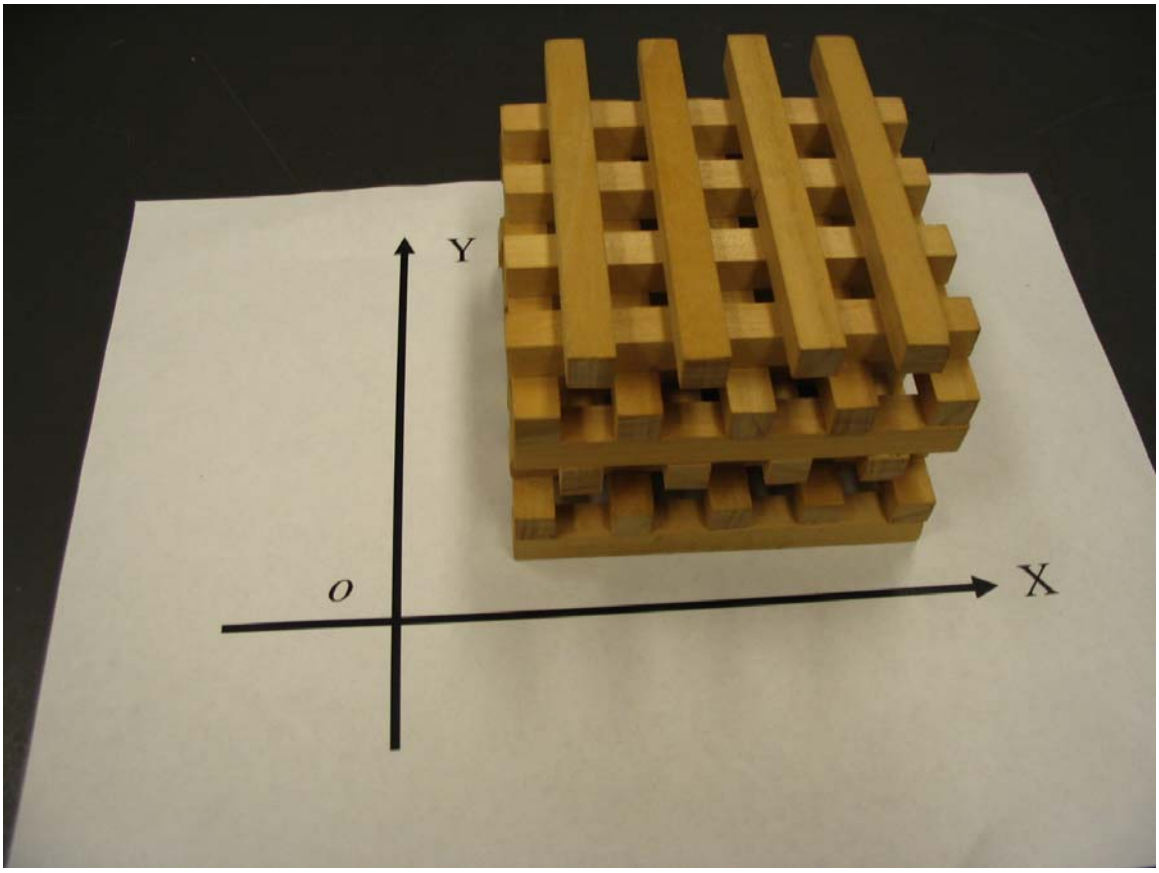


Figure 4-1: Coordinate system (Real object)

Second, define the incident angle based on the geometry coordinate ( $XYZ$ ) illustrated at Figure 4-1. We adopt the convention widely used at various physics systems: the azimuthal

angle $(\theta,\varphi)$ is defined in Figure 4-2. The wave vector $\boldsymbol{k}$ defines the incident direction. Line $\overline{Ok}$ projects on $XOY$ plane giving $\overline{OB}$.

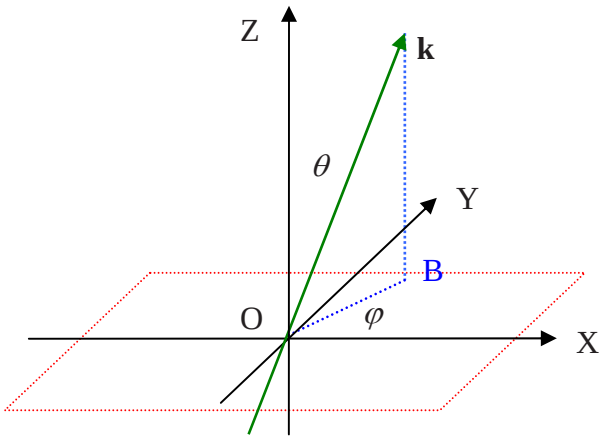


Figure 4-2: Coordinate system (XYZ axis)

Third, for each incident direction $\boldsymbol{k}$, there are two independent polarization directions for the electric field vector. To uniquely define the two independent polarization directions, we first define an incident plane. The incident plane is the plane which contains the vector $\boldsymbol{k}$ and axis $OZ$ which is the normal direction of the first photonic crystal layers (or the $XOY$ plane). In Figure 4-2, the incident plane is plane $ZOBk$. (Note: incident plane is always perpendicular to $XOY$.) Now, we can define the two independent polarization direction: $\boldsymbol{e_1}$ which is perpendicular to the incident plane and $\boldsymbol{e_2}$ which is in the incident plane and perpendicular to $\boldsymbol{e_1}$ and $\boldsymbol{k}$. In fact $\boldsymbol{e_1}$, $\boldsymbol{e_2}$ and $\boldsymbol{k}$ are orthogonal to each other and composes a right hand Cartesian coordinate. After we define the two independent polarization angles, we can define the polarization direction when the polarization angle equals to $\alpha$ where $\alpha$ is rotating counter-clockwise from the $\boldsymbol{e_1}$ axis (in Figure 4-3).

Note: the $\boldsymbol{k}$ direction points out of $\boldsymbol{e}_1 O' \boldsymbol{e}_2$ plane. We can use $\boldsymbol{e_1}$, $\boldsymbol{e_2}$ and $\alpha$ to express any polarizations via $\vec{e}_\alpha = (\cos\alpha)\vec{e}_1 + (\sin\alpha)\vec{e}_2$. The $\boldsymbol{h}$ polarization means its electrical field is parallel to $\boldsymbol{e_1}$. And, the $\boldsymbol{e}$ polarization means its electrical field is parallel to $\boldsymbol{e_2}$.

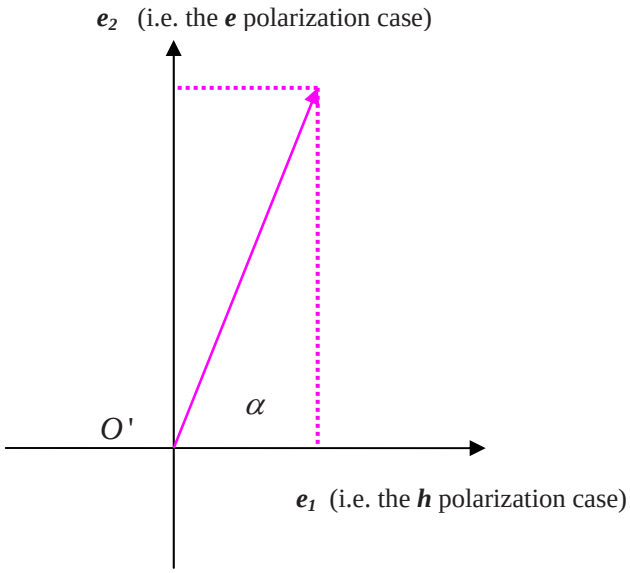


Figure 4-3: Polarization angle

Fourth, now we have defined the incident angle ($\theta, \varphi$) and polarization angle $\alpha$ and the relationship between them to the physical position of photonic crystal at real space coordinate ($XYZ$). Now we can express any incidence in term of the components at the $XYZ$ coordinate system. We can realize this by two steps; first find the three components of $e_1$ and $e_2$ by Eq. (4.1) and then apply $\vec{e}_\alpha = (\cos\alpha)\vec{e}_1 + (\sin\alpha)\vec{e}_2$. Finally we can get the $x, y, z$ components of arbitrary planewave incidence $\vec{e}_\alpha$ (Eq. (4.2)) at the $XYZ$ coordinate system.

$$\begin{aligned} \vec{e}_1 &= (-\sin\varphi)\hat{x} + (\cos\varphi)\hat{y} \\ \vec{e}_2 &= (-\cos\varphi\cdot\cos\theta)\hat{x} + (-\sin\phi\cdot\cos\theta)\hat{y} + (\sin\theta)\hat{z} \end{aligned} \tag{4.1}$$

$$\begin{aligned} e_{\alpha,x} &= -\sin\varphi\cdot\cos\alpha - \cos\varphi\cdot\cos\theta\cdot\sin\alpha \\ e_{\alpha,y} &= \cos\varphi\cdot\cos\alpha - \sin\phi\cdot\cos\theta\cdot\sin\alpha \\ e_{\alpha,z} &= \sin\theta\cdot\sin\alpha \end{aligned} \tag{4.2}$$

Now, to get a feeling or what is really looks like, here I also post some real pictures: the pencil represents the incident light, at the end of the pencil, we can see there are three arrows: the red arrow is $\boldsymbol{e}_1$, the red arrow with black head is $\boldsymbol{e}_2$ and the blue arrow is electric field direction for a certain polarization angle $\alpha$.

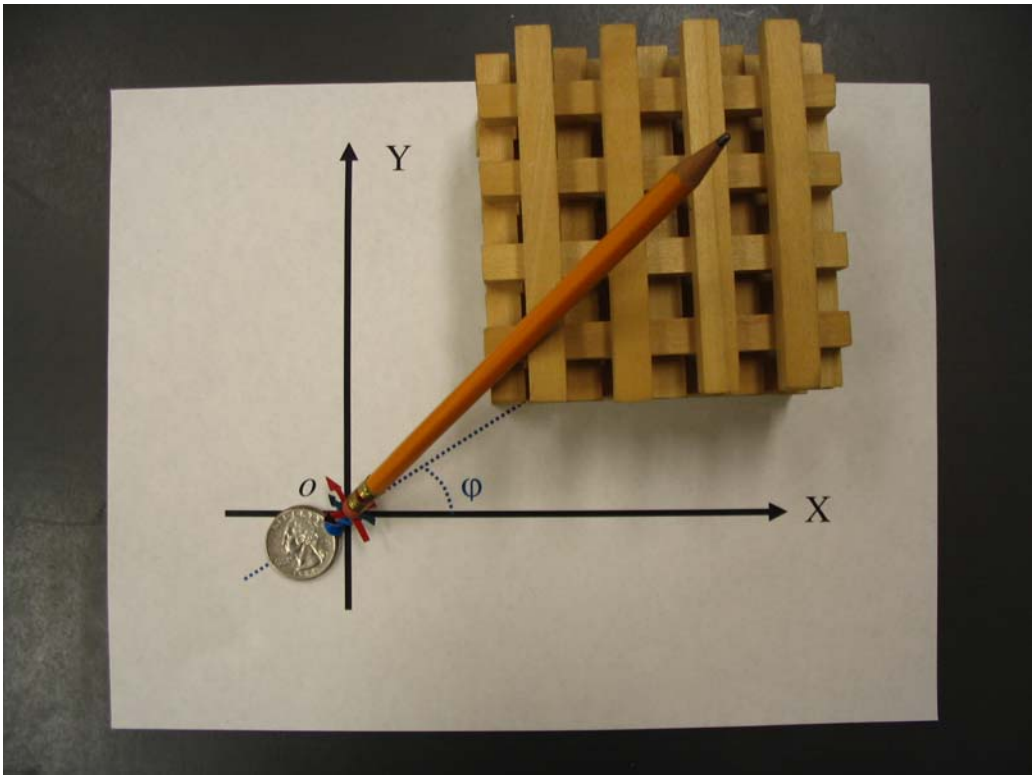


Figure 4-4: Incident angle (Real object)

Here is some special case of the incident angle: Figure 4-5 shows the normal incident case in which the origin $O$ and $O'$ are at the same position; Figure 4-6 shows a special case where $\theta = 0$.

For each pair of incident angle, there are two independent polarizations can be chosen according to the convention of 2D photonic crystal: TE or TM mode. But the definition of TE and TM is not clear for 3D or 1D photonic crystal, even for 2D photonic crystal, people usually have different conventions for different geometry cases. In our planewave based

transfer (scattering) matrix algorithm, the incident electric magnetic wave is defined by incidence angles $(\theta, \varphi)$ and polarization angle $(\alpha)$.

$$\theta = 0, \varphi = 0, \alpha$$

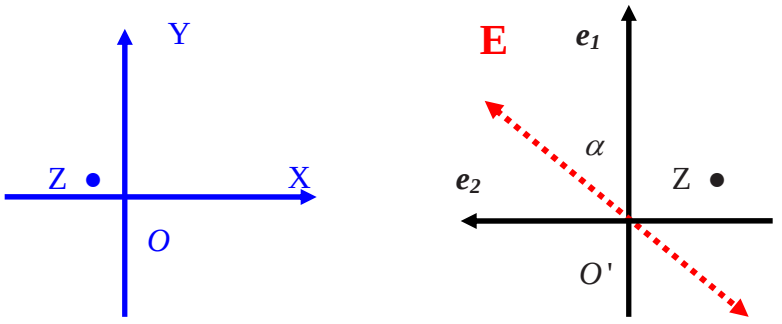


Photonic crystal plane: XOY  EM polarization plane $e_1$ and $e_2$

Figure 4-5: Special case, normal incident

$$\theta = 0, \varphi \neq 0, \alpha$$

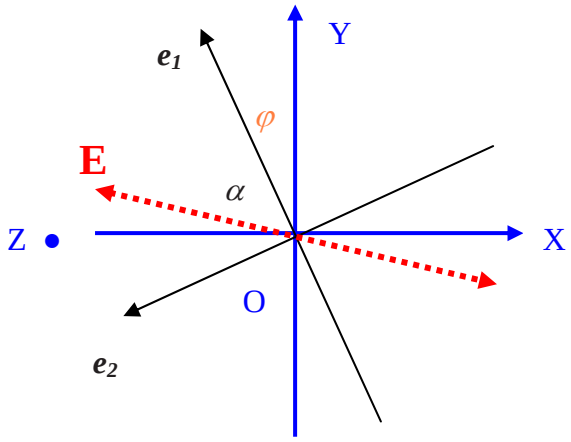


Figure 4-6: Special case, theta = 0

The normal incidence **e** and **h** polarization have very high symmetry, for example rotate 180 degree and $X$ axis mirror symmetry and $Y$ axis mirror symmetry which will lead to mode degeneracy and normal incidence calculation only will miss some modes. Although oblique incidence can break any geometry related symmetry and can excite all possible modes in the spectra, the interpolation results is bad due to the reason we are going to discuss in the next section. The way to keep the good interpolation result of normal incidence while extracting all possible modes is our recently introduced higher-order normal incidence.

Under some circumstances oblique incidence is prohibit (for example: the symmetric transfer matrix method which utilize the symmetry property of the geometry and input plane wave to reduce memory usage and calculation time dramatically), and higher-order normal incidence is the only choice to extract all possible resonant modes from the planewave based transfer (scattering) matrix algorithm.

## 4.2 Comparison between oblique incidence and fixed $k$ value incidence

As we mentioned in the last section, the spectra interpolation result from data points of oblique incidence is bad but the spectra interpolation result from data points of higher-order normal incidence is good. In this section, we explain why the oblique incidence interpolation is bad and introduce the theoretical foundation of fixed $k$ value incidence.

Let's take a typical point defect embedded in the photonic crystal for example. The planewave based transfer (scattering) matrix method adopts super cell configuration, i.e. the periodic boundary condition for both $X$ and $Y$ directions (Figure 4-7). The relationship between the super cell configuration and actual finite size photonic crystal with cavity embedded can be justified as: when the size of the super cell is large enough that the interaction across neighborhood cavity is negligible, then the result of the super cell approximates the result of the finite photonic crystal with cavity.

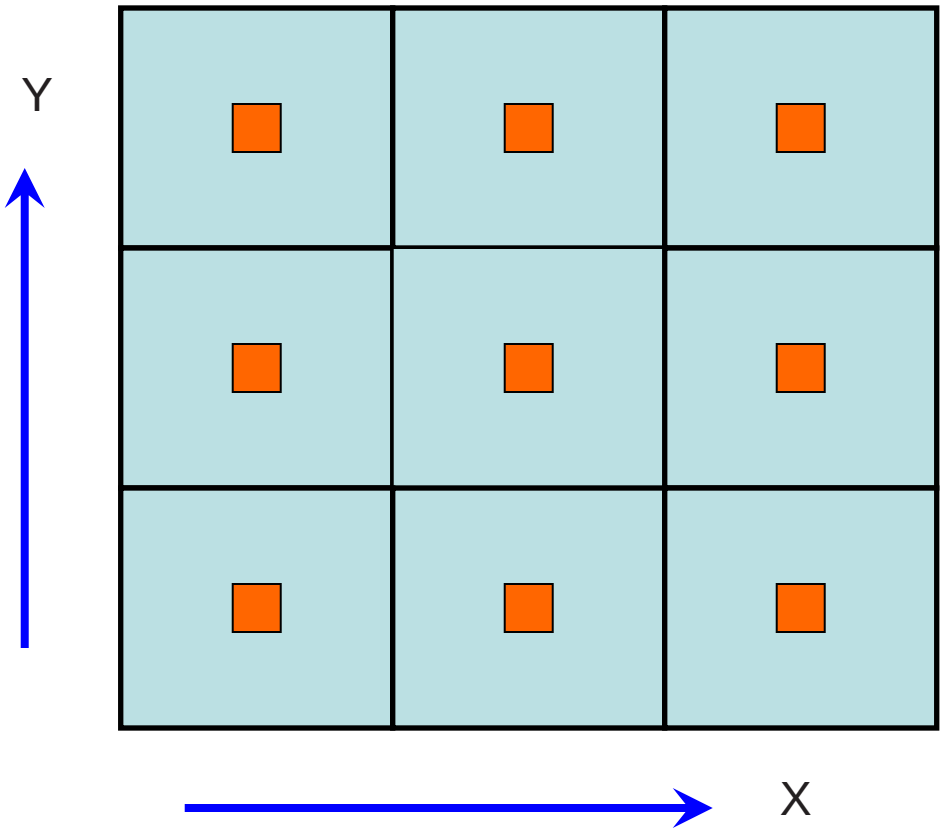


Figure 4-7: Illustration of the concept of super cell

The related extended Brillouin Zone of a super cell cavity embedded photonic crystal is conceptually illustrated at Figure 4-8 with the purple region representing the band gap and green line representing the defect mode.

Typically, the defect mode (cavity mode) resonant frequency is slight changed while the *k* value various. The frequency at Γ points is corresponding to the normal incident case. If a few normal incidence data points is used to interpolate the spectrum, we are going to get good interpolation results with the resonant frequency exactly as the frequency at Γ point which is confirmed by the detailed example at section 3.2. But as we mentioned at last section that modal degeneracy may happen due to the symmetry configuration while the

oblique incidence can extract all possible modes. However the oblique incidence has bad convergence on spectra interpolation.

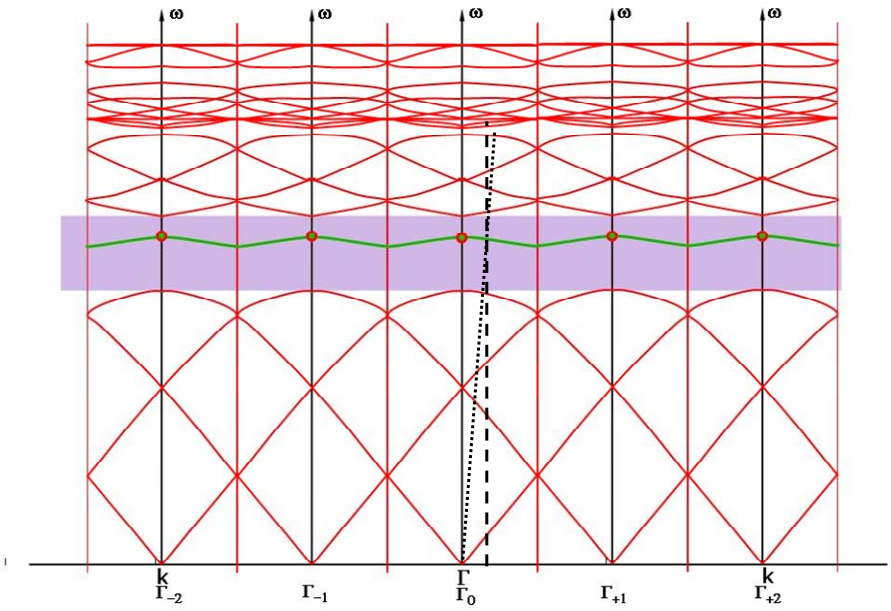


Figure 4-8: Extended Brillouin Zone for super cell configuration: the y axis is frequency and x axis is the k vales.

If we look close to the extended Brillouin Zone (Figure 4-8) with the dotted line represents an oblique incidence for fixed angle, then we can realize that for oblique incidence, the resonant frequency is not actually one fixed value but a small range of frequency. Trying to interpolate several data points belong to different resonant frequencies (although the difference is very small) into fixed peak Lorentzian curve is for sure not a good approach and the bad performance of oblique incidence is explained.

One way to preserve the good interpolation performance while breaking the symmetry related modal degeneracy is using the fixed non-zero $k$ value normal incidence. We still use the normal incidence (set the azimuthal angle $\theta$ to zero), but when we calculate the transfer matrix and scattering matrix we use the nonzero fixed $k$ value. The dashed line of Figure 4-8 is exactly this situation. In this case, the resonant frequency is one fixed value which is slight

different to the Γ points resonant value. Because the non-symmetric property of the non-zero fixed $k$, all possible resonant modes can be extracted while all data points belong to one fixed resonant peak so the interpolation works well. One directly application of the fixed $k$ value is to obtain a detailed variation of resonant frequency verses the $k$ value or the detailed dispersion relation for photonic crystal devices. One example of this application is discussed at section 4.4.

But how about if someone wants exactly all the Γ point resonant values while there is indeed model degeneracy? The answer is we can use higher-order incidence when the super cell configuration is used.

## 4.3 Higher-order incidence

Usually only the zero order planewave is propagation mode in vacuum and higher-order planewaves are evanescent mode below a frequency threshold (detailed explanation at later part of this section). But for higher-order planewave incidence, there exists propagation modes within the band gap frequency range which is the most interested frequency range to researchers. In this section, the concept of higher-order propagation planewave is discussed in very detail with symmetry consideration. We suppose the photonic crystal cavity has $X$ axis mirror symmetry and $Y$ axis mirror symmetry (i.e. belongs to $C_{2v}$ group); and we are going to apply higher-order normal incidence to break this symmetry while still take advantage of the normal incidence and symmetry properties of photonic crystal.

### 4.3.1 $C_{2v}$ Group

Typical symmetries involved in photonic crystal are $X$ mirror symmetry and/or $Y$ mirror symmetry. For structures with both $X$ and $Y$ mirror symmetry, they belong to $C_{2v}$ group. The most important property of $C_{2v}$ group is that there are 4 irreducible representations: $A_1$,

$A_2$, $B_1$ and $B_2$. And the electric field and magnetic field eigen mode should belong to one of the irreducible representations. There are 4 operations for $C_{2v}$ group: $\hat{E}, \hat{C}_2, \hat{\sigma}_x, \hat{\sigma}_y$ defined at Eq. (4.3).

$$\begin{aligned} \hat{E}(x,y,z) &= (x,y,z) \\ \hat{C}_2(x,y,z) &= (-x,-y,z) \\ \hat{\sigma}_x(x,y,z) &= (x,-y,z) \\ \hat{\sigma}_y(x,y,z) &= (-x,y,z) \end{aligned} \tag{4.3}$$

$$P = \frac{l}{h}\sum_R \chi_R \hat{P}_R \tag{4.4}$$

To determine which representation a function belongs, we need to apply the project operator (Eq. (4.4)) into that function for each representation. If the result is zero, then this function is not belonging to this representation, and if the result is nonzero, then this function is belonging to this representation. For any functions, it should belong to at least one of four representations. In Eq. (4.4), $h$ is the group size (i.e. how many operations, for $C_{2v}$ it is 4); $\chi$ is the number in the character table of the group; $\hat{P}_R$ is the operators and $l$ is the dimension of the group. The character table of $C_{2v}$ group is listed at Table 4-1.

Table 4-1: Character table of $C_{2v}$ group

| | $\hat{E}$ | $\hat{C}_2$ | $\hat{\sigma}_x$ | $\hat{\sigma}_y$ |
|---|---|---|---|---|
| $A_1$ | 1 | 1 | 1 | 1 |
| $A_2$ | 1 | 1 | -1 | -1 |
| $B_1$ | 1 | -1 | 1 | -1 |
| $B_2$ | 1 | -1 | -1 | 1 |

### 4.3.2 Higher-order planewave and its symmetry

The order of planewave is defined by the index $(i, j)$ in the column vector of incidence (Eq. (4.5) here $n_{cl}$ is the refractive index of cladding material). For any order, the **e** polarization (**e-pol.**) has $E_{ij,x} = -1, E_{ij,y} = 0$, and the **h** polarization (**h-pol.**) has $E_{ij,x} = 0, E_{ij,y} = 1$. The corresponding magnetic field components can be found through electric field components via Eq. (4.6).

$$\begin{aligned} E_x(x,y,z) &= \sum_{ij} E_{ij,x} e^{\mathbf{i}\left(k_{ij,x}x + k_{ij,y}y\right)} e^{\mathbf{i}\beta_{ij}z} \\ E_y(x,y,z) &= \sum_{ij} E_{ij,y} e^{\mathbf{i}\left(k_{ij,x}x + k_{ij,y}y\right)} e^{\mathbf{i}\beta_{ij}z} \\ with: \beta_{ij} &= \sqrt{k_0^2 - k_{ij,x}^2 - k_{ij,y}^2}; k_0 = n_{cl}\frac{\omega}{c} \end{aligned} \tag{4.5}$$

$$\begin{pmatrix} H_{ij,x} \\ H_{ij,y} \end{pmatrix} = \frac{1}{k_0 \beta_{ij}} \begin{pmatrix} -k_{ij,x}k_{ij,y} & k_{ij,x}^2 - \beta_{ij}^2 \\ -k_{ij,y}^2 + \beta_{ij}^2 & k_{ij,x}k_{ij,y} \end{pmatrix} \begin{pmatrix} E_{ij,x} \\ E_{ij,y} \end{pmatrix} \tag{4.6}$$

Now let's consider the zero order $(i = 0, j = 0)$ incidence, and consider air cladding, i.e. $n_{cl} = 1$. Then the electric field $X$ and $Y$ components for both **e-pol.** and **h-pol.** can be found through Eq. (4.5) and expressed in Eq. (4.7). And the corresponding magnetic field can be found through the magnetic components which can be calculated through Eq. (4.6), and the result is expressed at Eq. (4.8).

$$\begin{aligned} \mathbf{e-pol}: E_x^{00}(x,y,z) &= -e^{\mathbf{i}k_0 z}; E_y^{00}(x,y,z) = 0 \\ \mathbf{h-pol}: E_x^{00}(x,y,z) &= 0; E_y^{00}(x,y,z) = e^{\mathbf{i}k_0 z} \end{aligned} \tag{4.7}$$

$$\begin{aligned} \mathbf{e-pol}: H_x^{00}(x,y,z) &= 0; H_y^{00}(x,y,z) = -e^{\mathbf{i}k_0 z} \\ \mathbf{h-pol}: E_x^{00}(x,y,z) &= -e^{\mathbf{i}k_0 z}; E_y^{00}(x,y,z) = 0 \end{aligned} \tag{4.8}$$

$$E_z(x,y,z)=\frac{1}{ik_0\varepsilon_0}\left(\frac{\partial H_y}{\partial x}-\frac{\partial H_x}{\partial y}\right) \tag{4.9}$$

After obtaining the electric field $X$ and $Y$ components, the $Z$ components can be found by Eq. (4.9). For zero order normal incidence, the electric field $Z$ components turn out to be zero for both **e-pol.** and **h-pol.**. So the zero order normal incidence **e-pol.** $\mathbf{E}(\mathbf{r})=\hat{\mathbf{x}}\left(-e^{\mathbf{i}k_0 z}\right)$, there is only $X$ component; and the zero order normal incidence **h-pol.** $\mathbf{E}(\mathbf{r})=\hat{\mathbf{y}}\left(e^{\mathbf{i}k_0 z}\right)$, there is only $Y$ component.

Now let's analysis the $(i=1,j=0)$ order incidence with $k_{10,x}=2\pi/a_1, k_{10,y}=0$ (here $a_1$ is the lattice constant along the $Y$ direction of the super cell). According to Eq. (4.5), we have $\beta_{01}=\sqrt{k_0^2-k_{01,x}^2-k_{01,y}^2}=\sqrt{(\omega/c)^2-(2\pi/a_1)^2}$ and the corresponding $X$ and $Y$ electric field components of both **e-pol.** and **h-pol.** can be found through Eq. (4.5) and is expressed in Eq.(4.10).

The $X$ and $Y$ magnetic field components of both **e-pol.** and **h-pol.** is expressed in Eq. (4.11). The electric field $Z$ components can be found through Eq. (4.9) with the already known $X$ and $Y$ components of magnetic field (Eq. (4.11)). And it turns out to be Eq. (4.12) with $C_1, C_2$ and $C_3$ three nonezero constants.

$$\begin{aligned}
&\textbf{e - pol}: E_x^{10}(x,y,z)=-e^{\mathbf{i}\frac{2\pi}{a_1}x}e^{\mathbf{i}\beta_{01}z};\quad E_y^{10}(x,y,z)=0\\
&\textbf{h - pol}: E_x^{10}(x,y,z)=0;\quad E_y^{10}(x,y,z)=e^{\mathbf{i}\frac{2\pi}{a_1}x}e^{\mathbf{i}\beta_{01}z}
\end{aligned} \tag{4.10}$$

$$\begin{aligned}
&\textbf{e - pol}: H_x^{10}(x,y,z)=0;\quad H_y^{10}(x,y,z)=-C_1e^{\mathbf{i}\frac{2\pi}{a_1}x}e^{\mathbf{i}\beta_{01}z}\\
&\textbf{h - pol}: H_x^{10}(x,y,z)=C_2e^{\mathbf{i}\frac{2\pi}{a_1}x}e^{\mathbf{i}\beta_{01}z};\quad H_y^{10}(x,y,z)=0
\end{aligned} \tag{4.11}$$

$$\begin{aligned}
&\textbf{e - pol}: E_z^{10}(x,y,z) = C_3 e^{\mathbf{i}\frac{2\pi}{a_1}x} e^{\mathbf{i}\beta_{01}z} \\
&\textbf{h - pol}: E_z^{10}(x,y,z) = 0
\end{aligned} \qquad (4.12)$$

The similar procedure can be applied to all other orders; and the all three components of electric field can be found for each order. After we get the electric field for each order, we can apply the group theory analysis discussed at section 4.3.1 to find the symmetry properties of the electric field of each order.

Let's start with the simplest zero order $(i=0, j=0)$ incidence of **e-pol.**: $\mathbf{E}(\mathbf{r}) = \hat{\mathbf{x}}\left(-e^{\mathbf{i}k_0 z}\right)$. Apply the project operator (Eq. (4.4)) to $\mathbf{E}(\mathbf{r})$ to each of the four irreducible representations. If the result is zero then $\mathbf{E}(\mathbf{r})$ is not belonging to this representation and if the result is none zero, then $\mathbf{E}(\mathbf{r})$ is belonging to this representation. $\mathbf{E}(\mathbf{r})$ should belong to at least one of the representations. By the definition of the four symmetry operations at Eq. (4.3), we can get the symmetry transformed $\mathbf{E}(\mathbf{r})$ expressed at Eq. (4.13). To test whether $\mathbf{E}(\mathbf{r})$ belongs to $A_1$ irreducible representation, we need apply the projection operator to $\mathbf{E}(\mathbf{r})$ with the coefficient in the character table of $C_{2v}$ group's first line. Then we get $P^{(A1)} = 0$ which means $\mathbf{E}(\mathbf{r})$ does not belong to $A_1$ irreducible representation. The same procedure can be applied to $A_2$, $B_1$ and $B_2$ irreducible representations and result is put at Eq. (4.14). The conclusion is that the zero order **e-pol.** incidence belongs to $B_1$ representation.

$$\begin{aligned}
&\hat{E}\mathbf{E}(\mathbf{r}) = \hat{\mathbf{x}}\left(-e^{\mathbf{i}k_0 z}\right) \\
&\hat{C}_2\mathbf{E}(\mathbf{r}) = -\hat{\mathbf{x}}\left(-e^{\mathbf{i}k_0 z}\right) \\
&\hat{\sigma}_x\mathbf{E}(\mathbf{r}) = \hat{\mathbf{x}}\left(-e^{\mathbf{i}k_0 z}\right) \\
&\hat{\sigma}_y\mathbf{E}(\mathbf{r}) = -\hat{\mathbf{x}}\left(-e^{\mathbf{i}k_0 z}\right)
\end{aligned} \qquad (4.13)$$

The similar procedure can be applied the zero order incidence with **h-pol.**: $\mathbf{E}(\mathbf{r}) = \hat{\mathbf{y}}\left(e^{\mathbf{i}k_0 z}\right)$ with the four symmetry operation listed at Eq. (4.15) and the projection operation to each

irreducible representation at Eq. (4.16). And the result indicates that the zero order **h-pol.** incidence belongs to $B_2$ representation.

$$\begin{aligned}
P^{(A_1)}\mathbf{E}(\mathbf{r}) &= \frac{1}{4}\left(\hat{E}\mathbf{E}(\mathbf{r}) + \hat{C}_2\mathbf{E}(\mathbf{r}) + \hat{\sigma}_x\mathbf{E}(\mathbf{r}) + \hat{\sigma}_y\mathbf{E}(\mathbf{r})\right) = 0 \\
P^{(A_2)}\mathbf{E}(\mathbf{r}) &= \frac{1}{4}\left(\hat{E}\mathbf{E}(\mathbf{r}) + \hat{C}_2\mathbf{E}(\mathbf{r}) - \hat{\sigma}_x\mathbf{E}(\mathbf{r}) - \hat{\sigma}_y\mathbf{E}(\mathbf{r})\right) = 0 \\
P^{(B_1)}\mathbf{E}(\mathbf{r}) &= \frac{1}{4}\left(\hat{E}\mathbf{E}(\mathbf{r}) - \hat{C}_2\mathbf{E}(\mathbf{r}) + \hat{\sigma}_x\mathbf{E}(\mathbf{r}) - \hat{\sigma}_y\mathbf{E}(\mathbf{r})\right) \neq 0 \\
P^{(B_2)}\mathbf{E}(\mathbf{r}) &= \frac{1}{4}\left(\hat{E}\mathbf{E}(\mathbf{r}) - \hat{C}_2\mathbf{E}(\mathbf{r}) - \hat{\sigma}_x\mathbf{E}(\mathbf{r}) + \hat{\sigma}_y\mathbf{E}(\mathbf{r})\right) = 0
\end{aligned} \tag{4.14}$$

$$\begin{aligned}
\hat{E}\mathbf{E}(\mathbf{r}) &= \hat{\mathbf{y}}\left(e^{\mathbf{i}k_0 z}\right) \\
\hat{C}_2\mathbf{E}(\mathbf{r}) &= -\hat{\mathbf{y}}\left(e^{\mathbf{i}k_0 z}\right) \\
\hat{\sigma}_x\mathbf{E}(\mathbf{r}) &= -\hat{\mathbf{y}}\left(e^{\mathbf{i}k_0 z}\right) \\
\hat{\sigma}_y\mathbf{E}(\mathbf{r}) &= \hat{\mathbf{y}}\left(e^{\mathbf{i}k_0 z}\right)
\end{aligned} \tag{4.15}$$

$$\begin{aligned}
P^{(A_1)}\mathbf{E}(\mathbf{r}) &= \frac{1}{4}\left(\hat{E}\mathbf{E}(\mathbf{r}) + \hat{C}_2\mathbf{E}(\mathbf{r}) + \hat{\sigma}_x\mathbf{E}(\mathbf{r}) + \hat{\sigma}_y\mathbf{E}(\mathbf{r})\right) = 0 \\
P^{(A_2)}\mathbf{E}(\mathbf{r}) &= \frac{1}{4}\left(\hat{E}\mathbf{E}(\mathbf{r}) + \hat{C}_2\mathbf{E}(\mathbf{r}) - \hat{\sigma}_x\mathbf{E}(\mathbf{r}) - \hat{\sigma}_y\mathbf{E}(\mathbf{r})\right) = 0 \\
P^{(B_1)}\mathbf{E}(\mathbf{r}) &= \frac{1}{4}\left(\hat{E}\mathbf{E}(\mathbf{r}) - \hat{C}_2\mathbf{E}(\mathbf{r}) + \hat{\sigma}_x\mathbf{E}(\mathbf{r}) - \hat{\sigma}_y\mathbf{E}(\mathbf{r})\right) = 0 \\
P^{(B_2)}\mathbf{E}(\mathbf{r}) &= \frac{1}{4}\left(\hat{E}\mathbf{E}(\mathbf{r}) - \hat{C}_2\mathbf{E}(\mathbf{r}) - \hat{\sigma}_x\mathbf{E}(\mathbf{r}) + \hat{\sigma}_y\mathbf{E}(\mathbf{r})\right) \neq 0
\end{aligned} \tag{4.16}$$

Now we have the information of the zero order incidence of both polarizations: **e-pol.** belongs $B_1$ representation and **h-pol.** belongs to $B_2$ representation. The physics meaning of the above information is: the zero order **e-pol.** incidence can only excite resonant modes belong to $B_1$ representation and any other possible modes of $A_1$, $A_2$ or $B_2$ can not be excited by the zero order **e-pol.** incidence (or in other words, there will be no such resonant mode in the spectrum of zero order **e-pol.** incidence); the zero order **h-pol.** incidence can only excite resonant modes belong to $B_2$ representation and any other possible modes of $A_1$, $A_2$ or $B_1$

can not be excited by the zero order **h-pol.** incidence (or in other words, there will be no such resonant mode in the spectrum of zero order **h-pol.** incidence).

In actual photonic crystal cavity, the resonant modes may belong to any of the 4 irreducible representations, so we need analysis higher-order incidence to make sure all of four irreducible representations are covered.

Now let's do the similar analysis to the $i=1, j=0$ higher-order incidence with the electric field expressed in Eq. (4.17). By applying the 4 symmetry transformation operation $\hat{E}$, $\hat{C}_2$, $\hat{\sigma}_x$ and $\hat{\sigma}_y$ and using the projection operator, we can get the results that **e-pol.** belongs to $A_1$ and $B_1$ irreducible representations (Eq. (4.18)) and **h-pol.** belongs to $A_2$ and $B_2$ irreducible representations (Eq. (4.19)).

So higher-order $(i=1, j=0)$ incidence with **e-pol.** and **h-pol.** can cover all four representations and all possible resonant modes can be excited if both **h-pol.** and **h-pol.** of $(i=1, j=0)$ order incidence are used.

$$\begin{aligned}
&\textbf{e - pol}: \mathbf{E}(\mathbf{r}) = -e^{\mathbf{i}\frac{2\pi}{a_1}x} e^{\mathbf{i}\beta_{01}z}\hat{\mathbf{x}} - C_1 e^{\mathbf{i}\frac{2\pi}{a_1}x} e^{\mathbf{i}\beta_{01}z}\hat{\mathbf{z}} \\
&\textbf{h - pol}: \mathbf{E}(\mathbf{r}) = e^{\mathbf{i}\frac{2\pi}{a_1}x} e^{\mathbf{i}\beta_{01}z}\hat{\mathbf{y}}
\end{aligned} \tag{4.17}$$

**e - pol.**

$$\begin{aligned}
P^{(A_1)}\mathbf{E}(\mathbf{r}) &= \frac{1}{4}\left(\hat{E}\mathbf{E}(\mathbf{r}) + \hat{C}_2\mathbf{E}(\mathbf{r}) + \hat{\sigma}_x\mathbf{E}(\mathbf{r}) + \hat{\sigma}_y\mathbf{E}(\mathbf{r})\right) \neq 0 \\
P^{(A_2)}\mathbf{E}(\mathbf{r}) &= \frac{1}{4}\left(\hat{E}\mathbf{E}(\mathbf{r}) + \hat{C}_2\mathbf{E}(\mathbf{r}) - \hat{\sigma}_x\mathbf{E}(\mathbf{r}) - \hat{\sigma}_y\mathbf{E}(\mathbf{r})\right) = 0 \\
P^{(B_1)}\mathbf{E}(\mathbf{r}) &= \frac{1}{4}\left(\hat{E}\mathbf{E}(\mathbf{r}) - \hat{C}_2\mathbf{E}(\mathbf{r}) + \hat{\sigma}_x\mathbf{E}(\mathbf{r}) - \hat{\sigma}_y\mathbf{E}(\mathbf{r})\right) \neq 0 \\
P^{(B_2)}\mathbf{E}(\mathbf{r}) &= \frac{1}{4}\left(\hat{E}\mathbf{E}(\mathbf{r}) - \hat{C}_2\mathbf{E}(\mathbf{r}) - \hat{\sigma}_x\mathbf{E}(\mathbf{r}) + \hat{\sigma}_y\mathbf{E}(\mathbf{r})\right) = 0
\end{aligned} \tag{4.18}$$

**h - pol.**

$$
\begin{aligned}
P^{(A_1)}\mathbf{E}(\mathbf{r}) &= \frac{1}{4}\left(\hat{E}\mathbf{E}(\mathbf{r}) + \hat{C}_2\mathbf{E}(\mathbf{r}) + \hat{\sigma}_x\mathbf{E}(\mathbf{r}) + \hat{\sigma}_y\mathbf{E}(\mathbf{r})\right) = 0 \\
P^{(A_2)}\mathbf{E}(\mathbf{r}) &= \frac{1}{4}\left(\hat{E}\mathbf{E}(\mathbf{r}) + \hat{C}_2\mathbf{E}(\mathbf{r}) - \hat{\sigma}_x\mathbf{E}(\mathbf{r}) - \hat{\sigma}_y\mathbf{E}(\mathbf{r})\right) \neq 0 \\
P^{(B_1)}\mathbf{E}(\mathbf{r}) &= \frac{1}{4}\left(\hat{E}\mathbf{E}(\mathbf{r}) - \hat{C}_2\mathbf{E}(\mathbf{r}) + \hat{\sigma}_x\mathbf{E}(\mathbf{r}) - \hat{\sigma}_y\mathbf{E}(\mathbf{r})\right) = 0 \\
P^{(B_2)}\mathbf{E}(\mathbf{r}) &= \frac{1}{4}\left(\hat{E}\mathbf{E}(\mathbf{r}) - \hat{C}_2\mathbf{E}(\mathbf{r}) - \hat{\sigma}_x\mathbf{E}(\mathbf{r}) + \hat{\sigma}_y\mathbf{E}(\mathbf{r})\right) \neq 0
\end{aligned}
\tag{4.19}
$$

Further analysis shows that higher-order incidence $(i=-1, j=0)$ has the same results as higher-order incidence $(i=1, j=0)$. Similarly, the higher-order incidence $(i=0, j=\pm 1)$ covers $A_2$ and $B_1$ irreducible representations for **e-pol.** and $A_1$ and $B_2$ irreducible representations for **h-pol.** Each polarizations of any higher-order with $(i\geq 1, j\geq 1)$ can cover all four irreducible representations. Those results are summarized at Table 4-2 with $i\geq 1$.

Table 4-2: Irreducible repressions coved by high order incidence

| | $(0,0)$ | | $(0,\pm i)$ | | $(\pm i,0)$ | | $(\pm i,\pm i)$ | |
|---|---|---|---|---|---|---|---|---|
| | **e** | **h** | **e** | **h** | **e** | **h** | **e** | **h** |
| Rep. | $B_1$ | $B_2$ | $A_2$ $B_1$ | $A_1$ $B_2$ | $A_1$ $B_1$ | $A_2$ $B_2$ | all 4 | all 4 |

### 4.3.3 Possible propagation modes for higher-order incidence

As we mentioned at the beginning of this section, not all the higher-order planewave are propagation mode for all frequency ranges. We need pay close attention to the wave vector $k_z$ expressed in Eq. (4.20). When $k_z$ is real number, it is propagation mode; and when $k_z$ is imaginary number, it is evanescent mode which will decay exponentially with respect to the propagating distance. The resonant cavity modes can only be excited by propagation modes.

$$
k_z = \beta_{ij} = \sqrt{k_0^2 - k_{ij,x}^2 - k_{ij,y}^2}; k_0 = n_{cl}\frac{\omega}{c} \tag{4.20}
$$

For zero order incidence $(i=0, j=0)$ $k_{ij,x}=k_{ij,y}=0$, $k_z=k_0$ and it is real number for any frequency. So zero order incidence is propagating mode for all frequency range. Now let's take $(i=0, j=1)$ order incidence for example: $k_{ij,x}=0, k_{ij,y}=2\pi/a_2$ and $k_z$ is real number only for $n_{cl}\omega/c \geq 2\pi/a_2$ or $\omega \geq 2\pi c/(n_{cl}a_2)$. There is a cut-off frequency for propagation modes. Below that cut-off frequency, it is evanescent wave and can not be used to excite resonant cavity modes. Luckily, the frequency range we are interested in (within the band gap range) is usually above this cut-off frequency.

Based on our experience, the first band gap lower frequency edge is usually above 0.2 normalized frequency. If we set the normalized cut-off frequency to be 0.2, then the cut-off frequency $\omega$ takes the larger value of $\omega$ in $\omega A_1/2\pi c \geq 0.2$ and $\omega A_2/2\pi c \geq 0.2$. Here $A_1$ and $A_2$ is the lattice constant of the super cell, while $a_1$ and $a_2$ are the length of the unit cell along $X$ and $Y$ direction. Usually we have $A_1=ma_1$ and $A_2=ma_2$ with $m$ and $n$ integers (for example: $m=5, n=5$; we call it 5x5 super cell).

Now let's setup a lower frequency boundary ($c_0$ in Eq. (4.21)) and suppose all calculation is above this boundary. Based on this lower frequency boundary, we can find which higher order incidence are propagation modes and which order are evanescent modes.

$$c_0=\frac{\omega a_1}{2\pi c}, \quad \frac{\omega}{c}=c_0\frac{2\pi}{a_1} \tag{4.21}$$

$$k_{ij,x}=i\frac{2\pi}{ma_1}; \quad k_{ij,y}=j\frac{2\pi}{na_2} \tag{4.22}$$

For order $(i, j)$ incidence with $m\times n$ super cell configuration, $k_{ij,x}$ and $k_{ij,y}$ can be expressed in Eq. (4.22). With our pre-set lower frequency boundary $c_0$, the order $(i, j)$ incidence is propagation mode only if the relation of Eq.(4.23) is satisfied. For fixed $m, n$ and $a_1, a_2$, the maximized order propagation incidence can be determined.

$$\left(n_{cl}\frac{\omega}{c}\right)^2 \geq k_{ij,x}^2 + k_{ij,y}^2 \quad or$$
$$\left(n_{cl}\frac{2\pi c_0}{a_1}\right)^2 \geq \left(i\frac{2\pi}{ma_1}\right)^2 + \left(j\frac{2\pi}{na_2}\right)^2 \qquad (4.23)$$
$$or \quad n_{cl}c_0 \geq \sqrt{\frac{i^2}{m^2} + \frac{j^2}{n^2\left(a_2/a_1\right)^2}}$$

If we draw all the higher-order $(i, j)$ into a diagram with $k_x$ and $k_y$ as the $X$ and $Y$ axis and keep $a_1 = a_2$ and $m = n$, they are isolated points of square grid. All the grid points within the circle with center at origin and radius of $mn_{cl}c_0$ are propagation modes, which is illustrated at Figure 4-9: Propagation modes in k space.

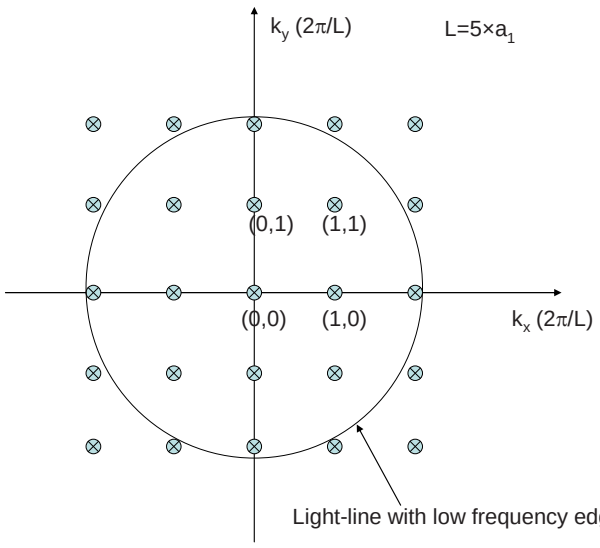


Figure 4-9: Propagation modes in k space

All the above discussion is based on normal higher-order incidence with fixed incidence wave vector $k_{0x} = k_{oy} = 0$, i.e. the $\Gamma_0$ point at Figure 4-8. In case of other fixed incidence wave vector $k_{0x}, k_{oy}$, the propagation mode is still with in the circle with radius $mn_{cl}c_0$, but the center of the circle is now $(k_{0x}, k_{oy})$.

## 4.4 Example of application of higher-order incidence

This section is modified from a paper published at *Optics Letters* Vol. 31, No. 23 (page 3498) at December 2006 with title: "Higher-order incidence transfer matrix method used in three-dimensional photonic crystal coupled-resonator array simulation", by M. Li, X. Hu, Z. Ye, K. Ho, J. Cao, and M. Miyawaki.

Photonic crystals (PCs), periodic dielectric media, can inhibit electromagnetic (EM) wave propagation in certain frequency ranges called photonic band gaps (PBGs).[1,2] Introducing point or line defects into PCs can create highly localized defect modes within the PBGs,[3] resulting in resonant cavities of high quality factor Q and low loss waveguides.[4,5,6] Recently, coupled PC cavity arrays have received much attention due to their potential application in integrated optical circuits.[7,8,9,10] However, most of these structures are based on two-dimensional (2D) PCs or 2D PC slab. There exist few studies[8] on resonant cavity arrays in three-dimensional (3D) PCs due to difficulties in fabrications and numerical simulations. In this letter, we theoretically study periodic resonant arrays in 3D PCs by using the planewave based transfer-matrix methods (TMM)[11,12] with higher-order planewave incidence and rational-function interpolation[13] techniques. As an example, both the quality factor and dispersion relation are obtained very efficiently for a resonant cavity array based on the layer-by-layer woodpile PCs. An interesting ultra-slow negative group velocity is observed in this structure. To our knowledge, this is the first time that dispersions are calculated for coupled resonant cavity arrays in 3D woodpile PCs in all directions.

The 3D layer-by-layer woodpile[14] PC is composed of 25 layers (in the z direction) of square dielectric rods of refractive index $n = 2.4$ and width $0.35a_0$, with the cladding material at both ends along z direction of refractive index $n_{cl}$. Here the lattice constant $a_0$ is the distance between two neighbored rods (shown in Figure 4-10(a)). The cavities are located in the 13th

layer and of double periodicities of $5a_0$ in both x and y directions. Each cavity is created by filling a volume of $a_0$ by $a_0$ by $0.35a_0$ with the rod material ($n = 2.4$) (shown in Figure 4-10 (b)).

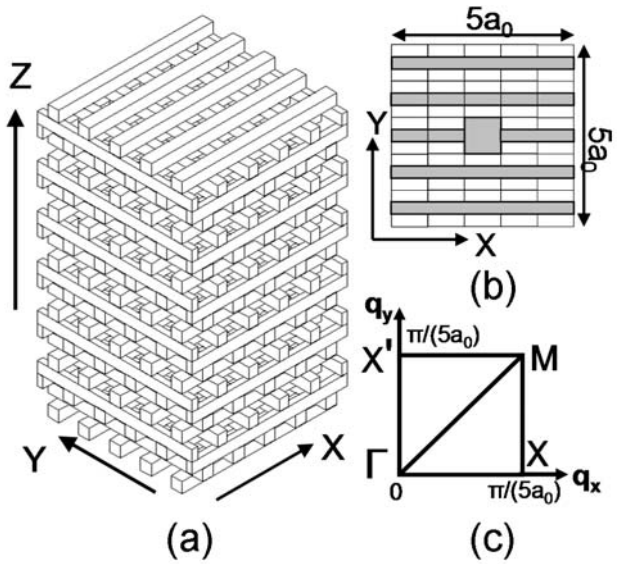


Figure 4-10: The X-Y-plane-periodic array of 3D woodpile PC (with cavity in the 13th layer): (a) the 5-by-5 super cell of total 25 layers along z direction with dielectric cladding of refractive index $n_{cl}$ (the cladding is not shown); (b) top view of the 13th layer with the cavity of volume of $a_0$ by $a_0$ by $0.35a_0$ and $n$ = 2.4; and (c) the irreducible Brillouin zone of ($q_x$, $q_y$). The 3D woodpile PC is composed of dielectric square rods of $n$ = 2.4 and width $0.35a_0$, where $a_0$ is the distance between two neighbored rods (i.e. the lattice constant).

The related reciprocal lattice $\left(G_x = 2i\pi/(5a_0), G_y = 2j\pi/(5a_0)\right)$ and irreducible Brillouin zone of the Bloch wave-vector $(q_x, q_y)$ for this periodic cavity array are shown in Figure 4-10(b) and Figure 4-10 (c), respectively. Since the resonant cavity array has x-axis and y-axis mirror symmetry, the cavity modes belong to the $\mathbf{C_{2v}}$ group with four irreducible representations ($\mathbf{A_1}$, $\mathbf{A_2}$, $\mathbf{B_1}$, **and** $\mathbf{B_2}$) and the character table of the $\mathbf{C_{2v}}$ group is listed in Figure 4-10 (c).[15]

We consider the incidence of planewaves with wave-vector $\left(k_x = q_x + G_x, k_y = q_y + G_y, k_z = (k_0^2 - k_x^2 - k_y^2)^{1/2}\right)$ upon the above resonant cavity array, where

$k_0 = n_{cl}\omega/c$ with $c$ the speed of light and $n_{cl}$ the cladding substrate refractive index. $k_x^2 + k_y^2 < k_0^2$ and $k_x^2 + k_y^2 > k_0^2$ corresponds to propagating and evanescent waves, respectively (shown in Figure 4-11 (a) and (b)). In our TMM algorithm,[11,10] the Bloch boundary condition with $(q_x, q_y)$ is used for a $5\times5$ supercell.

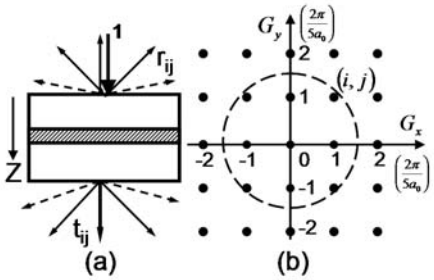


| $C_{2v}$ | E | $C_2$ | $\sigma_x$ | $\sigma_y$ |
|---|---|---|---|---|
| $A_1$ | 1 | 1 | 1 | 1 |
| $A_2$ | 1 | 1 | -1 | -1 |
| $B_1$ | 1 | -1 | 1 | -1 |
| $B_2$ | 1 | -1 | -1 | 1 |

(c)

| | e-pol. | h-pol. |
|---|---|---|
| (0,0) | $B_1$ | $B_2$ |
| (0,1) | $A_2B_1$ | $A_1B_2$ |
| (1,0) | $A_1B_1$ | $A_2B_2$ |
| (1,1) | $A_1A_2B_1B_2$ | $A_1A_2B_1B_2$ |

(d)

Figure 4-11: (a) Incidence of a planewave with wave-vector ( $k_x = q_x + G_x$ , $k_y = q_y + G_y$ and $k_z = \left(k_0^2 - k_x^2 - k_y^2\right)^{1/2}$ ) upon the 3D PC cavity array (periodic in the X-Y plane); solid (dashed) arrows stand for the propagating (evanescent) waves. (b) The reciprocal lattice for the 5-by-5 super cell PC cavity array; the G points inside (outside) the dashed circle (with radius $k_0 = n_{cl}\omega/c$ and center ($-q_x$, $-q_y$), shown for $\omega a/(2\pi c) = 0.43$ , $n_{cl} = 1.0$ and $q_x = q_y = 0$ ) stand for the propagating (evanescent) waves. (c) The $C_{2v}$ group character table for the PC cavity array with E, $C_2$, $\bullet_x$ and $\bullet_y$ symmetry operation.[15] (d) The irreducible representations for the **e**- and **h**- polarized incident planewaves of order ($i$, $j$), i.e. $G_x = 2i\pi/(5a_0)$ and $G_y = 2j\pi/(5a_0)$.

The electric field coefficient vector $(E_{ij,x}, E_{ij,y})$ of planewaves with $G_x = 2i\pi/(5a_0), G_y = 2j\pi/(5a_0)$ (named as order ($i$, $j$) in the following) can be transferred from layer to layer in the $z$ direction by a transfer matrix. Here $i, j = -N, ...0, 1, ...N$ and a favorable convergence is found using $N = 25$ for the present $5\times5$ supercell. Previously[13], normal incidence with $k_x = k_y = 0$ (i.e. order $(0,0)$ with $q_x = q_y = 0$) was used to study the PC cavities. However, not all the cavity modes could be excited with $(0,0)$ incidence with $q_x = q_y = 0$ (as shown in Figure 4-12) because of group symmetry considerations. To excite

all the cavity modes of PC cavities, we performed higher-order $(i, j)$ planewave incidences with both **e**- and **h**- polarizations defined by $E^0_{ij,x} = -1, E^0_{ij,y} = 0$ and $E^0_{ij,x} = 0, E^0_{ij,y} = 1$ respectively, where the superscript index $^0$ represents the electric field components before entering the photonic crystal structure.

The incidence of planewaves with $q_x = q_y = 0$ is firstly considered. The irreducible representations that the order $(i, j)$ could cover can be found through the projection operation,[15] and the results are shown in Figure 4-11 (d). Clearly, if the zero order $(i = j = 0)$ (i.e. normal incidence) is used alone, only the $\mathbf{B_1}$ or $\mathbf{B_2}$ representation is excited (for **e**- and **h**- polarizations, respectively) and any resonant modes belonging to $\mathbf{A_1}$ or $\mathbf{A_2}$ representation will not be excited. Actually for this particular photonic crystal cavity array structure there is indeed one resonant mode (mode A) belongs to $\mathbf{A_2}$ representation at normalized frequency 0.43948; and the other resonant mode (mode B) belongs to $\mathbf{B_1}$ representation at normalized frequency 0.44763. The mode shape profiles for both modes are also calculated by TMM with higher-order incidence and are illustrated in Figure 4-13 (a). Based on the projection operation[15], any higher order $(i, j)$ incidence with $i \geq 1$ and $j \geq 1$ will cover all the representations and both resonant modes can be excited.

To find the frequency and quality factor of the resonant modes, the nearly continuous transmission spectra are obtained accurately from the rational function interpolation of 21 individual frequencies ranging in the first band gap[13]. Figure 3 shows the transmission results for the planewave incidence of the first four orders. Although the transmission amplitude for different orders and polarizations varies dramatically, the resonant frequency and Q value for each resonant mode are practical identical: $f_A = 0.43948$, $Q_A = 11910$ and $f_B = 0.44763$, $Q_B = 6900$ (the relative difference of $f$ and $Q$ for different incidences is less than $10^{-5}$ and $10^{-4}$, respectively). The excited resonant peaks for each order $(i, j)$ incidence agree well with the above group theory analysis. For example, the group theory analysis indicates that the $(1, 0)$ order incidence with **e**-polarization covers the irreducible representations of $\mathbf{A_1}$ and

**$B_1$**, and hence the mode B (belonging to **$B_1$**) instead of mode A (belonging to **$A_2$**) appears in the calculated transmission spectrum for the $(1,0)$ incidence. There is also a third resonant mode found by TMM at normalized frequency $\omega a/(2\pi c) = 0.4635$.

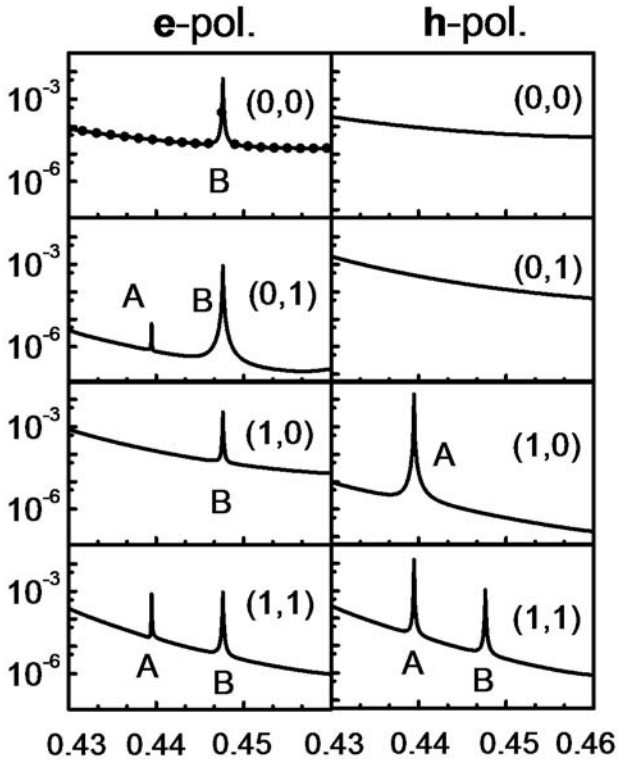


Figure 4-12: Transmission spectra for the planewaves incidence of $q_x = q_y = 0$ and order (*i*, *j*) upon the 3D PC cavity array with **e-pol** and **h-pol** defined by $E^0_{ij,x} = -1, E^0_{ij,y} = 0$ and $E^0_{ij,x} = 0, E^0_{ij,y} = 1$ respectively. The resonant mode A and B are also labeled. The first band gap in the z direction (i.e. the (0, 0) incidence) opens from $\omega a/(2\pi c) = 0.395$ to $\omega a/(2\pi c) = 0.515$. There is the third resonant mode at normalized frequency $\omega a/(2\pi c) = 0.4635$ which is not shown in this figure.

The transmission spectra are calculated for planewave incidence with different $(q_x, q_y)$. We note that all the cavity modes can be excited for the case of $(q_x \neq 0, q_y \neq 0)$ due to the broken symmetry of non-zero $q_x$ and $q_y$. The frequencies of resonant cavity modes can be extracted from the spectra and the related dispersion relations are illustrated at Figure 4-13 (b). The

slopes of the dispersions are very flat, indicating ultra-slow group velocities in the woodpile PC cavity array structure.

The average group velocity (calculated by finding the slope of the straight line connecting two high symmetry points) of mode A in the Γ-X(X') direction is $\upsilon_g = 0.0012c = 3.6\times10^5 m/s$ ($\upsilon_g = 0.0048c = 1.4\times10^6 m/s$) and that of mode B in the Γ-X' direction is $\upsilon_g = 0.0056c = 1.7\times10^6 m/s$. It is interesting that a negative group velocity of $\upsilon_g = -0.0009c = -2.7\times10^5 m/s$ can be achieved for mode B in the Γ-X direction.

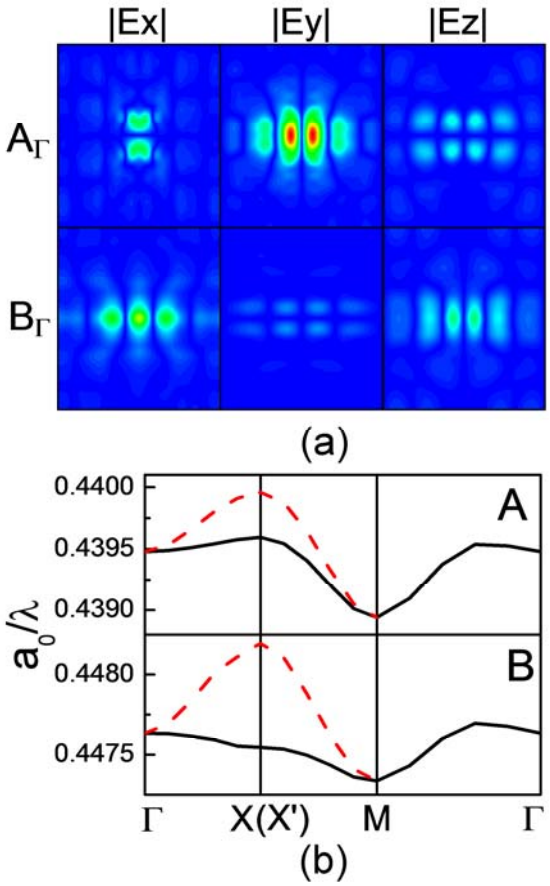


Figure 4-13:(a) Electric field mode profiles for the cavity modes A and B at • point ( $q_x = q_y = 0$ ); (b) dispersion relation of both cavity modes in the 3D PC cavity array with black curve corresponds for •-X-M and red dashed curve for •-X'-M. Please note •-X-M and •-X'-M represent different ($q_x$, $q_y$) direction as shown at Figure 4-10(c).

In conclusion, we have developed a higher-order planewave incidence concept for the planewave based transfer matrix method with rational function interpolation algorithm to efficiently simulate three-dimensional photonic crystal devices. As an example, the dispersion relations and quality factors were calculated for the resonant cavity array embedded in layer-by-layer photonic crystal structure. An interesting ultra-slow negative group velocity is observed in this structure. One other advantage of TMM is that there is no limitation on the length of photonic crystal structure along the propagation direction making the TMM ideal for waveguide simulation. One other direct application of this paper is to find out the wave guide loss by means of finding the resonant Q value for different $(k_x, k_y)$.

**References:**


1. E. Yablonovitch, "Inhibited Spontaneous Emission in Solid-State Physics and Electronics," *Phys. Rev. Lett.* **58**, 2059 (1987)
2. S. John, "Strong Localization of Photons in Certain Disordered Dielectric Superlattices, " *Phys. Rev. Lett.* **58**, 2486 (1987)
3. J.D. Joannopoulos, R.D. Meade and J.N. Winn, *Photonic Crystal*, Princeton University Press, New Jersey, 1995
4. E. Özbay, G. Tuttle, M. Sigalas, C. M. Soukoulis, and K. M. Ho, "Defect structures in a layer-by-layer photonic band-gap crystal," *Phys. Rev. B* **51**, 13961 (1995)
5. A. Chutinan, and S. Noda, "Highly confined waveguides and waveguide bends in three-dimensional photonic crystal," *Appl. Phys. Lett.* **75**, 3739 (1999)
6. M. Okano, A. Chutinan, and S. Noda, "Analysis and design of single-defect cavities in a three-dimensional photonic crystal," *Phys. Rev. B* **66**, 165211 (2002)

7. A. Yariv, Y. Xu, R.K. Lee and A. Scherer, "Coupled-resonator optical waveguide: a proposal and analysis," *Optics Lett.* **24**, 711 (1999)
8. M. Bayindir, B. Temelkuran and E. Ozbay, "Tight-Binding Description of the Coupled Defect Modes in Three-Dimensional Photonic Crystals, " *Phys. Rev. Lett.* 84, 2140 (2000)
9. H. Altug and J. Vuckovic, "Two dimensional coupled photonic crystal resonator arrays, " *Appl. Phys. Lett.* **84**, 161 (2004)
10. H. Altug and J. Vuckovic, "Experimental demonstration of the slow group velocity of light in two-dimensional coupled photonic crystal microcavity arrays," *Appl. Phys. Lett.* **86**, 111102 (2005)
11. Z.Y. Li and L.L. Lin, "Photonic band structures solved by a plane-wave-based transfer-matrix method," *Phys Rev. E* **67**, 046607 (2003)
12. L. L. Lin, Z. Y. Li and K. M. Ho, "Lattice symmetry applied in transfer-matrix methods for photonic crystals," *J. Appl. Phys.* **94**, 811 (2003)
13. M. Li, Z.Y. Li, K.M. Ho, J.R. Cao and M. Miyawaki, "High-efficiency calculations for three-dimensional photonic crystal cavities," *Optics Lett.* **31**, 262 (2006)
14. K. M. Ho, C. T. Chan, C. M. Soukoulis, R. Biswas and M. Sigalas, "Photonic band gaps in three dimensions: new layer-by-layer periodic structures," *Solid State Commun.* **89**, 413 (1994)
15. V. Heine, *Group theory in quantum mechanics*, Pergamom Press, NY, 1960

# Chapter 5. Perfectly matched layer used in TMM

In numerical simulations, absorption boundary condition is very useful to define finite calculation domain which is extremely important in finite-difference time-domain method (FDTD)[1]. And numerous approaches have been introduced by FDTD exporters, in which the perfectly matched layer (PML) absorbing boundary condition[2,3,4,5] can be naturally adapted to our planewave based transfer (scattering) matrix method (TMM). As mentioned in previous chapters, TMM's key assumption is periodic boundary condition. In order to achieve finite size isolated calculation domain, we must put a finite thickness absorption boundary such as perfectly matched layer, which will absorb all the incoming waves and act like infinite boundary enclosed a finite size domain. One other application of perfectly matched layer is to put it at the end of the wave guide to simulate infinite long waveguide structures. The mode profile of one dimensional dielectric waveguide and the optical properties of sub-wavelength aluminum grating with semi-infinite substrate are examples of PML applied to TMM which illustrate the accuracy and power of the application of perfectly matched layer.

## 5.1 Motivation of introducing perfectly matched layer

The intrinsic boundary condition used in TMM is Bloch periodic boundary condition. For perfect photonic crystals (PC) simulation, the periodic boundary condition reveals the periodic nature of photonic crystal and TMM returns the properties (such as spectrum, band structure and mode profile) for the infinitely large PC structures. For more interested defective PC structures, the supercell concept and periodic boundary condition (i.e. an infinite array of defects) are adopted to approximate a single defect embedded in the infinite or finite large PC. The convergence of increasing the size of the supercell for a resonant cavity within layer-by-layer woodpile PC has been studied at section 3.2. Periodic boundary

conditions are also used in FDTD and other popular numerical methods to simulate infinitely large periodic PC structures.

In experiments and real applications the PC structures are all finite in size, and it is usually important to study the defect structure within a finite size PC. The perfectly matched layer absorption boundary condition first introduced in FDTD can be adapted to TMM to simulate finite size PC structures. Although the performance of PML has been extensively studied in FDTD, there are very few reports on PML applications to TMM method. In this chapter the theoretical foundation and detailed benchmark results of perfectly matched layer will be discussed along with several application examples.

## 5.2 Theory of perfectly matched layer and Z axis PML

### 5.2.1 Background of PML

The concept of PML was first introduced at 1994 by J.P. Berenger to improve the performance of absorption boundary conditions in FDTD methods. Later Sacks discussed in his 1995 paper that an anisotropic uniaxial material with both permittivity (dielectric constant) and magnetic permeability diagonal tensor can act as perfect match interface. The uniaxial PML is directly derived from the Maxwell Equations to realize the perfectly matched conditions. Such material can absorb all the incoming electromagnetic energy for all incidence angles, i.e. there is absolutely no reflection and transmission through this medium. Although we can not find this kind of material in nature or man-made material tile now, but we can use physical parameters to describe this special medium.

Our planewave based transfer (scattering) matrix method can treat anisotropic material naturally, which makes the anisotropic uniaxial material our ideal candidate to realize the perfectly matched absorbing condition.[6,7]

The illustration of PML of two polarizations **e-pol** (or called s wave) and **h-pol** (or called p wave) for $Z$-axis is at Figure 5-1 (a) and Figure 5-1 (b). The propagation direction is along $Z$ axis, and the interface ($XY$ plane) is perpendicular to $Z$ axis. The isotropic region at the left side of the interface has dielectric constant $\varepsilon_1$ and magnetic permeability $\mu_1$.

The anisotropic PML region right to the interface will be perfectly matched to the isotropic region if the dielectric constant tensor $\varepsilon_2$ and magnetic permeability tensor $\mu_2$ are given by Eq. (5.1) with $s_z = a + b\mathbf{i}$, any complex number. For ideal $Z$-axis PML, there will be no reflection for planewave of any incidences at all frequencies and the transmitted wave in the PML is exponential extenuated by factor $\exp(-\alpha)$ with $\alpha \sim bz\cos\theta/\lambda$ (with $b$ imaginary part of $s_z$, $z$ thickness of PML, $\lambda$ wavelength, and $\theta$ incident angle).

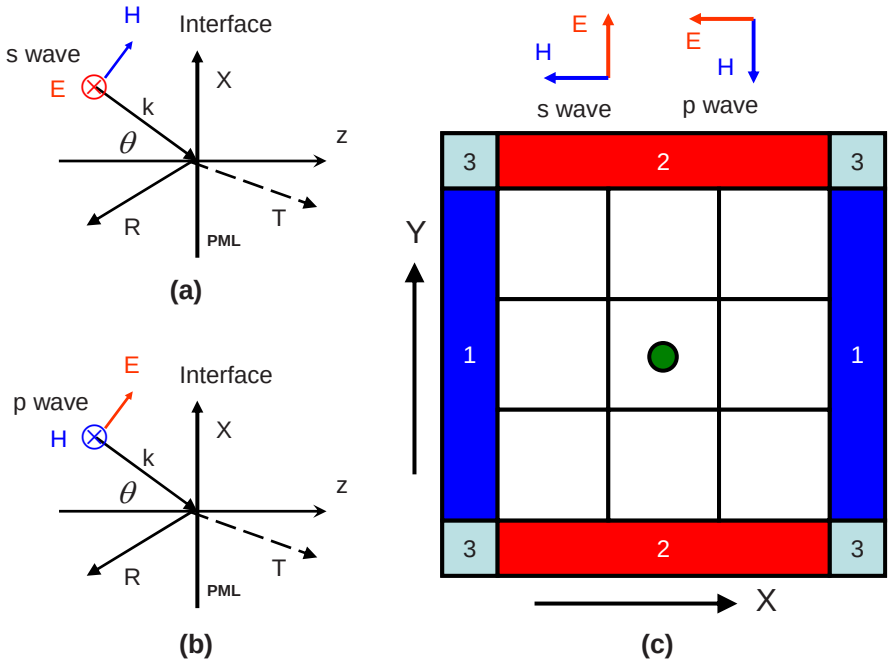


Figure 5-1: (a) **e-pol** (s wave) oblique incidence upon Z-axis PML, (b) **h-pol** (p wave) oblique incidence upon Z-axis PML: E for electric field and H for magnetic field. (c) 3x3 supercell illustration at XY plane of PC structure with a defect located at the center with s and p wave shown for normal incidence; three PML regions are labeled: 1 for X-axis side PML, 2 for Y-axis side PML, and 3 for XY corner PML.

$$\tilde{\varepsilon}_2 = \varepsilon_1 \tilde{s};\quad \tilde{\mu}_2 = \mu_1 \tilde{s}$$
$$\tilde{s} = \begin{bmatrix} s_z & 0 & 0 \\ 0 & s_z & 0 \\ 0 & 0 & 1/s_z \end{bmatrix} \qquad (5.1)$$

In FDTD simulation with finite spatial sampling, to get the ideal PML performance, fine tuning of $s_z$ is required and sometimes multiple layers of different $s_z$ are used, such as polynomial-graded PML. But in our TMM method, for the $Z$ axis perfectly matched layer, a single layer with thickness half of the unit cell and $s_z = 4 + 4\mathbf{i}$ is good enough (detail at section 5.2.2).

### 5.2.2 Performance of simple parameter approach

The following are the performance of the $Z$ -axis perfectly matched layer of $s_z = 4 + 4\mathbf{i}$ with thickness of $0.5a_0$ ($a_0$ the unit cell lattice constant) for the normal incidence case ($\theta = 0$). At Figure 5-2, the reflection rate of a long frequency range (0 to 10 normalized frequency) is plotted: for both **e** and **h** polarizations the reflection rate is below -250dB and excellent match condition is observed. At Figure 5-3, the transmission rate after the $0.5a_0$ thick perfectly matched layer is plotted: for both **e** and **h** polarizations the transmission is decreasing exponentially when the normalized frequency increases.

The larger the normalized frequency, the shorter the wave length and more number of wavelength in the $0.5a_0$ thickness, so the more absorption (less transmission) from the perfectly matched layer is observed. But even with normalized frequency 0.2, the transmission is less than 1%. To make better performance of the perfectly matched layer at lower frequency range, we can increase the thickness of layer. With the increase of the thickness, the reflection rate remains the same while the transmission rate is decreased exponentially.

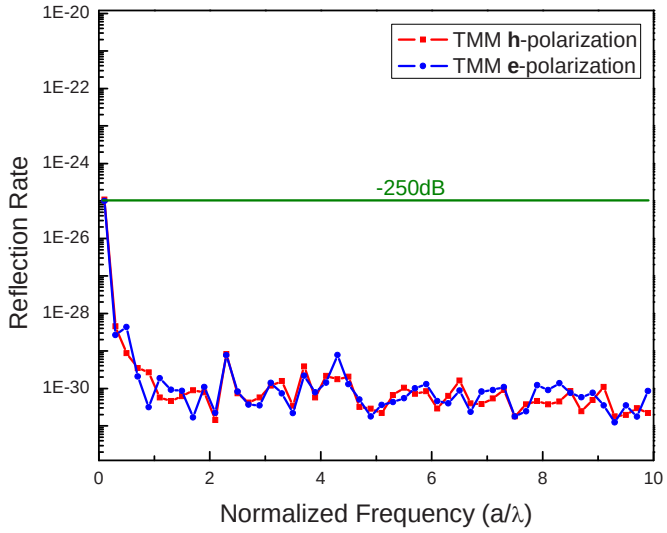


Figure 5-2: Reflection from perfect match interface

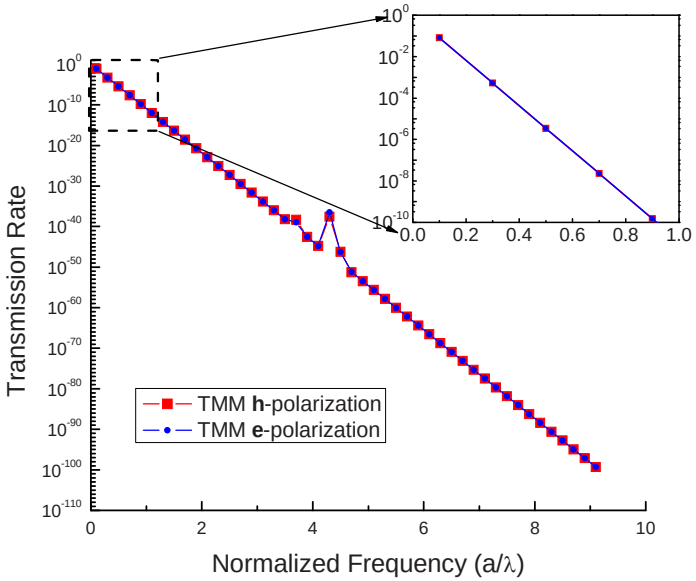


Figure 5-3: Transmission rate after the perfect match layer

In the formulation, the result is independent of incident angles; but in the real work numerical simulation, the performance of the perfectly matched layer is indeed depending on the

incidence angle and there are a lot of studies on how to improve the large angle incidence perfectly matched layer performance in FDTD research fields.

Fortunately, our TMM method does not require much attention on that issue. Although, the performance do vary when the incidence angle changes, the overall performance is still excellent: at Figure 5-4 the reflection rate is calculated for incidence angle range from 0 to 89 degree for normalized frequency 0.4 and perfectly matched layer thickness $0.5a_0$ and $s_z = 4 + 4\mathbf{i}$. Even for very high incidence angle 89 degree, the refection is below 190 dB for both polarizations. The transmission rate is also calculated for various angles and the result is plotted at Figure 5-5 for normalized frequency 0.4 and perfectly matched layer thickness $0.5a_0$ and $s_z = 4 + 4\mathbf{i}$. We can see that the performance is OK for smaller incidence angle (for example around 0.1 transmission rate at 80 degree). But the transmission is larger than 0.5 when the incidence angle approach to 90 degree. Although the electromagnetic wave maybe in a distribution of incidence angles and high incidence angle components is rare, we still need to be very careful when apply the perfectly matched layer and assume the transmission is purely zero case.

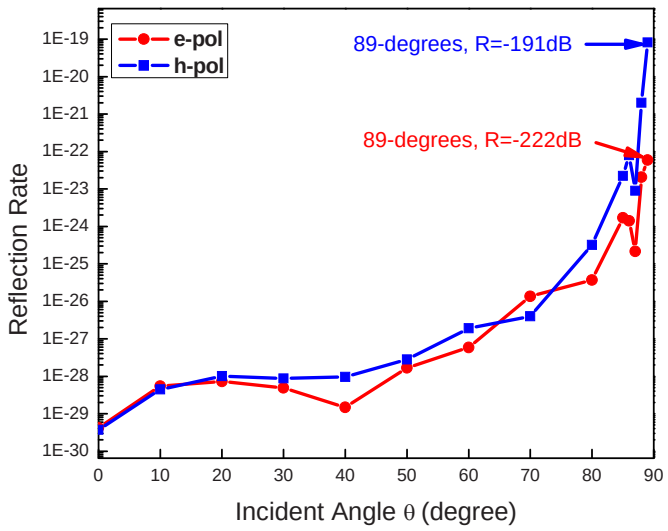


Figure 5-4: Reflection rate vs. incidence angle

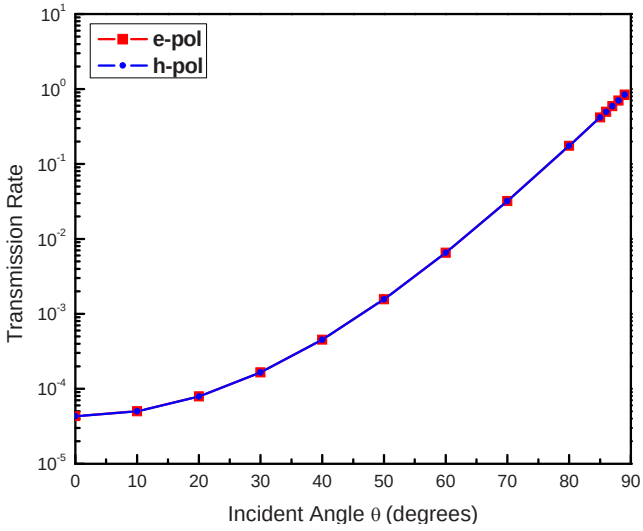


Figure 5-5: Transmission rate vs. incidence angle

### 5.2.3 Two strategies to improve the performance

Two strategies are studied to improve the performance of PML in term of attenuating the transmission: one is to increase the imaginary part of $s_z$ and the other is to increase the thickness of the PML. Both approaches have the same effect to increase of the attenuation factor $\alpha \sim bz\cos\theta/\lambda$. The transmittance and reflectance of both methods are illustrated at Figure 5-6 with both cases: double the thickness of PML and double the imaginary part of $s_z$. As shown Figure 5-6 (a), the performance of PML is improved for all incident angles, but when the incident angle approaches to 90 degree, the transmittance is always approaching to 100%; while the perfectly matched condition (no reflection) still remains valid for all angles (Figure 5-6 (b)).

Further studies such as grading of PML are required to further improvement of the transmittance attenuation performance. Even without grading, the reflectance is already below $10^{-20}$ which is much better than the complicated grading PML in FDTD.

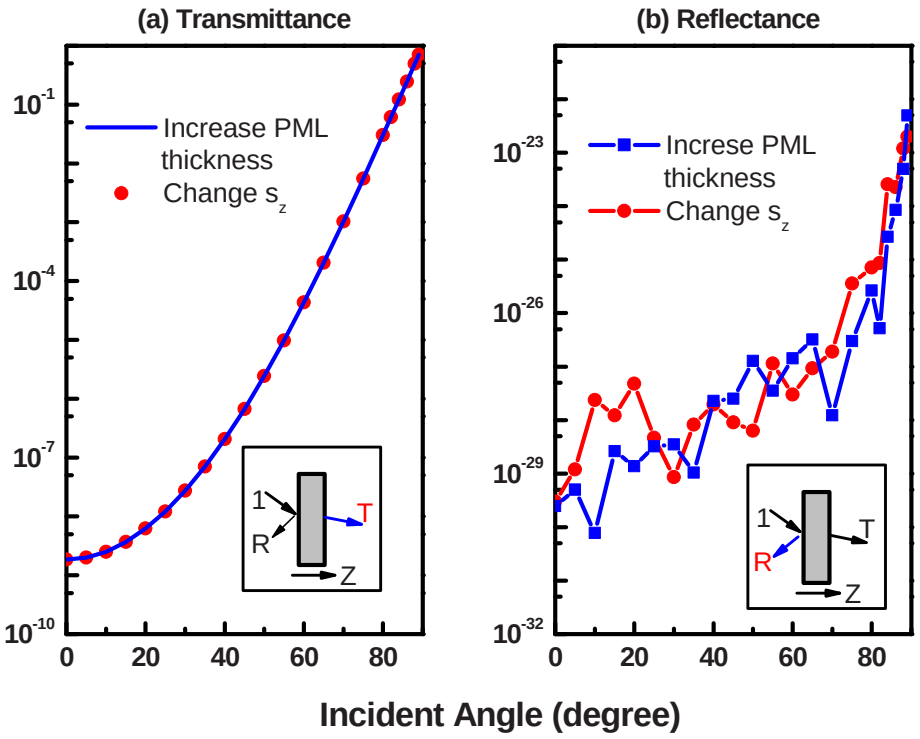


Figure 5-6: Two approaches to improve the performance of Z-axis PML -- double the thickness of PML and double the imaginary part of $s_z$ : (a) transmittance is attenuated more for every incidence angle but still approaches to 100% as incidence angle approaches 90 degree, (b) reflectance is still perfectly matched for all incidence angles. Only s wave shows, p wave presents the same behaviors.

### 5.2.4 Application of PML to periodic 1D waveguide

Now we can apply the $Z$ direction perfectly matched layer to one dimensional waveguide structure illustrated at Figure 5-7: the blue region represents dielectric material ($\varepsilon = 5.76$) and the background is air; the width of the waveguide is $d = 0.25a_0$ and the length of the waveguide is $L = 3a_0$ with $a_0$ the lattice constant along $x$ direction. The planewave is incident from left and propagating along $Z$ direction. We choose the normalized frequency $a_0 / \lambda = 0.4$.

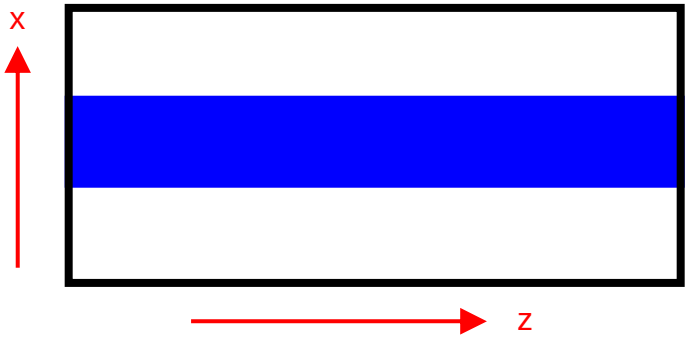


Figure 5-7: 1D wave guide (without perfect match layer)

The planewave based TMM adopts the periodic boundary condition at $Y$ direction. Due to the air-dielectric material interface termination at the end of the waveguide, a standing wave is formed which is shown clear in the mode profile plot from TMM (Figure 5-8). Those results are typical for finite length waveguide. While FDTD software can also do this task; but when it comes to infinite waveguide case, FDTD has some difficulties. We can simulate infinite long 1D waveguide by putting a layer of PML at the end of the waveguide and the mode profile distribution of electric field is plotted at Figure 5-9. The standing wave feature disappeared and guided wave presents within the waveguide slab. The PML has thickness of $0.5a_0$ with $s_z = 4 + 4\mathbf{i}$. There are very little energy penetrated into the PML and energy is absorbed exponentially as it propagates into the PML. The detailed comparison of TMM results with the analytical results will be discussed in section 5.3.2.

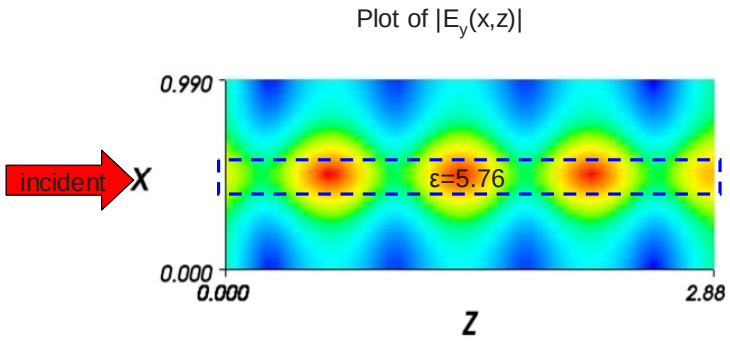


Figure 5-8: Electric field distribution within the unit cell of 1D waveguide (without putting perfect match layer at the end).

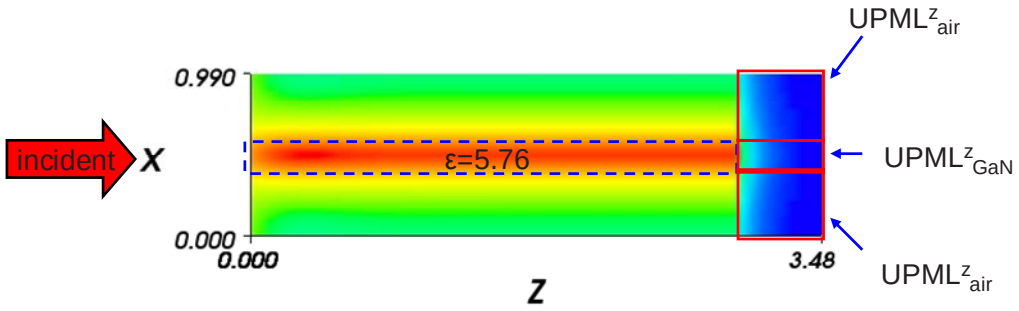


Figure 5-9: Electric field distribution within the unit cell of 1D waveguide (without putting perfect match layer at the end).

## 5.3 Perfectly matched layer for $X,Y$ axis and its application to 1D waveguide

To get perfectly matched in the $X$ or $Y$ boundary within the $XY$ plane (for example eliminating the crosstalk between neighborhood in plane supercells), we can adopt the similar relation as the $Z$-axis PML: to match $X$ boundary Eq. (5.2) should be used; to match $Y$ boundary Eq. (5.3) should be used; and to match the corner of $XY$ boundary the product of Eq. (5.2) and Eq. (5.3) should be used.

Figure 5-1 (c) illustrates three types of $XY$ plane PMLs applied to a 3x3 supercell structure with a defect embedded at center. It is tricky to get direct performance benchmark of the $X$- or $Y$-axis side PML because in TMM we can only collect spectra information in the propagation direction ($Z$-axis), while the structure is periodic along the $X$ and $Y$ axis direction. To get an idea of the performance of $X$ or $Y$ side PML, the indirect approach of electric field distribution comparison with analytical results will be utilized.

$$\tilde{s}_x = \begin{bmatrix} 1/s_x & 0 & 0 \\ 0 & s_x & 0 \\ 0 & 0 & s_x \end{bmatrix} \qquad (5.2)$$

$$\tilde{s}_y = \begin{bmatrix} s_y & 0 & 0 \\ 0 & 1/s_y & 0 \\ 0 & 0 & s_y \end{bmatrix} \tag{5.3}$$

Now we apply those perfectly matched layer at $X$ -axis and $Z$ -axis direction to 1D waveguide to see the difference between the numerical calculation and analytical results. But before the comparison, we need first derive the analytical results of the 1D infinite waveguide.

### 5.3.1 Analytical solutions of 1D dielectric slab waveguide

The one dimensional dielectric slab waveguide is discussed in many text books, such as *Optical Waves in Crystals* by Yariv and Yeh[8]. Here in this section, I outline the key steps of the derivation and list the result for our later comparison purpose. The geometry of the 1D wave guide is illustrated in Figure 5-10: the thickness of the wave guide is $d$ and centered at $x = 0$; the waveguide is uniform along $y$ and $z$ direction; the dielectric constant at region I and III is $\varepsilon_0$ while the dielectric constant at region II is $\varepsilon_1$; the guided wave will propagate along $z$ direction.

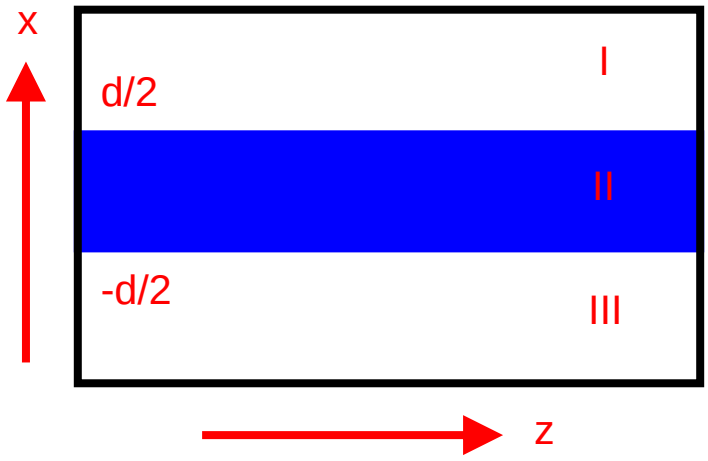


Figure 5-10: 1D wave guide analytical derivation illustraton

The Maxwell's Equations Eq. (2.6) needs to be solved in this particular structure. As along the propagation direction the whole dielectric structure is homogeneous, so the solution can be expressed as Eq. (5.4).

And the wave equation through the Maxwell's Equations can be written as Eq. (5.5) which are valid in each of the three regions (within each region $\varepsilon$ is constant instead of function of coordinate).

$$\begin{aligned}\mathbf{E}(x,y,z) &= \mathbf{E}(x,y)e^{i\beta z} \\ \mathbf{H}(x,y,z) &= \mathbf{H}(x,y)e^{i\beta z}\end{aligned} \tag{5.4}$$

$$\begin{aligned}\nabla^2\mathbf{E}(x,y,z) &= \frac{\omega^2}{c^2}\varepsilon\mathbf{E}(x,y,z) = k_0^2 n^2\mathbf{E}(x,y,z) \\ \nabla^2\mathbf{H}(x,y,z) &= \frac{\omega^2}{c^2}\varepsilon\mathbf{H}(x,y,z) = k_0^2 n^2\mathbf{H}(x,y,z)\end{aligned} \tag{5.5}$$

There is no variation along $y$ direction, so any derivative with respect to $y$ is zero. So plug Eq. (5.4) to Eq. (5.5) we can get the relations for all three regions (Eq. (5.6)). The magnetic field $\mathbf{H}(x)$ satisfies the same equation set with $\mathbf{E}(x)$ replaced by $\mathbf{H}(x)$.

$$\begin{aligned}I &: \frac{\partial^2}{\partial x^2}\mathbf{E}(x) + \left(k_0^2 n_0^2 - \beta^2\right)\mathbf{E}(x) = 0 \\ II &: \frac{\partial^2}{\partial x^2}\mathbf{E}(x) + \left(k_0^2 n_1^2 - \beta^2\right)\mathbf{E}(x) = 0 \\ III &: \frac{\partial^2}{\partial x^2}\mathbf{E}(x) + \left(k_0^2 n_0^2 - \beta^2\right)\mathbf{E}(x) = 0\end{aligned} \tag{5.6}$$

There are two different modes in this case: TE mode and TM mode. For TE mode, $E_y$, $H_x$ and $H_z$ are non-zero; for the TM mode, $H_y$, $E_x$ and $E_z$ are non-zero. We are going to solve these two modes separately. For guided mode, we need the electric field magnitude to vanish as $x \to \pm\infty$ which implies $k_0 n_0 < \beta < k_0 n_1$.

Now let's take TM mode into detail consideration which has $H_y$, $E_x$ and $E_z$ non-zero. We can take $H_y$ (Eq.(5.7)) as the independent variable and $E_x$ and $E_z$ can be derived accordingly by Eq.(5.8).

$$H(x,y,z,t) = H_y(x)e^{\mathbf{i}(\beta z - \varpi t)} \tag{5.7}$$

$$\begin{aligned} E_x(x) &= \frac{\beta}{\omega}\frac{1}{\varepsilon(x)}H_y(x) \\ E_z(x) &= \frac{\mathbf{i}}{\omega}\frac{1}{\varepsilon(x)}\frac{\partial}{\partial x}H_y(x) \end{aligned} \tag{5.8}$$

The solution of $H_y(x)$ to the three regions can be expressed as Eq. (5.9) with $k_1 = \sqrt{\beta^2 - n_0^2 k_0^2}$ , $k_2 = \sqrt{\beta^2 - n_1^2 k_0^2}$ , $k_0 = \omega / c$ and $A, B, C$ undetermined constant. The solution of $E_z(x)$ can be found from Eq. (5.8) and expressed at Eq. (5.10).

Using the continuities of $H_y(x)$ and $E_z(x)$ , we can obtain the following relations: $A = B\cos(-k_2 d/2 + \alpha)$ , $C = B\cos(k_2 d/2 + \alpha)$ , $Ak_1/n_1^2 = -Bk_2/n_2^2 \sin(-k_2 d/2 + \alpha)$ and $Ck_1/n_1^2 = Bk_2/n_2^2 \sin(k_2 d/2 + \alpha)$, which is simplified and listed at Eq. (5.11).

$$\begin{aligned} H_y^I(x) &= Ae^{k_1(x+d/2)} \\ H_y^{II}(x) &= B\cos(k_2 x + \alpha) \\ H_y^{III}(x) &= Ce^{-k_1(x-d/2)} \end{aligned} \tag{5.9}$$

$$\begin{aligned} E_z^I(x) &= \frac{\mathbf{i}k_1}{\omega n_1^2}Ae^{k_1(x+d/2)} \\ E_z^{II}(x) &= -\frac{\mathbf{i}k_2}{\omega n_2^2}B\sin(k_2 x + \alpha) \\ E_z^{III}(x) &= -\frac{\mathbf{i}k_1}{\omega n_1^2}Ce^{-k_1(x-d/2)} \end{aligned} \tag{5.10}$$

$$
\begin{aligned}
&k_1 / n_1^2 = k_2 / n_2^2 \tan\left(k_2 d/2 - \alpha\right) \\
&k_1^2 + k_2^2 = \left(n_2^2 - n_1^2\right) k_0^2, \quad \alpha = n\pi/2 \\
&A = B\cos\left(-k_2 d/2 + \alpha\right) \\
&C = B\cos\left(k_2 d/2 + \alpha\right)
\end{aligned}
\tag{5.11}
$$

For the lowest TM mode of $n = 0$ (with $\alpha = 0, B = 1, A = C = \cos\left(k_2 d/2\right)$), the dispersion relation is given by $k_1 / n_1^2 = k_2 / n_2^2 \tan\left(k_2 d/2\right)$ and $k_1^2 + k_2^2 = \left(n_2^2 - n_1^2\right) k_0^2$. Finally we get the field components expressed at Eq. (5.12).

$$
\begin{aligned}
&H_y^I(x) = Ce^{k_1(x+d/2)}, H_y^{II}(x) = \cos\left(k_2 x\right), H_y^{III}(x) = Ce^{-k_1(x-d/2)} \\
&E_x^I(x) = \frac{C\beta}{\omega n_1^2} e^{k_1(x+d/2)}, E_x^{II}(x) = \frac{\beta}{\omega n_2^2}\cos\left(k_2 x\right), E_x^{III}(x) = -\frac{\beta}{\omega n_1^2} e^{-k_1(x-d/2)} \\
&E_z^I(x) = \frac{\mathbf{i}k_1}{\omega n_1^2} e^{k_1(x+d/2)}, E_z^{II}(x) = -\frac{\mathbf{i}k_2}{\omega n_2^2}\sin\left(k_2 x\right), E_z^{III}(x) = -\frac{\mathbf{i}k_1}{\omega n_1^2} e^{-k_1(x-d/2)}
\end{aligned}
\tag{5.12}
$$

Similar approach can be applied to the TM mode and $E_y, H_x$ and $H_z$ at three regions can be found.

### 5.3.2 Numerical results of TMM with side PMLs

After we get the analytical results for the 1D infinitely long dielectric waveguide, detailed quantified comparison with TMM calculation can be done. The mode profile of 1D dielectric waveguide with *z* axis only PML has been plotted at Figure 5-9. Due to the periodic boundary condition along *x* axis, this result is a set of infinite parallel dielectric waveguide array. Although the interaction between neighborhood waveguide is small, the result at Figure 5-9 is still not identical to the analytical solution. To eliminate the cross talk between neighborhood waveguide, the side wall PMLs are added as shown at Figure 5-11. To get detailed comparison, we take layer #48 shown as blue dashed line at Figure 5-11 and plotted at Figure 5-12 which is for TE mode with $E_y$ non zero. Without the x-sidewall PML, the

magnitude of electric field $y$ component is larger than the analytical result at the edge of the unit cell ($x = \pm 0.5a$) due to the interaction between neighborhood waveguides; the results within the waveguide's dielectric material region is very close. With the $x$-sidewall PML, the performance is improved and the TMM calculation results are more consistent with analytical results at the edge of the unit cell boundary.

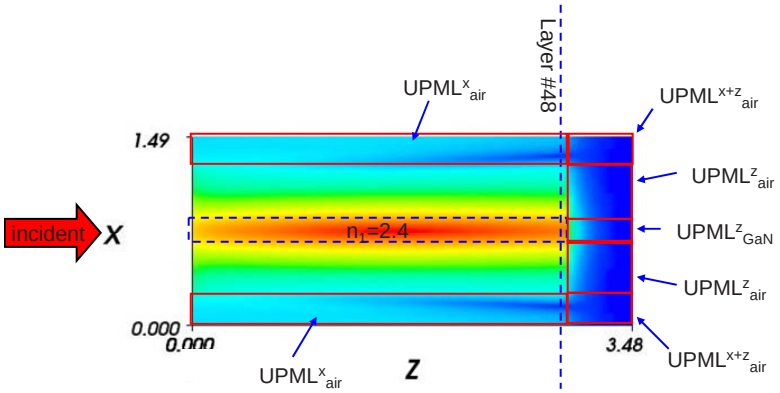


Figure 5-11: Mode profile of 1D dielectric waveguide with side PML

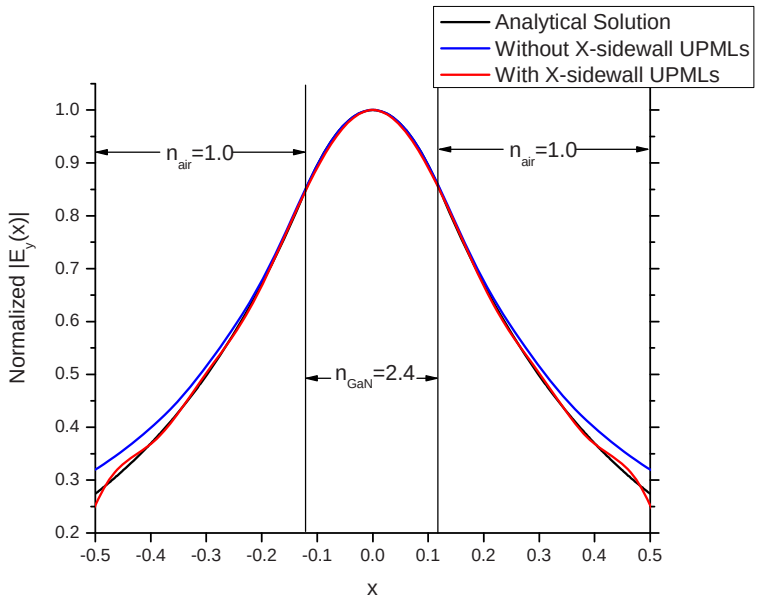


Figure 5-12: Detailed comparison of electric field magnitude with analytical solutions

## 5.4 PML application example: dispersive sub-$\lambda$ aluminum grating

As the experimental technique improved in recent years, the proposed future devices used in optics and laser are getting smaller and smaller. Those recently proposed devices are so small that sometimes much smaller than the wavelength of interested electromagnetic wave. TMM can be applied directly to sub-$\lambda$ components such as resonant cavity, waveguide, grating etc. In this section, the sub-$\lambda$ aluminum grating is studied with the application of PML to simulate infinite thick substrate at visible light frequency.

The geometry of the grating is illustrated at Figure 5-13. It is periodic along $x$ direction and uniform along $y$ direction. The incident planewave is from top and propagates along the $z$ direction with azimuthally incident angle $\theta = 7^0$. The aluminum width is 0.068 $\mu m$, and the air width is 0.102 $\mu m$. So the lattice constant along $x$ direction is 0.17 $\mu m$ and the filling ration is 40 %. The thickness of the grating is 0.136 $\mu m$. The substrate is made by $SiO_2$ with refractive index $n_{sub} = 1.55$. We calculate two cases of different substrate thickness: one with finite thickness of 0.5 $mm$ and the other with infinite thickness by applying PML at the end of the substrate. The refractive index of dispersive aluminum is listed at Table 5-1 with $\tilde{n} = n + ik$.

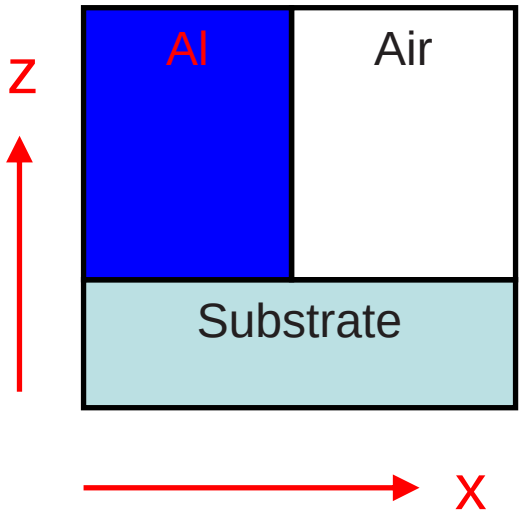


Figure 5-13: Geometry sub-wavelength of metal grating

Table 5-1: refractive index of Aluminum at visible wavelength

| wavelength ($\mu m$) | n | k | wavelength ($\mu m$) | n | k |
|---|---|---|---|---|---|
| 0.344389 | 0.364 | 4.17 | 0.550044 | 0.95 | 6.69 |
| 0.350028 | 0.375 | 4.24 | 0.551022 | 0.96 | 6.7 |
| 0.354229 | 0.385 | 4.3 | 0.563545 | 1.02 | 6.85 |
| 0.364647 | 0.407 | 4.43 | 0.576651 | 1.08 | 7 |
| 0.375697 | 0.432 | 4.56 | 0.590381 | 1.15 | 7.15 |
| 0.387438 | 0.46 | 4.71 | 0.600097 | 1.2 | 7.26 |
| 0.399935 | 0.49 | 4.86 | 0.604781 | 1.22 | 7.31 |
| 0.413267 | 0.523 | 5.02 | 0.6199 | 1.3 | 7.48 |
| 0.427517 | 0.558 | 5.2 | 0.635795 | 1.39 | 7.65 |
| 0.442786 | 0.598 | 5.38 | 0.64979 | 1.47 | 7.79 |
| 0.450018 | 0.618 | 5.47 | 0.652526 | 1.49 | 7.82 |
| 0.459185 | 0.644 | 5.58 | 0.670162 | 1.6 | 8.01 |
| 0.476846 | 0.695 | 5.8 | 0.688778 | 1.74 | 8.21 |
| 0.49592 | 0.755 | 6.03 | 0.700056 | 1.83 | 8.31 |
| 0.499919 | 0.769 | 6.08 | 0.708457 | 1.91 | 8.39 |
| 0.506041 | 0.789 | 6.15 | 0.729294 | 2.14 | 8.57 |
| 0.516583 | 0.826 | 6.28 | 0.75003 | 2.4 | 8.62 |
| 0.527575 | 0.867 | 6.42 | 0.751394 | 2.41 | 8.62 |
| 0.539044 | 0.912 | 6.55 | 0.774875 | 2.63 | 8.6 |

There are two polarizations for this case: TE polarization (s wave) has the electric field vector perpendicular to the incident plane and TM polarization (p wave) has the electric field vector in the incident plane.

First the sub-$\lambda$ grating with finite thickness of $0.5\,mm$ is calculated; the reflection rates of both polarizations are plotted at Figure 5-14 (a). For TE mode, the reflection is very high (around 90%) and it is almost a constant in the whole visible light frequency range. But for TM mode, it is quiet different. The most obvious different feature compared with TE mode is the oscillations in the whole spectrum which is due to the interference with the strong reflection from the interface of the substrate end to the air. The reflection rate of TM mode change a lot within the visible light range and at around $0.45\mu m$ the reflection is almost zero. This can be used as the polarization light splitter to separate different polarizations.

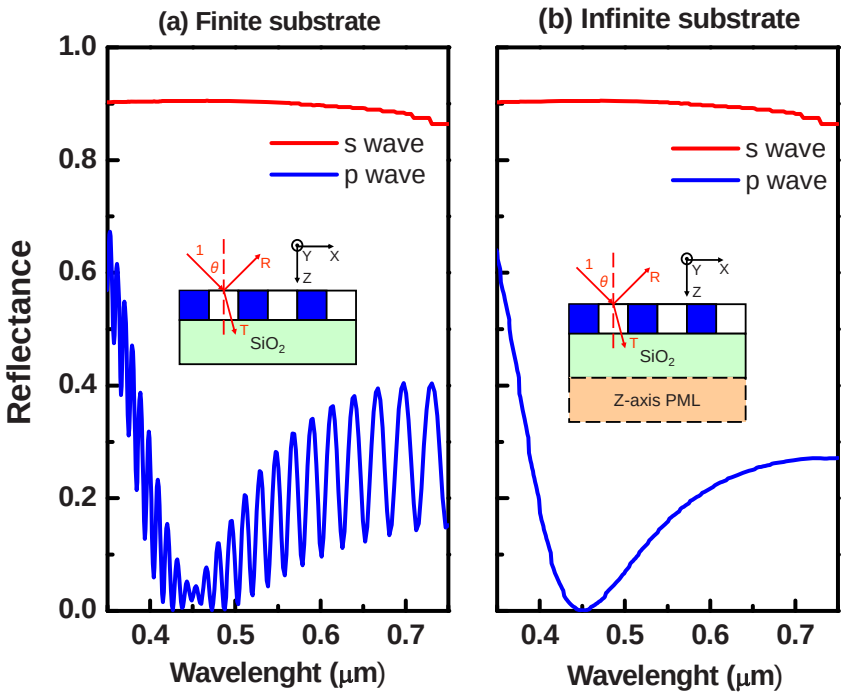


Figure 5-14: Reflection rate of finite thickness sub-wavelength grating Reflectance of sub-wavelength grating for both s and p planewave with incident angle 7 degree at visible frequencies: (a) with finite $SiO_2$ substrate, and (b) with infinite $SiO_2$ substrate by applying Z-axis PML at the end of substrate.

Next, we did a calculation on infinite substrate case. Here we used the $z$ axis PML discussed at section 5.1 with $s_z = 4 + 4\mathbf{i}$. The reflection rate for both TE and TM polarization are plotted at Figure 5-14 (b). For TE mode, there is not much difference compared with the finite thickness substrate case. But for TM mode, the oscillation disappears for the infinite thickness of substrate. This is easy to explain because for infinite substrate, there will be no reflection from other end of the substrate and hence no interference. At wavelength of $0.45\mu m$, the TM mode's reflection rate is nearly zero, and it is perfect for polarization beam splitter.

To get better understanding of the behaviors at wavelength of $0.45\mu m$, the electric magnitude mode profiles are plotted for both TE and TM waves at Figure 5-15. The TE mode is Ey dominated, and strong reflection occur at the front of the grating which

corresponding to the high reflectance. On the other hand, the TM mode is Ex dominated and the electromagnetic energy can propagate through the grating and substrate.

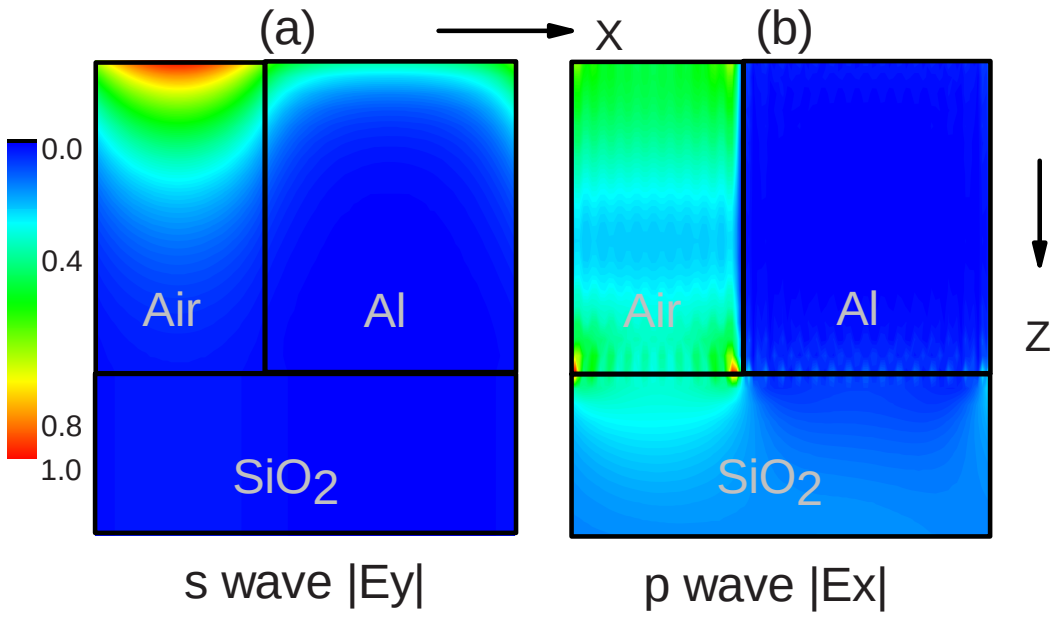


Figure 5-15: Electric field mode profiles of sub-wavelength grating for the infinite substrate case at wavelength 4.5um: (a) TE mode (s wave) incidence, Ey is dominate and electromagnetic energy is highly reflected, (b) TM mode (p wave) incidence, Ex is dominate and electromagnetic energy is 100% transmitted.

One of our recent research shows that a coordinate transformation can be applied to TMM to simulate curved waveguide structure. The result of the coordinate transformation is very similar to the PML we applied in this chapter except that the parameter of $s_z$ is a real function of coordinate.[9] Although PML is an artificial material first introduced for numerical simulation purpose, researchers are enthusiastic to seek PML-like materials or structures of controllable electric permittivity and magnetic permeability.[10,11] With those two parameters well controlled, EM wave cloaking, or invisible material can be achieved.[11] TMM can also be used in the design of such permittivity and permeability controllable materials just like the implementation of PML absorption boundary condition.

**References:**


1. Taflove and S.C. Hagness, *Computational Electrodynamics* (Artech Houses, 2000)
2. J.P. Berenger, "A perfectly matched layer for the absorption of electromagnetic-waves", *J. Computational Physics*, **114**, 185 (1994)
3. J.P. Berenger, "Perfectly matched layer for the FDTD solution of wave-structure interaction problems", *J. Computational Physics*, **127**, 363, (1996)
4. Z.S. Sacks, D.M. Kingsland, R. Lee and J.F. Lee, "A perfectly matched anisotropic absorber for use as an absorbing boundary condition", *IEEE Trans. Antennas and Propagation*, **43**, 1460 (1995)
5. S.D. Gedney, "An anisotropic perfectly matched layer-absorbing medium for the truncation of FDTD lattices", *IEEE Trans. Antennas and Propagation*, **44**, 1630 (1996)
6. Z.Y. Li and K.M. Ho, "Application of structural symmetries in the plane-wave-based transfer-matrix method for three-dimensional photonic crystal waveguides", *Phys. Rev. B* **68**, 245117 (2003)
7. Z.Y. Li and K.M. Ho, "Bloch mode reflection and lasing threshold in semiconductor nanowire laser arrays", *Phys. Rev. B* **71**, 045315 (2005)
8. Yariv and P. Yeh, Optical waves in crystal, (Wiley, 1984)
9. Z. Ye, X. Hu, M. Li and K.M. Ho, "Propagation of guided modes in curved nanoribbon waveguides", *Appl. Phys. Lett.* **89**, 241108 (2006)
10. X. Hu, C.T. Chan, J. Zi, M. Li and K.M. Ho, "Diamagnetic response of metallic photonic crystals at infrared and visible frequencies", *Phys. Rev. Lett.* **96**, 223901 (2006)
11. S.A. Cummer, B.I. Popa, D. Schurig, D.R. Smith and J. Pendry, "Full-wave simulations of electromagnetic cloaking structures", *Phys. Rev. E* **74**, 036621 (2006)

# Chapter 6. TMM extension to curvilinear coordinate system

The planewave based transfer (scattering) matrix method is developed in curvilinear coordinates to study the guided modes in curved nanoribbon waveguides. The problem of a curved structure is transformed into an equivalent straight structure with spatially-dependent tensors of dielectric constant and magnetic permeability. We investigate the coupling between the eigenmodes of the straight part and those of the curved part when the waveguide is bent. We show that curved sections can result in strong oscillations in the transmission spectrum similar to the recent experimental results in reference 1. This chapter is modified from a paper published at *Applied Physics Letters* **89**, 241108 (2006) with title: "Propagation of guided modes in curved nanoribbon waveguides", by Z. Ye, X. Hu, M. Li, K. Ho and P. Yang.

## 6.1 Transform into curvilinear coordinate

In previous chapter, the planewave based transfer matrix method (TMM) is mainly used in Euclidian coordinate system ( $x, y, z$ ). The unit cells for any applicable structures are all rectangular in $xy$ plane and straight at the propagation direction ( $z$ axis). Although non-orthogonal lattice can be taken in the $xy$ plane; it is not possible to deal with any structure that has any curvature along the propagation direction ( $z$ axis). To study the properties of curved photonic crystal structures, we need to re-develop the TMM algorithm in curvilinear coordinate system ( $x', y', s$ ) following previous work on curvilinear coordinate system.[2]

The relation between the Euclidian coordinate system and the curvilinear coordinate system is illustrated at Figure 6-1. For Euclidian coordinate system, $x, y, z$ are perpendicular parewisely and the propagation direction is $z$ axis; for curvilinear coordinate system, $s$ is

the propagation direction and $x$ axis is always pointing to the center of the curvature of radius R. The relation between the Euclidian system and curvilinear system can be expressed by Eq. (6.1). Let $\left(x^1, x^2, x^3\right)$ be the coordinates of Euclidian system and $\left(q^1, q^2, q^3\right)$ be the coordinates of curvilinear system. The new coordinate system can be characterized by its covariant basis vector $\vec{a}_i$ and metric $g_{ij}$ defined by Eq. (6.2). In our curvilinear system case, the covariant basis vector and metric is expressed at Eq. (6.1) and Eq. (6.2).

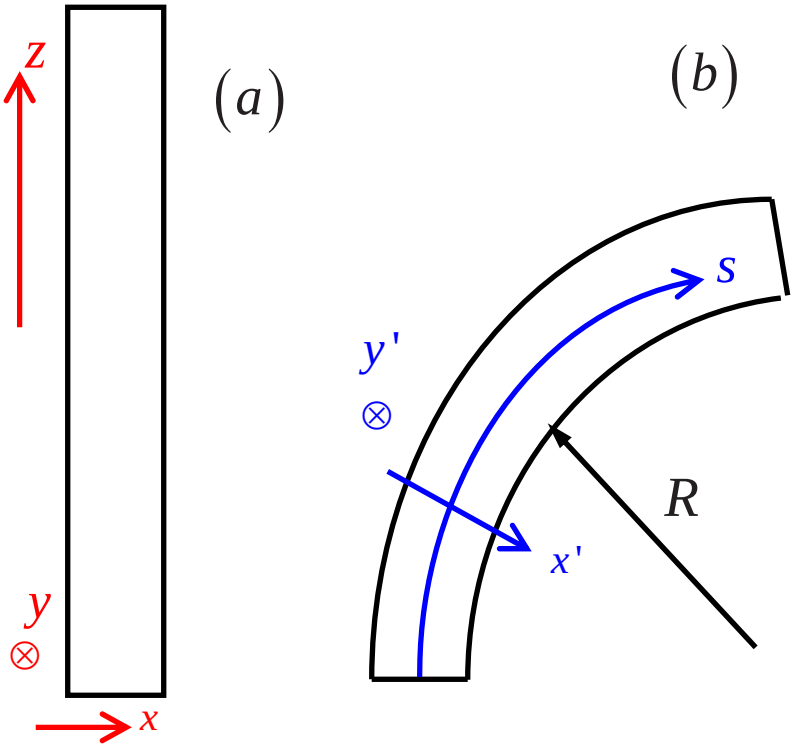


Figure 6-1: Coordinate system (a) Euclidian (b) curvilinear

$$
\begin{aligned}
x &= x'\cos\frac{s}{R} + R\left(1-\cos\frac{s}{R}\right) \\
y &= y' \\
z &= -x'\sin\frac{s}{R} + R\sin\frac{s}{R}
\end{aligned}
\tag{6.1}
$$

$$\vec{a}_i = \left( \frac{\partial x^1}{\partial q^i}, \frac{\partial x^2}{\partial q^i}, \frac{\partial x^3}{\partial q^i} \right)$$
$$g_{ij} = \frac{\partial x^k}{\partial q^i} \frac{\partial x^k}{\partial q^j} \tag{6.2}$$

$$\vec{a}_{x'} = \left( \cos\frac{s}{R}, 0, -\sin\frac{s}{R} \right)$$
$$\vec{a}_{y'} = (0,1,0) \tag{6.3}$$
$$\vec{a}_{s'} = \left( -\frac{x'}{R}\sin\frac{s}{R} + \sin\frac{s}{R}, 0, -\frac{x'}{R}\cos\frac{s}{R} + \cos\frac{s}{R} \right)$$

$$g_{ij} = \begin{pmatrix} 1 & 0 & 0 \\ 0 & 1 & 0 \\ 0 & 0 & \left(1 - \frac{x'}{R}\right)^2 \end{pmatrix} \tag{6.4}$$

Now we can apply the coordinate transformation toward Maxwell's Equations in terms of differential equations relating to the transverse components of fields (Eq.(6.5) with some parameters defined at Eq. (6.6)).

$$\frac{\partial E_{x'}}{\partial s} = \frac{\partial}{\partial x'}\left[-\frac{1}{\mathbf{i}k_0\varepsilon_3}\left(\frac{\partial H_{y'}}{\partial x'} - \frac{\partial H_{x'}}{\partial y'}\right)\right] + \mathbf{i}k_0\mu_2 H_{y'}$$
$$\frac{\partial E_{y'}}{\partial s} = \frac{\partial}{\partial y'}\left[-\frac{1}{\mathbf{i}k_0\varepsilon_3}\left(\frac{\partial H_{y'}}{\partial x'} - \frac{\partial H_{x'}}{\partial y'}\right)\right] - \mathbf{i}k_0\mu_1 H_{x'}$$
$$\frac{\partial H_{x'}}{\partial s} = \frac{\partial}{\partial x'}\left[\frac{1}{\mathbf{i}k_0\mu_3}\left(\frac{\partial E_{y'}}{\partial x'} - \frac{\partial E_{x'}}{\partial y'}\right)\right] - \mathbf{i}k_0\varepsilon_2 E_{y'} \tag{6.5}$$
$$\frac{\partial H_{y'}}{\partial s} = \frac{\partial}{\partial y'}\left[\frac{1}{\mathbf{i}k_0\mu_3}\left(\frac{\partial E_{y'}}{\partial x'} - \frac{\partial E_{x'}}{\partial y'}\right)\right] + \mathbf{i}k_0\varepsilon_1 E_{x'}$$

$$\varepsilon_1 = \varepsilon_2 = \varepsilon\alpha, \mu_1 = \mu_2 = \mu\alpha$$
$$\varepsilon_3 = \frac{\varepsilon}{\alpha}, \mu_3 = \frac{\mu}{\alpha}, \alpha = \left(1 - \frac{x'}{R}\right) \tag{6.6}$$

So the arc structure can be viewed as a straight one with effective $\tilde{\varepsilon}$ and $\tilde{\mu}$ tensors depending on the transverse coordinate $x'$ with the relation displayed at Eq. (6.7). Giving a close look toward Eq. (6.7), we can notice that they have the same formation as the uni-axial perfect match layer discussed at reference 2 but with the elements $\varepsilon_1, \varepsilon_2, \varepsilon_3, \mu_1, \mu_2, \mu_3$ function of coordinate. One other difference between perfect match layer and curvilinear coordinate transformation is that: for PML, each element is a complex number in which the imaginary part plays the role of absorption; for curvilinear coordinate transformation, each element is a real number. The curved part of the waveguide is perfectly matched with the straight part in the $s$ direction, but not it the $x', y'$ directions.

$$\tilde{\varepsilon} = \begin{pmatrix} \varepsilon_1 & 0 & 0 \\ 0 & \varepsilon_2 & 0 \\ 0 & 0 & \varepsilon_3 \end{pmatrix}, \tilde{\mu} = \begin{pmatrix} \mu_1 & 0 & 0 \\ 0 & \mu_2 & 0 \\ 0 & 0 & \mu_3 \end{pmatrix} \qquad (6.7)$$

When the curved waveguide is effectively considered as a straight one with $\tilde{\varepsilon}$ and $\tilde{\mu}$ given by Eq. (6.6) and Eq. (6.7), we can apply the well-developed planewave TMM to calculate the dispersion relations and eigenmode profiles in the curved waveguide. Semiconductor nanowires can nanoribbons have many promising optoelectronic applications such as waveguide[1,3], lasers[4-6], optical switches, and sensors[7].

## 6.2 Curved waveguide simulation

With the knowledge of the curvilinear coordinate transformation for TMM, we can study the curved waveguide structure in detail. The geometry used in this section is similar to the experiment done in reference 1. The refractive index of the background, square waveguide, substrate is: $n_0 = 1.0$ , $n_1 = 2.1$ , $n_2 = 1.5$ respectively. The cross-section of the square nanoribbon waveguide is $360nm(x') \times 250nm(y')$, shown as Figure 6-2.

The dispersion relations can be calculated for both the straight waveguide (a) and the arc one with $R = 2\mu m$ (b) which are shown in Figure 6-3; the insets give the $|E_x|$ distribution for the first mode and $|E_y|$ distribution for the second mode at $600\,nm$.

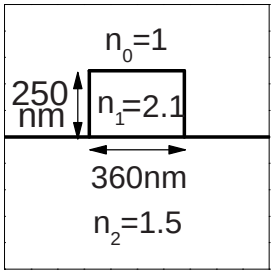


Figure 6-2: Geometry illustration of nanoribbon waveguide

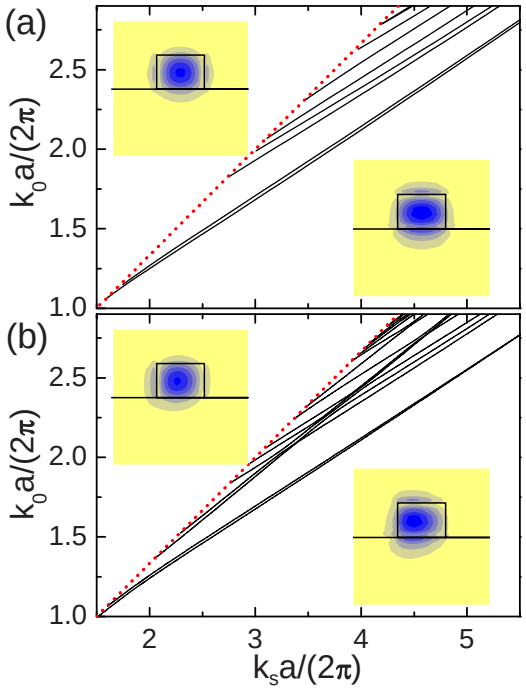


Figure 6-3: Dispersion relations of straight (a) and curved waveguide (b) with the supercell lattice constant $a = 1\mu m$. The dashed line is the light line in substrate: $k_s = n_2 k_0, (k_0 = 2\pi/\lambda)$. The left inset is the $|E_x|$ distribution of the first mode and the right inset is the $|E_y|$ distribution of the second mode at $\lambda = 600nm$.

The guided modes move downwards for a bent waveguide and the modal field shifts outwards from the center of curvatures ($-x'$ direction)[8,9]. The first and fourth modes are $E_x$ polarized, and the second and third modes are $E_y$ polarized. Modes after the fifth mode are not as highly polarized as the first four modes.

We consider the transmission coefficients for a curved waveguide joint between two straight waveguides. Here we only present the self transmission coefficients of guided eigenmode $i\left(i=1,2,...\right)$, which is defined as the ratio of the transmission energy flux of particular mode $i$ and the incident energy flux (only mode $i$ incident).

The reason for doing this is that in propagation along the straight waveguide, we expect some guided modes are much more sensitive to waveguide imperfections (such as sidewall roughness) than others. These sensitive modes are much more likely to disappear during propagation.

We start from a simple "U" shape structure, made of two semi-infinite straight waveguides connected by a semicircular waveguide (see the inset in Figure 6-4 (a)). First we set $R=10\mu m$. The self transmission of the first six guided eigenmodes is shown in Figure 6-4 (a). One can see regular fluctuations in transmission like in reference 1 but with much weaker amplitude. The reflection is very small ($<10^{-4}$, not shown here). That agrees well with the above analysis of $\tilde{\varepsilon}$ and $\tilde{\mu}$ given by Eq. (6.6) and Eq. (6.7).

Then we try an "L" structure, made of two semi-infinite straight waveguides connected by a quarter-circular waveguide with $R=20\mu m$. The result is shown in Figure 6-4 (b). The amplitude of transmission fluctuation is even weaker; but the position of the transmission peaks and bottoms of the first four modes are about the same compared to Figure 6-4 (a). It is interesting that the first two $E_x$ polarized modes (the 1st and 4th modes) have almost the same period, and the first two $E_y$ polarized modes (the 2nd and 3rd modes) also do so.

We tested structures with different curvatures and different span lengths. We found that: (i) the amplitude of transmission fluctuation decreases as $R$ is increased and (ii) the period of transmission fluctuation is only related to the span length of the arc part and decreases as we extend the arc part. The first rule is natural to understand. Smaller radius of curvature enlarges the perturbation to the system, causing the transmission to fluctuate more intensively (see Figure 6-4 (c), where $R$ is set to be $4\mu m$). The second rule can be explained by mode conversion.

Let us begin from a simple model. Suppose there are two modes in the waveguide marked $i$ and $j$ for the straight part and $i'$ and $j'$ for the curved part. If the arc part has length $L$, we can write down the self-transmission of mode $i$ when the reflection is very small: $|t_{ii'}e^{ik_{i'}'L}t_{i'i}+t_{ij'}e^{ik_{j'}'L}t_{j'i}|^2=|t_{ii'}|^4+|t_{ij'}|^4+2|t_{ii'}|^2|t_{ii'}|^2\cos(\Delta k'L)$ where $\Delta k'=k_j'-k_i'$; $t_{ii'},t_{i'i},t_{ij'},t_{j'i}$ are the convention coefficients from mode $i$ to $i'$, $i'$ to $i$, $i$ to $j'$ and $j'$ to $i$ respectively, and $t_{ii'}=t_{i'i}^*,t_{ij'}=t_{j'i}^*$. Because $\Delta k'$ is not very sensitive to $R$, the period of transmission fluctuation is mainly related to the span length $L$ of the arc part. The conversion between modes with the same polarization is much stronger than between different polarization modes. So the $1st$, $4th$ modes have similar self-transmission periods and the $2nd$, $3rd$ modes also have similar periods. However, higher order modes are not highly polarized in either $x$ or $y$ direction. The conversion rates between different polarized modes are not small. So their self-transmissions do not show fluctuations as regular as the first four modes (see the bottom plots of Figure 6-4 (a) and (b)).

Our numerical results suggest a possible explanation for the strong regular oscillation in the output spectrum observed by Law et al. The observed oscillations can be caused by a rippling section of nanoribbon (as shown in Figure 6-5 inset), which has a small bending radius for the curved part. We calculate the structure in Figure 6-5 inset for different parameters, and one of the results is shown in Figure 6-5. The parameters are: $R=3\mu m$, $L_1=1\mu m$, $L_2=5\mu m$ and *2* periods of fluctuations (Figure 6-5 inset only shows *1* period). The self-

transmission diagram exhibit similar strong oscillations in the 3rd, 4th and 5th modes as in reference. 1.

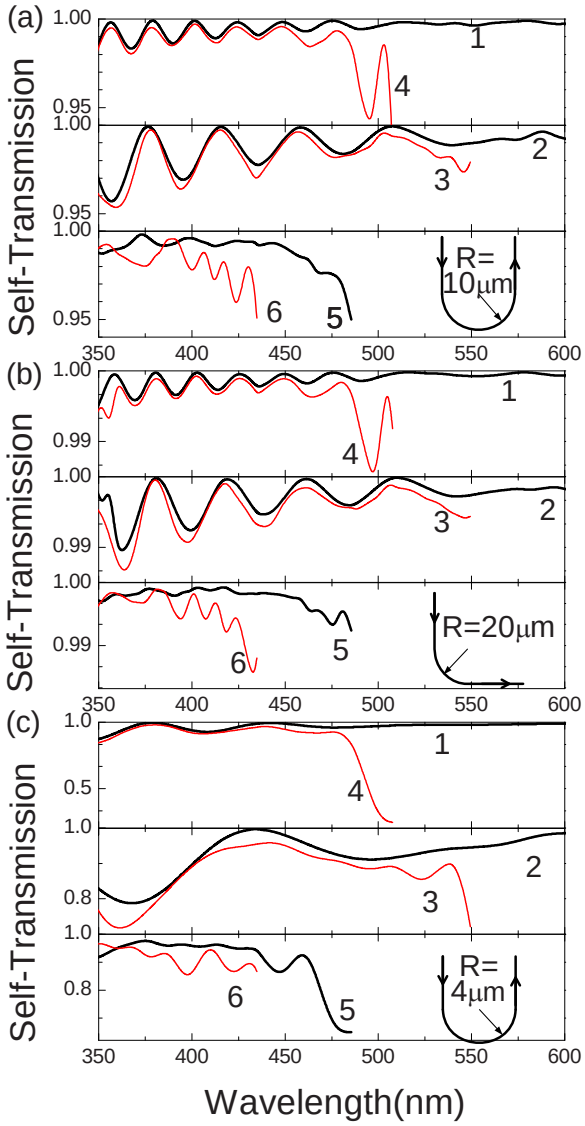


Figure 6-4: Self-transmission of the first six modes numbered from 1 to 5 for: (a): "U" structure of $R = 10\mu m$, (b): "L" structure of $R = 20\mu m$, and (c): "U" structure of $R = 4\mu m$. Mode 1 and mode 3 have the similar pattern; while mode 2 and mode 4 have the similar pattern.

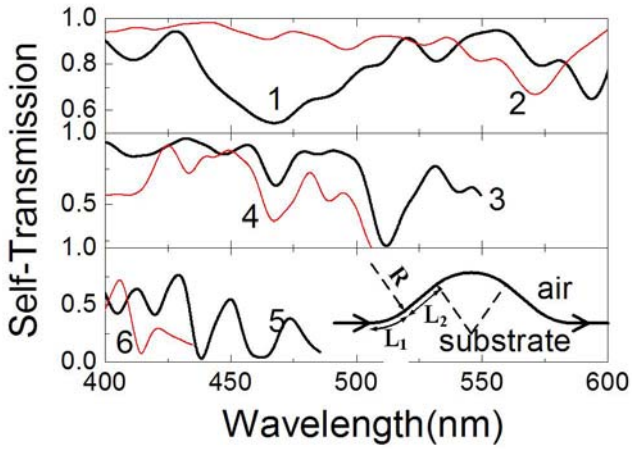


Figure 6-5: Self-transmission of the first six modes for the structure in the inset but of two periods of fluctuation, when $R = 3\mu m$, $L_1 = 1\mu m$ and $L_2 = 5\mu m$. Inset: illustration of a waveguide containing a rippling section.

In summary, we have developed an improved TMM method in curvilinear coordinates to study curved nanoribbon waveguides. Our method can be applied to any shape of curved waveguides. From our results we can extract and explain two rules concerning the period and multitude of the transmission fluctuations. We finish by calculating a rippling waveguide structure and obtain oscillations in transmission similar to those observed in experiments.

**References:**

1. M. Law, D.J. Sirbuly, J.C. Goldberger, R.J. Saykally, and P. Yang, "Nanoribbon Waveguides for Subwavelength Photonics Integration", *Science* **305**, 1269 (2004)
2. M. Skorobogatiy, S. Jacobs, S. Johnson, Y. Fink, "Geometric variations in high index-contrast waveguides, coupled mode theory in curvilinear coordinates", *Opt. Express*, **10**, 1227 (2002)
3. C.J. Barrelet, A.B. Greytak, and C.M. Lieber, "Nanowire Photonic Circuit Elements", *Nano Lett.* **4**, 1981 (2004)

4. M.H. Huang, S. Mao, H. Feick, H.Q. Yan, Y.Y. Wu, H. Kind, E. Weber, R. Russo, and P.D. Yang, "Room-temperature ultraviolet nanowire nanolasers", *Science* **292**, 1897 (2001)
5. X. Duan, Y. Huang, R. Agarwal, and C.M. Lieber, "Single-nanowire electrically driven lasers", *Nature (London)* **421**, 241 (2003)
6. A.V. Masolv and C.Z. Ning, "Reflection of guided modes in a semiconductor nanowire laser", *Appl. Phys. Lett.* **83**, 1237 (2003)
7. H. Kind, H. Yan, B. Messer, M. Law, and P. Yang, "Nanowire ultraviolet photodetectors and optical switches", *Adv. Mater. (Weinheim, Ger.)* **14**, 158 (2002)
8. V. Van, P.P. Absil, J.V. Hryniewicz, and P.T. Ho, "Propagation loss in single-mode GaAs-AlGaAs microring resonators: Measurement and model", *J. Lightwave Technol.* **19**, 1734 (2001)
9. Y.A. Vlasov and S.J. McNab, "Losses in single-mode silicon-on-insulator strip waveguides and bends", *Opt. Express* **12**,1622 (2004)

# Chapter 7. Application of TMM to diffractive optics

Besides the magnitude of the electromagnetic wave transmission or reflection rate, the planewave based transfer (scattering) matrix method (TMM) can also calculate the phase information of the electric or magnetic field. When the phase at every point of a plane is determined by the geometry (shape of a structure) and composition (material with different refractive indices), the properties of electromagnetic wave or light (such as bending, focusing) can be determined.[1] Photonic crystal structure can be designed to meet certain purpose in controlling the behaviors of electromagnetic wave. For example, dielectric grating (1D photonic crystal) has been proposed to apply to camera lens to eliminate chromatic aberrations.[2] In this chapter, TMM is developed to calculate the phase difference and in turn to design novel photonic crystal structures for various applications.

## 7.1 Finding phase by TMM

The spectrum can be obtained by finding the Poynting vector through Eq. (2.53) at Section 2.6.1. Before the Poynting vector is calculated, TMM has already obtained the electric field in term of complex vector ($E_t$, $E_r$) for transmission and reflection wave by Eq. (2.52). The information of the complex electric field vectors is used to calculate the spectrum, and the phase factor information of this complex electric field vectors is used to obtain the phase of the electric field in the range of $(-\pi, \pi)$.

Let's denote the imaginary and real part of the $E_t$ or $E_r$ at Eq. (2.52) to be *Im* and *Re* respectively and the mode (or absolute value) of $E_t$ or $E_r$ at Eq. (2.52) to be *Ab*, then the phase of the electric field ($E_t$ or $E_r$) can be found by Eq. (7.1).

$$
\begin{aligned}
&\varphi = \arcsin\left(\frac{Im}{Ab}\right) \quad if \quad Im \geq 0 \quad and \quad Re \geq 0 \\
&\varphi = \pi - \arcsin\left(\frac{Im}{Ab}\right) \quad if \quad Im \geq 0 \quad and \quad Re < 0 \\
&\varphi = -\pi + \arcsin\left(\frac{-Im}{Ab}\right) \quad if \quad Im < 0 \quad and \quad Re < 0 \\
&\varphi = -\arcsin\left(\frac{-Im}{Ab}\right) \quad if \quad Im < 0 \quad and \quad Re \geq 0
\end{aligned}
\tag{7.1}
$$

Cautions must be aware when calculating the phase of photonic crystal devices, because we only have the information of phase within the range of $(-\pi, \pi)$; and there is no information of how many $2\pi$ has already passed. In the real situation, those $2\pi$ periods are essential to determine the phase difference and we have to recover this information. One way to recover the $2\pi$ period is to first calculate one repeat pattern along the propagation direction (one geometry period along $z$ axis); and if the phase of this one geometry period is less than $2\pi$ then the phase from TMM is the "real" phase of one geometry period. For multiple geometry periods, we can simply multiply the number of geometry periods and the "real" phase of one geometry period. Please note we can not cut one geometry period into small portions to calculate the phase of each portion individually to get the phase of one geometry period. By doing so, we have destroyed the internal properties of the structure.

One other approach to get the "real" phase of arbitrary periods is to start calculate the phase from very low frequency (around *zero* normalized frequency) which correspond to very long wavelength. For very long wavelength, the phase difference between the two ends of the structure is less than $2\pi$. By increasing the frequency gradually, we can track each jump of phase which indicates the number of periods (or $2\pi$ s). Then we can obtain the "real" phase of any frequency. By the way, the phase change of a uniform medium with refractive index $n$, normalized frequency $\alpha$ and thickness $t$ (in the unit of normalized length) can be calculated as: $\varphi = k_z t = \alpha n(2\pi)t/c$ which can be used as a rough reference value for the phase.

## 7.2 Confirmation by Snell's Law

The law of refraction (Snell's Law) is a good example to confirm our idea of modeling the propagation properties by finding the phase difference through TMM. The law of refraction can be used in any interface between two uniformed medium with the mathematical form Eq. (7.2) with $n_1$ and $n_2$ the refractive index of those two uniformed medium and $\alpha_1$ and $\alpha_2$ the incident angle and refraction angle.

$$n_1 \sin\alpha_1 = n_2 \sin\alpha_2 \tag{7.2}$$

One of the simplest ways to steer the electromagnetic wave is to use an incline of dielectric material with the incline angle $\theta$ and refraction index $n_1$; and the background is air with refractive index $n_0$. Now let's suppose the electromagnetic wave incidents vertically as shown at Figure 7-1. The deflection angle is defined as the variation of refracted wave with respect to the incidence wave (shown as $\alpha$ at Figure 7-1). Given fixed incline angle $\theta$ and background refractive index $n_0$, the deflection angle $\alpha$ is a function of refractive index $n_1$. According to law of refection, we have $n_1 \sin\theta = n_0 \sin(\theta + \alpha)$; and the deflection angle $\alpha$ can be expressed as Eq. (7.3). For a set of parameter of: $n_1 = 3.0$, $n_0 = 1.0$ and $\theta = 10^0$, the deflection angle is $\alpha = 21.396^0$. Here we have the deflection angle twice as large as the incline angle. By changing the incline angle, we can reach certain range of deflection angles. But there is several shortage of this simplest design: first it is not easy to change the incline angle $\theta$ for solid inclines (high refractive index liquid may solve this problem); the transmission rate is low due to the contrast of the two mediums (i.e. strong reflection occurs at the dielectric material air interface).

$$\alpha = \sin^{-1}\left(\frac{n_1}{n_0}\sin\theta\right) - \theta \tag{7.3}$$

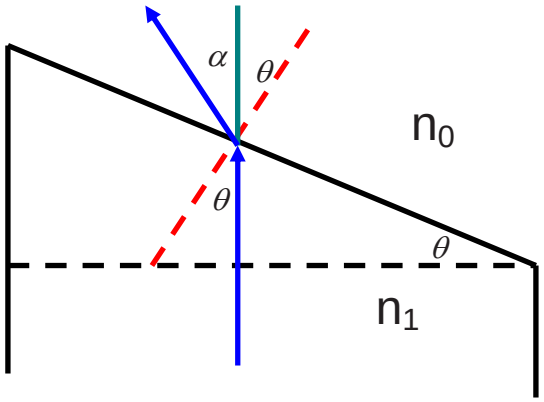


Figure 7-1: Deflection of angle of a simple incline by Law of refraction

On the other hand, we can deal the same problem by using the phase difference approach. The same structure is re-plotted at Figure 7-2 with the incline's length $L$ and height $d$. The deflection angle $\alpha$ can be expressed as $\alpha = \pi/2 - \beta - \theta$. The angle $\beta$ can be determined from the relation of wave vector $k_{AB}$ and $k_0$ which can be calculated from the phase difference (Eq. (7.4)). From Eq. (7.4), we can get the expression of $k_{AB}$ in term of $k_0$ at Eq. (7.5). Then angle $\beta$ can be found through Eq. (7.6). So $\pi/2 - \beta = \sin^{-1}(n_1 \sin\theta)$. Finally, we get the same result $\alpha = \sin^{-1}(n_1 \sin\theta) - \theta$ as the law of refraction.

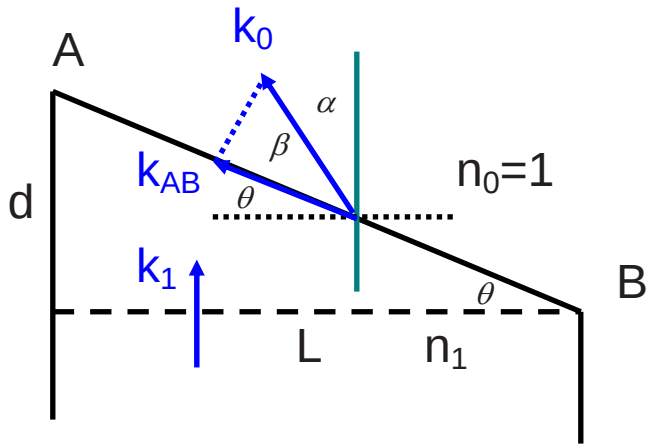


Figure 7-2: Deflection of angle of a simple incline by phase difference approach. The deflection angle $\alpha$ can be determined by the phase difference of arbitrary two horizontal locations.

$$\Delta\varphi_{AB} = k_{AB}\overline{AB}$$
$$\Delta\varphi_{AB} = k_1 d = k_0 n_1 d \tag{7.4}$$

$$k_{AB} = \frac{\Delta\varphi_{AB}}{d/\sin\theta} = k_0 n_1 \sin\theta \tag{7.5}$$

$$\beta = \cos^{-1}\left(k_{AB}/k_0\right) = \cos^{-1}\left(n_1 \sin\theta\right) \tag{7.6}$$

With the idea of phase difference, we confirm the result of the law of refraction. It is easy to calculate the phase difference in uniform medium, but this is not true for photonic crystal structures. Our TMM method can calculate the phase difference of any structures for any given frequency and in turn find the deflection angle. At the same time the transmission rate can be also figured out via TMM.

We can apply this approach to our box spring case (detail at next section) to find the phase difference between the compressed and un-compressed part and then figure out the deflection angle for certain geometry configuration.

## 7.3 Case study: box spring structures for electromagnetic wave deflection

In this section, we are going to use the concept of “phase difference” from TMM to determine the deflection angle of electromagnetic wave through a photonic crystal structure. Our purpose is to easily control the direction of electromagnetic wave propagation by adjusting the photonic crystal structure, mean while the transmission rate is still acceptable. As we mentioned in last section, the law of refraction used in two uniform medium interface is lack of flexibility to change the deflection angle and the transmission through the interface is affected by the high refractive index contrast. One advantage of the two uniform medium interface is that the response of the reflection angle is broad band (the deflection angles are

the same for any frequency if the material is non-dispersive). For photonic crystal structures, the frequency responses is usually non linear; and it may only work for a short frequency range, for example in the vicinity of band gaps. In certain application, a narrow bandwidth is still acceptable. There are several ways to control and adjust the response of photonic crystal structure, for example: mechanical, electrical or optical response. The most direct way to change the photonic crystal structure is mechanically change its shape and geometry. One candidate for such purposes is box springs which are easily modified by different comparison rates. The box spring photonic crystal has been studied by other researchers and the existence of band gap has been confirmed.[3,4]

### 7.3.1 Geometry of box spring structures

Box spring is a rather complicate photonic crystal structure. The box spring is periodic in *xy* plane and there are maybe overlaps across neighborhood springs. Figure 7-3 shows an example of overlapped 5x5 period box springs. The box spring can be compressed to achieve desired properties. The most compressed situation is the overlap of a set of box rings and the most uncompressed situation is a set of parallel rods in *xy* plane.

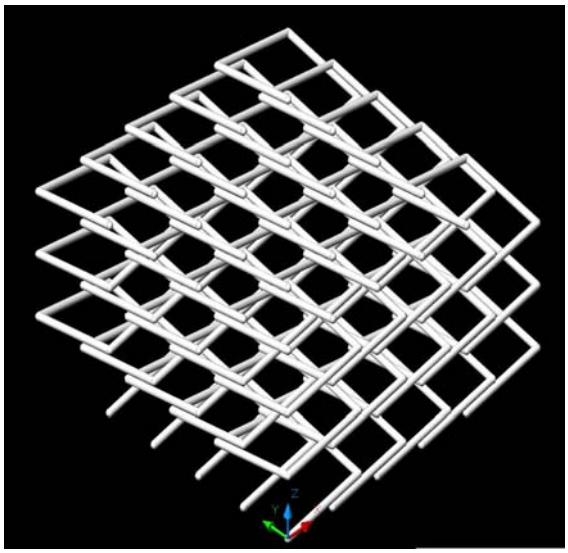

Figure 7-3: 3D view of 5x5 periods of box spring

The top view and side view of the box spring photonic crystal structure are shown at Figure 7-4. The overlap detail can be observed. Along the *z* direction there are four equivalent segments which have the same lift angle (shown at Figure 7-5) and length. Those four equivalent segments are perpendicular to each other. The lattice constant along *x* or *y* direction is the length between two neighbor rods (shown at Figure 7-5).

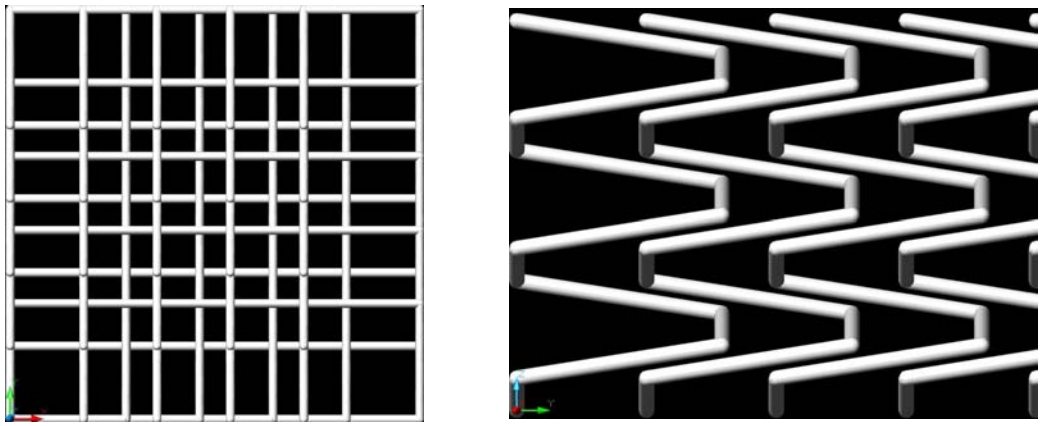


Figure 7-4: Top view (a) and side view (b) of the box spring photonic crystal structure. Overlap feature can be observed in detail. For one period along the z direction, there are four equivalent segments.

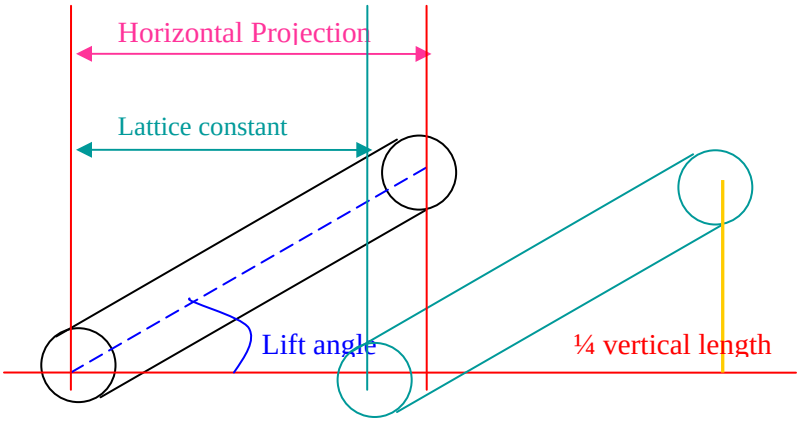


Figure 7-5: Detail of one segment along the z direction

For the calculation of uncompressed box spring photonic crystal structures, we use the following parameters: lattice constant (in plane rod to rod distant) $a$; rod length $1.6a$; rod radius $0.06a$; lift angle $8.9893^0$; refractive index of the rod material $n = 3.45$.

### 7.3.2 Simulation results of box spring structures

First, we studied the band structure of uncompressed box spring (parameters listed on the end of last section) and three cases of compressed box spring with the $C/C_0$ ratio 0.02, 0.04 and 0.06 where $C$ is the length of one period compressed box spring along $z$ direction and $C_0$ is the length of one period uncompressed box spring along $z$ direction. The band structures of all four cases are plotted at Figure 7-6.

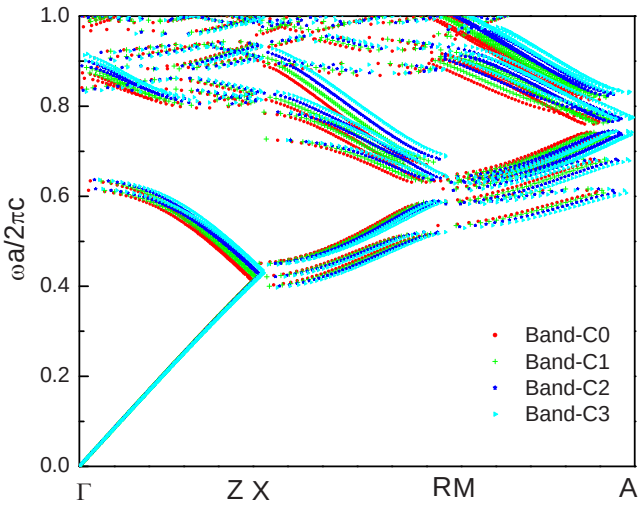


Figure 7-6: Band structure for uncompressed and compressed box spring photonic crystals.

With the information of each case (uncompressed and compressed), we can study the relation between deflection angle ($\beta$) and compressed angle ($\theta$) based on the illustration of Figure 7-7. The left side is the uncompressed box spring and right ride is the compressed box spring with compression ration $C/C_0$ and the box spring is compressed gradually between the left

side and right side and form an incline. The length between the left and right box spring is set to $a$ and the vertical length is 5 periods.

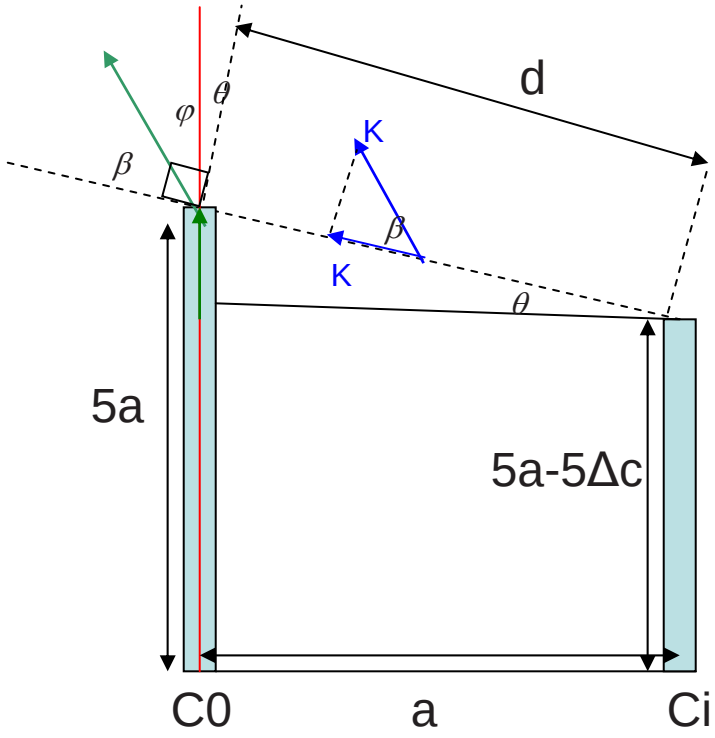


Figure 7-7: Illustration of how to deflect electromagnetic wave through uncompressed and compressed box spring photonic crystal.

Then we apply the strategy develop at section 7.2 to get the deflection angle by phase difference at left and right side. Here, we assume we can calculate the phase for each box spring individually without the interaction across neighborhood box springs and then get the phase difference of left and right side.

We first calculate the phase for the uncompressed box spring (left side) and then calculate the phase of the compressed box spring (right side). Then the phase difference is obtained just like the procedure to confirm the Snell's Law (Eq. (7.7) with $\alpha = ka/2\pi$ the normalized frequency).

$$\varphi = \frac{\pi}{2} - \beta - \theta$$

$$\theta = \tan^{-1}\left(\frac{5a - 5(a - \Delta c)}{a}\right) = \tan^{-1}\left(\frac{5\Delta c}{a}\right)$$

$$\Delta\phi = \phi_0 - \phi_i, k_p d = \Delta\phi, so\ k_p = \frac{\Delta\phi}{d},\ d = \frac{a}{\cos\theta},\ k = \alpha\frac{2\pi}{a} \quad (7.7)$$

$$\beta = \cos^{-1}\left(\frac{k_p}{k}\right) = \cos^{-1}\left(\frac{\Delta\phi/d}{\alpha\cdot 2\pi/a}\right) = \cos^{-1}\left(\frac{\Delta\phi\cdot\cos\theta/(a)}{\alpha\cdot 2\pi/a}\right)$$

$$= \cos^{-1}\left(\frac{\Delta\phi\cdot\cos\theta}{\alpha\cdot 2\pi}\right)$$

After the phase difference obtained by TMM, we can get the relationship of deflection angle for different normalized frequency at fixed compression ratio. The result of compression ration 0.06 at right side is shown at Figure 7-8 (in this result, the distance between the uncompressed and compressed spring is one lattice constant). The deflection angle is oscillating and remains small for a large frequency range below the first band gap. But very large deflection angle can be achieved at the vicinity of first band gap (Figure 7-9); at the same time the transmission rate is still acceptable (Figure 7-10): at normalized frequency $a/\lambda = 0.60725$, the deflection angle is $16.6^0$ and the transmission of both uncompressed and compressed box spring is around 70%.

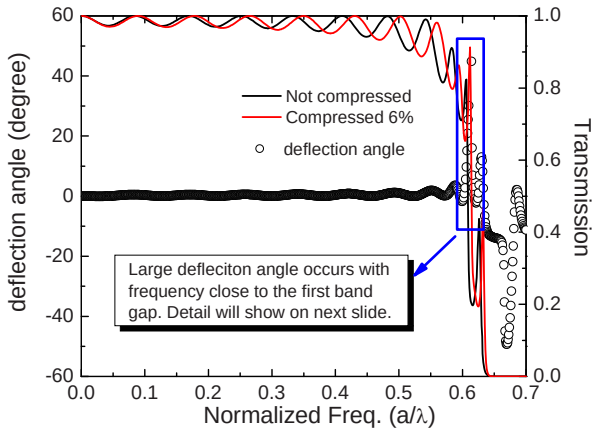


Figure 7-8: Deflection angle for all frequency with transmission for both uncompressed and compressed case.

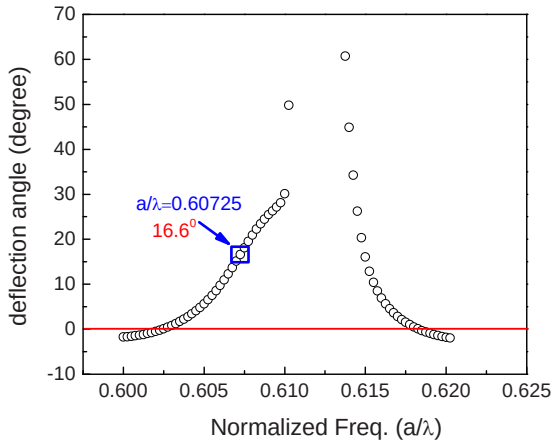


Figure 7-9: Detailed deflection angle at the vicinity of first band gap

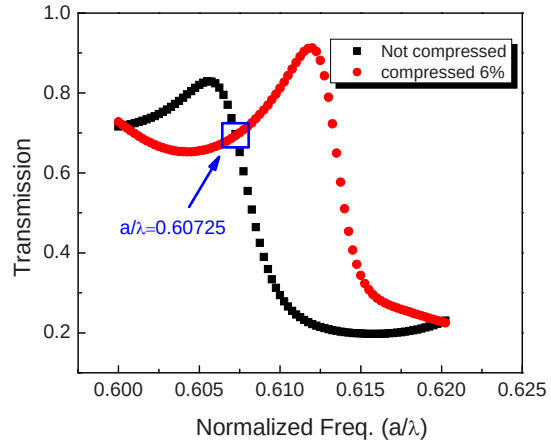


Figure 7-10: Detailed transmission at the vicinity of first band gap

The non-linear effect at the photonic band edge makes possible the large deflection angle. But the bandwidth for this large deflection angle is quite small. The deflection angle can be positive (deflected to the left) or negative (deflected to the right) which corresponds to normal refraction and negative refraction respectively. In this example, although we have found the deflection angle and transmission rate as functions of normalized frequency, the design of device of certain function is far from completed. Optimization is needed to get large bandwidth and more flexible deflection angle responses. But the idea of analyzing

phase at the position of *xy* plane from TMM can be generalized and applied to future device design and simulation.

**References:**


1. M. Born and E. Wolf, *Principles of Optics*, 7th edition, Cambridge University Press, 1999
2. http://www.usa.canon.com/consumer/controller?act=CanonAdvantageTopicDtlAct&id=2632 webpage accessed October 2007
3. O. Toader and S. John, "Square spiral photonic crystals: Robust architecture for microfabrication of materials with large three-dimensional photonic band gaps", *Phys. Rev. E* **66**, 016610 (2002)
4. O. Toader and S. John, "Proposed Square Spiral Microfabrication Architecture for Large Three-Dimensional Photonic Band Gap Crystals", *Science*, **292**, (2001)

# Chapter 8. TMM algorithm with active gain material extension

Photonic crystal cavity has been long proposed to be a good candidate for low-threshold laser, while current available numerical methods based on rate equations are not efficient and not accurate for simulation such small scale devices and for situations well above the threshold. Our previous chapters discussed the planewave based transfer (scattering) matrix method (TMM) mainly focus on passive material and the simulation results such as spectra, mode profiles for cavity embedded photonic crystal are only valid for “cold cavity”. However, our TMM algorithm is not limited to the passive material only; in this chapter detailed algorithm extension with capability for direct modeling active gain material is included along with several simulated active photonic crystal devices. The major advantage of Gain material TMM (GTMM) is to provide more precise lasing spectra, mode shape information and light-current (L-I) curve due to the fact that optical solution in GTMM is obtained in “hot cavity” condition which is self-consistent with laser pumping intensity. Eventually, GTMM can be used to solve complex 3D photonic crystal laser and light emitting diode (LED) structures.

## 8.1 Rate equation, the starting point

Rate equation is the fundamental simulation technique used in laser and LED device design which connects the electric property and optical property together by a set of differential equations. The gain medium layer is typically embedded in the middle of the structure; Figure 8-1 shows a schematic picture of a diode laser. The middle gain layer has width $w$, thickness $d$, length $L$, and a refractive index higher than the top and bottom layers, supporting a guiding mode with average width of $d/\Gamma$. When a current with density of J is injected downward, the middle layer can present a gain factor $g$ to amplify light.[1,2,3]

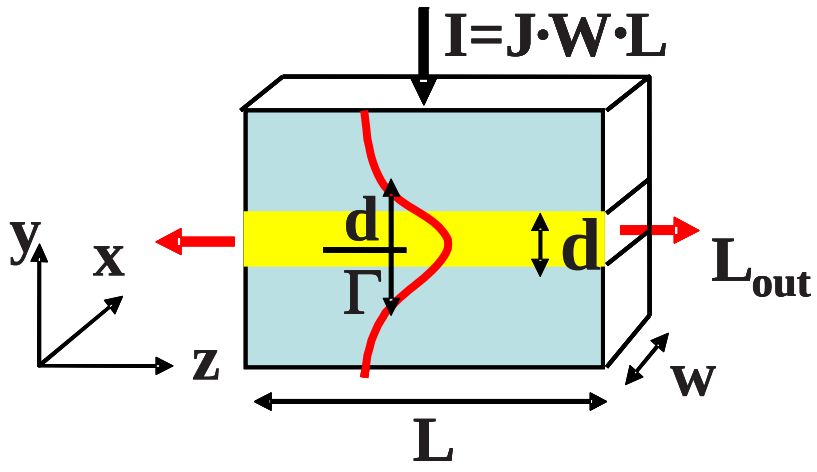


Figure 8-1: Schematic of a photonic crystal laser

To simplify the derivation and show the main idea of how rate equation works, we use the simple mode rate equation (Eq. (8.1)) with quantum dot gain relation (Eq. (8.2)) with the average carrier density $N$, the average photon density $P$, and gain factor $g$. The inject current $I$ and the light output $L_{out}$ are given by Eq. (8.3). The physical meanings of $\eta_i, q, \tau, v_g, \alpha_c, A_0, N_0$ etc. are listed and explained at Table 8-1 with a set of typical values of a diode laser.

$$\frac{dN}{dt} = \frac{\eta_i \cdot J}{q \cdot d} - \tau^{-1} N - \upsilon_g \cdot g \cdot P$$
$$\frac{dP}{dt} = \frac{\Gamma \cdot N \cdot \beta}{\tau_s} + \upsilon_g \cdot (\Gamma \cdot g - \alpha_c) \cdot P \qquad (8.1)$$

$$g = A_0 \cdot (N - N_0) \qquad (8.2)$$

$$I = J \cdot w \cdot L$$
$$L_{out} = P \cdot E_p \Gamma^{-1} V_c \cdot \tau_p^{-1} \qquad (8.3)$$

$$\frac{dN}{dt} = \frac{dP}{dt} = 0 \qquad (8.4)$$

Table 8-1: Physical meanings of parameters in rate equation with typical numerical values for a diode laser

| Physical meaning | | Typical numerical values |
|---|---|---|
| Vacuum speed of light: | c | $3\times10^{10}$ cm/s |
| Single electron charge: | q | $1.6\times10^{-19}$C |
| Plank's constant: | h | $6.625\times10^{-34}$ J·s |
| Differential gain: | $A_0$ | $2.5\times10^{-16}$ $cm^2$ |
| Transparent carrier density: | $N_0$ | $4.5\times10^{17}$ $cm^{-3}$ |
| Optical group index: | $n_g$ | 3.5 |
| Effective velocity: | $v_g$ | $v_g = c/n_g$ |
| Facet reflectivity: | $R_1$, $R_2$ | $R_1= R_2 = (n_g -1)^2 (n_g +1)^{-2}$ |
| Absorption loss: | $\alpha_0$ | 20 $cm^{-1}$ |
| Facet loss: | $\alpha_r$ | $\alpha_r = (1/2L)Ln[1/(R_1R_2)]$ |
| Total optical loss: | $\alpha_c$ | $\alpha_c =\alpha_r+\alpha_0$ |
| Carrier spontaneous emission lifetime: | $\tau_s$ | $3\times10^{-9}$ s |
| Carrier non-radioactive decay lifetime: | $\tau_{nr}$ | $3\times10^{-6}$ s |
| Total carrier lifetime: | $\tau$ | $\tau =(\tau_s^{-1}+ \tau_{nr}^{-1})^{-1}$ |
| Photon out-coupling lifetime: | $\tau_p$ | $\tau_p=1/( v_g \alpha_r)$ |
| Lasing wavelength in vacuum: | $\lambda_0$ | $1.3\times10^{-4}$ cm |
| Thickness of active layer: | d | $2.0\times10^{-5}$ cm |
| Frequency: | $\nu$ | $\nu = c/\lambda_0$ |
| Single photon energy: | $E_p$ | $E_p = h\nu = hc/\lambda_0$ |
| Confinement factor: | $\Gamma$ | 0.5 |
| Spontaneous emission factor: | $\beta$ | $1\times10^{-4}$ |
| Cavity width: | w | $5\times10^{-4}$ cm |
| Cavity length: | L | 0.025 cm |
| Cavity active volume: | $V_c$ | d×w×L |

At the steady state (i.e. the constant wave output with a single lasing frequency), the average carrier density and average photon density for fixed inject currents should not change (Eq. (8.4)). For a given inject current, the steady state quantities can be obtained from Eq. (8.1) to Eq. (8.4). With large inject current approximation ( $g \approx \alpha_c \Gamma^{-1}$ ), the results are expressed at Eq. (8.5).

$$
\begin{aligned}
&L_{out} \approx \frac{E_p \eta_i \alpha_r}{q \alpha_c} (I - I_{th}) \\
&I_{th} = \left( \alpha_c \Gamma^{-1} A_0^{-1} + N_0 \right) \cdot q \cdot V_c \cdot \eta_i^{-1} \cdot \tau^{-1} \\
&\frac{dL_{out}}{dI} = \frac{E_p \eta_i \alpha_r}{q \alpha_c}
\end{aligned}
\qquad (8.5)
$$

The first equation of Eq. (8.5) indicates there is a lasing threshold, and the third equation of Eq. (8.5) indicates one additional carrier will generate $\eta_i \alpha_r / \alpha_c$ photon when the inject current is above the threshold. The plot of the first equation of Eq. (8.5) illustrates the relation between the output light intensity (in unit of Watt) and input current (in Ampere) which is usually called the L-I curve.

## 8.2 Defining the electric field dependent dielectric constant for gain material

In the single mode rate equation algorithm (section 8.1), the second equation of Eq. (8.1) is used to describe the light in the cavity by using averaged parameters $\alpha_c$ and $\Gamma$. Those two parameters are difficult to define if the gain material has complex structure and the dimension of the cavity is comparable with lasing wavelength (such as 2D PC slab cavity laser and 3D photonic crystal laser). Even if the definitions of averaged parameters are given, the calculations can only be performed for the cold cavity case without gain (i.e. below the threshold).

To avoid the difficulties, we will not use the second equation of Eq. (8.1) with averaged parameters to describe the light in laser cavity. Instead, we will use rigorous GTMM formulism and electric field dependent dielectric constant for gain materials. The dielectric constant of gain material can be written as Eq. (8.6) with $\varepsilon_{ini}$ the dielectric constant when the electric field at the gain material is zero.

$$\varepsilon = (\sqrt{\varepsilon_{ini}} - i\frac{c}{2\omega}g)^2 \tag{8.6}$$

With the first equation of Eq. (8.1), Eq. (8.2) and Eq. (8.4), we can express the average carrier density and gain factor in Eq. (8.7). With photon density $P$ in term of electric field and single photon energy (Eq. (8.8)), the gain factor can be further rewritten as Eq. (8.9).

$$\begin{aligned} N &= \frac{\eta_i \tau q^{-1} d^{-1} J + A_0 \tau \upsilon_g P N_0}{1 + A_0 \tau \upsilon_g P} \\ g &= \frac{A_0(\eta_i \tau q^{-1} d^{-1} J - N_0)}{1 + A_0 \tau \upsilon_g P} \end{aligned} \tag{8.7}$$

$$P = \frac{1}{2}\varepsilon |E|^2 / E_p \tag{8.8}$$

$$\begin{aligned} g &= \frac{g_0}{1 + a|E|^2} \\ g_0 &= A_0 \eta_i \tau J/(qd) - A_0 N_0 \\ a &= A_0 \tau \upsilon_g \varepsilon/(2E_p) \end{aligned} \tag{8.9}$$

To consider the spontaneous emission, the second equation of Eq. (8.1) is rewritten as Eq. (8.10), and the gain factor with spontaneous emission can be expressed as Eq. (8.11). It should be mentioned that the spontaneous emission factor $\beta$ is the coupling factor between the total emission of dipole and the lasing cavity mode and depends on the exact coordinates and polarization of dipole. Spatially dependent $\beta$ should be used if we would like to know

the exact behavior below the lasing threshold. But for simplicity, we will use an averaged $\beta$ for the gain materials.

$$\begin{aligned} \frac{dP}{dt} &= \upsilon_g \cdot \left(\Gamma \cdot g' - \alpha_c\right) \cdot P \\ g' &= g + \frac{\beta}{\upsilon_g \tau_s P} N \end{aligned} \tag{8.10}$$

$$\begin{aligned} g' &= \frac{g_0}{1 + a|E|^2} + \beta \frac{b_1 + b_2 |E|^2}{|E|^2 (1 + a|E|^2)} \\ b_1 &= 2E_p \eta_i \tau J / (\tau_s q d \upsilon_g \varepsilon) \\ b_2 &= A_0 N_0 \tau / \tau_s \end{aligned} \tag{8.11}$$

## 8.3 Gain-TMM algorithm for laser device simulation

In last section, we have expressed the dielectric constant of gain medium and gain factor in term of electric field intensity. Various photonic crystal lasers have been proposed recently.[4,5,6,7,8] Now in this section the gain transfer (scattering) matrix algorithm (GTMM) is presented with iterations to simulate laser devices.

Same as the TMM algorithm assumed, periodic boundary condition is applied to the $XY$ plane and the planewave in defined as the usual way. We use $N_p \times 1$ vector $A_i$ and $B_i$ to represent the electric field Fourier coefficient at each slice $i$, and from our previous chapters the outgoing waves can be obtained from the incidence wave by the scattering matrix $S$ as expressed at Eq. (8.12). The schematic of GTMM structure is presented at Figure 8-2. The lasing status is when there is no light input while there is still continues light output.

$$\begin{pmatrix} A_{n+1} \\ B_0 \end{pmatrix} = S \begin{pmatrix} A_0 \\ B_{n+1} \end{pmatrix} \tag{8.12}$$

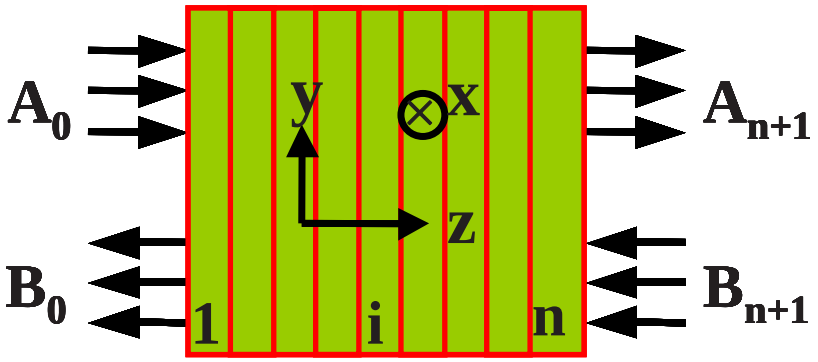


Figure 8-2: Schematic of Gain-TMM with the whole photonic crystal structure divided into n slices and the outgoing planewaves are found by the S matrix and incidence planewaves.

Mathematically to simulate a laser problem, we set $A_0 = (A_0^{(1)}, 0, \cdots, 0)$ and $B_{n+1} = (0, \cdots, 0)$ solving $A_0^{(1)}$ for a given output $L_{out,right}$ by Eq. (8.13) where $p_j = 0$ for all evanescent waves. When $A_0^{(1)}$ is obtained, we can use the TMM algorithm to calculate the field distribution. With the calculated field distribution, the new dielectric constant for gain medium can be obtained through Eq. (8.6). In turn, with the updated dielectric constant of gain medium a new $S$ matrix can be found. With the new $S$ matrix, a new $A_0^{(1)}$ can be obtained.

$$L_{out,right} = \sum_{j=1}^{M} p_j \, | A_{n+1}^{(j)} |^2$$
$$A_{n+1}^{(j)} = A_0^{(1)} S_{j1} \qquad (8.13)$$

Repeat the iteration, until the steady $A_0^{(1)}$ is finally achieved for given inject current $I$ and output power $L_{out,right}$. Then we will calculate $A_0^{(1)}$, the incident planewave, for various $L_{out,right}$ and incident frequencies. When the inject current is above threshold ($I > I_{th}$), a zero $A_0^{(1)}$ can be found for non-zero $L_{out,right}$ at certain incident frequency which indicates a steady finite light output exists for zero input light or lasing. The frequency where a zero $A_0^{(1)}$ is found is the lasing frequency and the light output power for certain current makes the L-I curve. The detailed procedures will be illustrated through an example of 1D DBR laser at next section.

## 8.4 1D DBR laser, an example of GTMM application

The multilayer 1D DBR cavity structure is illustrated at Figure 8-3. Based on the mentioned parameters at the figure caption, there will be a resonant mode at $0.98\mu m$ which is obtained from TMM spectrum calculation and the results are also shown at Figure 8-3.

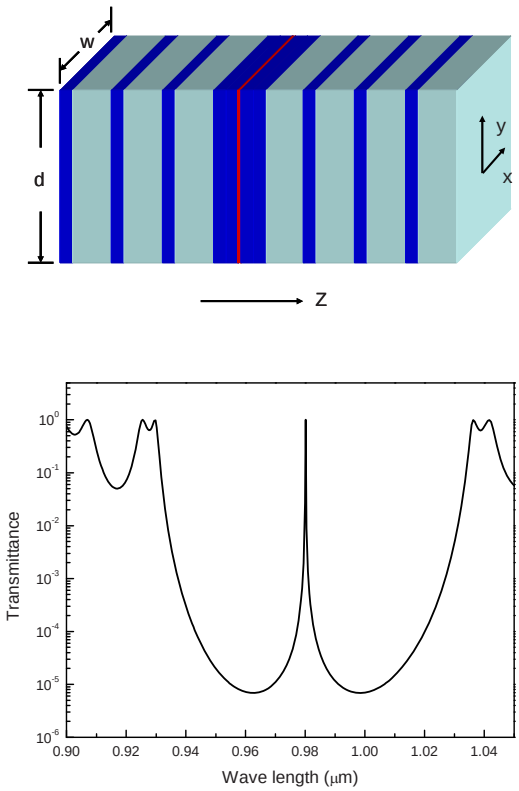


Figure 8-3: Schematic of 1D DBR laser with a multilayer structure $(AB)_{24}EGE(BA)_{24}$, where G is the Gain material layer. The refractive indices and the layer thicknesses are as following: $n_{A,E,G} = 3.526$ , $n_B = 3.077$ , and $d_A = 64.49nm$ $d_B = 79.63nm$ , $d_E = 137.78nm$ , $d_G = 2nm$ . The transition rate shows a single resonant peak at $0.98\mu m$ .

As mentioned at last section, for fixed incident frequency and light output with the presence of active gain material inside the structure, the required light input can be obtained through the iteration process until a steady light input value is reached. By varying the light output

value with fixed inject current and incident frequency, the light output vs. light input graph can be obtained. Three light output vs. light input relations are plotted at Figure 8-4: basically there are two saddle points for each curves. Above threshold the saddle point located at the larger light output region reaches zero which corresponds to lasing, while below threshold, the saddle point located at the smaller light output region reaches zero which corresponds to spontaneous emission, and just at the threshold those two saddle points come together and reaches zero at lasing frequency. For light output vs. light input relations, if the incident frequency is not the lasing frequency, neither of those two saddle points reaches zero, i.e. no lasing or spontaneous emission are found.

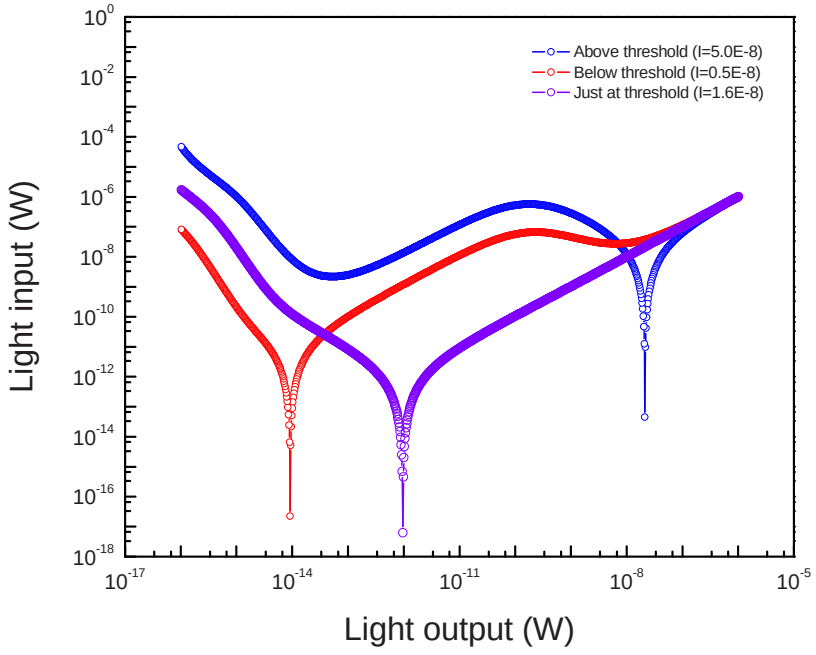


Figure 8-4: Light input vs. light out graph at lasing frequency for three different inject currents: above threshold, below threshold, and just at threshold.

For each inject current, by iteration for various incident frequencies, eventually there will a saddle point reaches zero which corresponds one (light output, current) point located at the L-I curve. When the inject current is above threshold, it is lasing case, otherwise it is a

spontaneous case. The light output intensity is several orders larger at lasing case than the spontaneous emission. The L-I curve of the 1D DBR laser is illustrated at Figure 8-5.

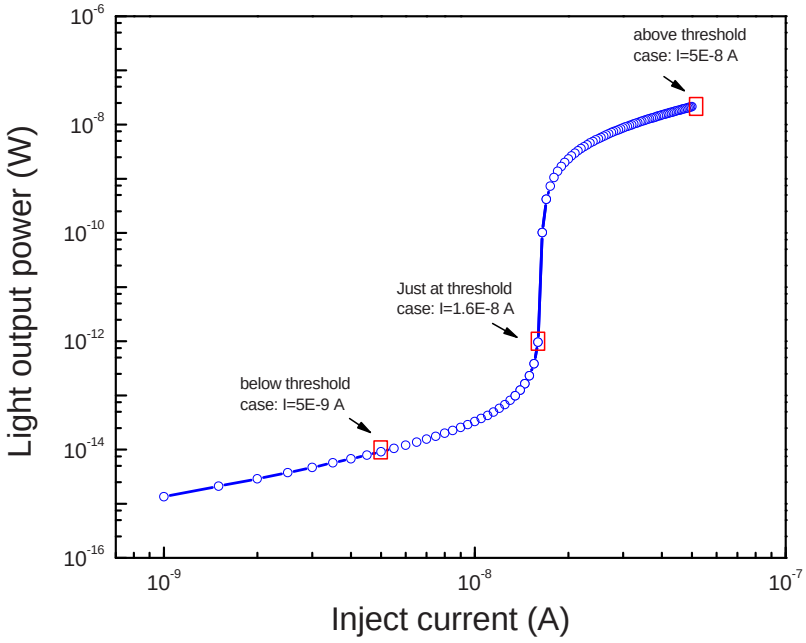


Figure 8-5: Light output power vs. inject current (L-I curve) for 1D DBR laser. Three typical inject currents are selected to show the difference across above threshold, below threshold and just at threshold with corresponding light input vs. light out graphs shown at Figure 8-4.

The lasing frequency is found to be almost the same as the resonant frequency of passive cavity with little dependence on inject currents. This is reasonable because of the small thickness of the gain medium layer and the small change of the dielectric constant of the gain medium (for the 1D DBR case, the imaginary part of dielectric constant is only around -0.23). But to show the little difference of lasing frequency, the 1D DBR lasing frequency for various inject currents are present at Figure 8-6.

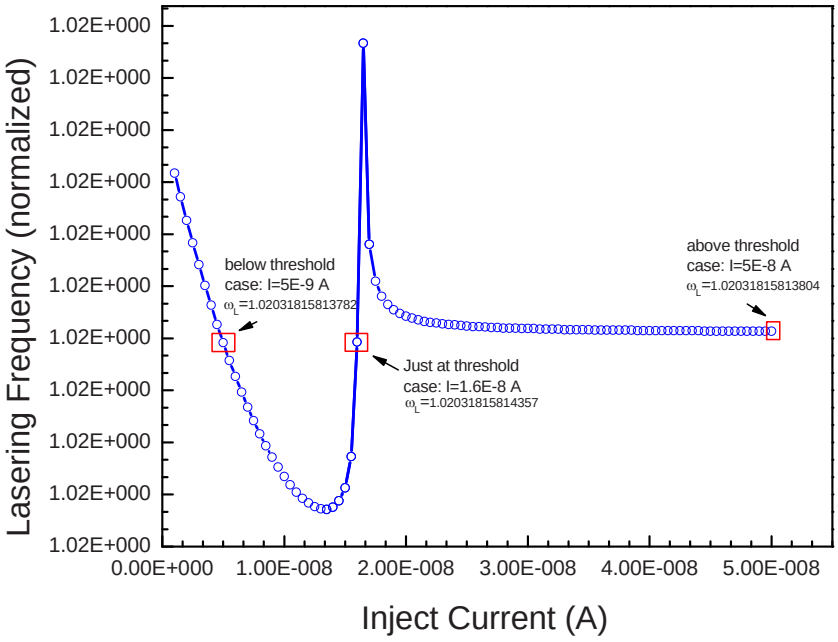


Figure 8-6: Lasing frequency for various inject current, here $\omega_L$ is in unit of normalized frequency: $1\mu m/\lambda$

## 8.5 3D woodpile photonic crystal laser, an example of GTMM application

To test the performance and the capacity of GTMM, we applied it to a 3D photonic crystal laser. The gain medium is located at the center of the cavity layer embedded in the classical layer-by-layer woodpile photonic crystal structure. The cross sections of 3-by-3 super cell of the woodpile structure are illustrated at Figure 8-7 (a) with the gain medium layer has the same geometry as the cavity layer. From the TMM spectra results, there are two resonant modes (for the passive cavity) inside the band gap from two different polarizations (shown on Figure 8-7 (b)). We are going to focus on the x-polarization mode which has resonant frequency $980nm$ with $Q$ value around 18000 and transmittance around 5%.

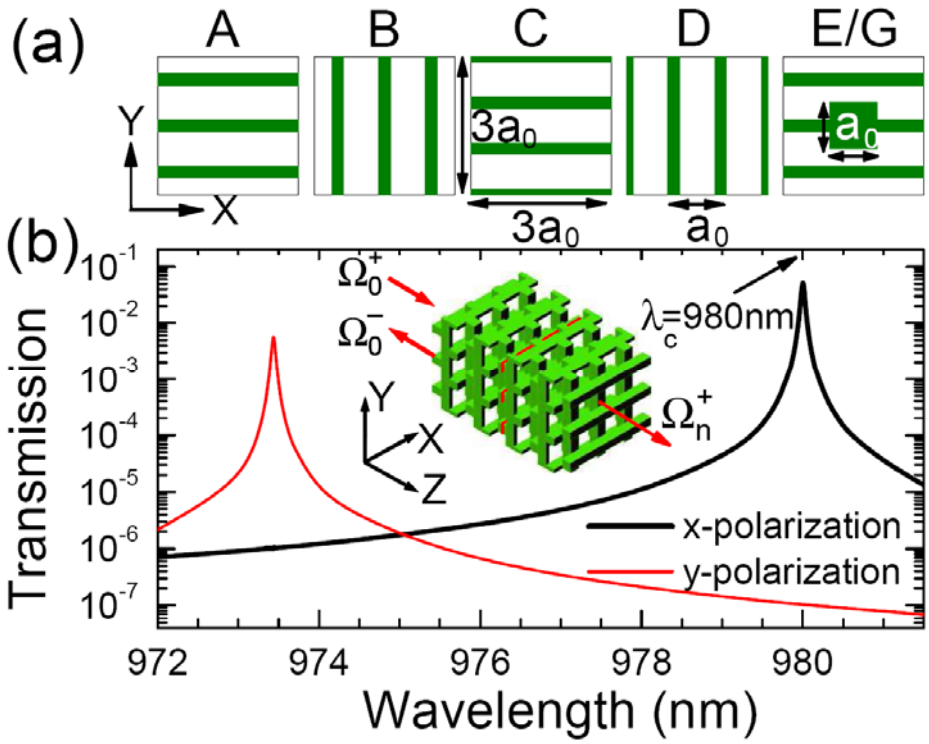


Figure 8-7: (a) Cross sections of the 3D woodpile photonic crystal laser $(ABCD)_2EGE(BCDA)_2$ composed of rectangular dielectric rods in air, where G is the gain medium layer. The structure has a periodicity of $3a_0$ along both X and Y directions, where $a_0 = 436.5\ \text{nm}$ . The rods have thickness $d_{A,B,C,D} = 0.3a_0$ , $d_G = 2nm$ , $d_E = 64.48\ \text{nm}$ and width $w = 0.25a_0$ , and refractive index of 3.526. (b) Transmission spectra for normal incidence of two polarized. The insect shows the photonic crystal laser structure with red layer the gain medium layer.

With the assumption of uniform pumping current in the gain medium, the total lasing output and lasing frequency can be found for different inject currents and the results are shown at Figure 8-8 (a). Above threshold, the “hot cavity” electric field mode profile shows strong spatial dependence which in turn causes the strong spatial hole burning effects of non-uniform imaginary part of gain material dielectric constant and non-uniform gain factor at different locations of the gain medium layer (Figure 8-8 (b)). Due to the large change of imaginary part of dielectric constant at gain medium layer, the deviation of lasing frequency form the passive cavity resonant frequency is large and strongly depends on the inject current.

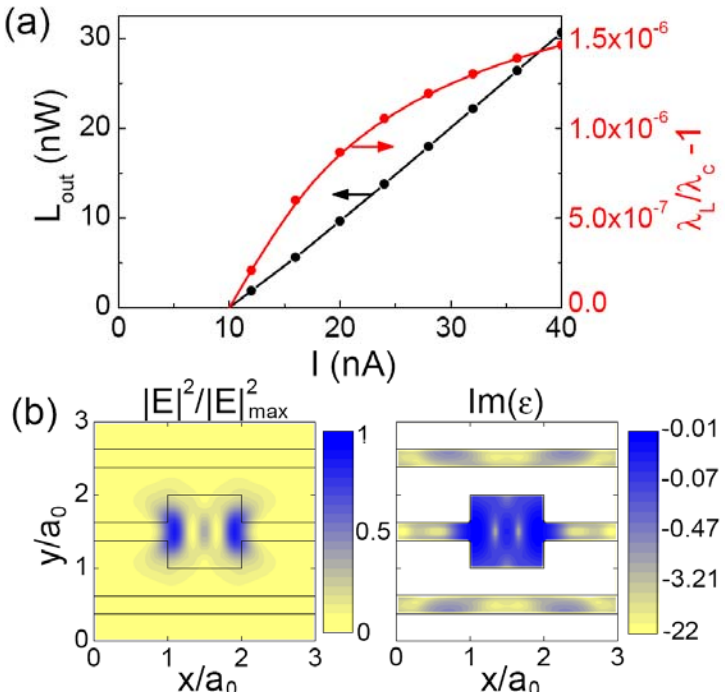


Figure 8-8: (a) light output power vs. inject current (L-I curve) of 3D woodpile laser; (b) electric field distribution and imaginary part of dielectric constant inside the gain medium layer when lasing at inject current 40nA.

The L-I curve, lasing mode profile and lasing frequency chirping effect can be calculated from the gain material transfer (scattering) matrix method. The 1D DBR laser case confirms the accuracy of GTMM and the 3D woodpile laser case shows the power of GTMM. In the future, the GTMM algorithm can be applied efficiently and accurately to simulate and design future photonic crystal laser devices.

**References:**

1. L.A. Coldren and S.W. Corzine, *Diode Lasers and Photonic Integrated Circuites*, John Wiley and Sons, New York, 1995
2. A. Yariv, *Quantum Electronic*s, John Wiley and Sons, New York, 1989

3. J. Piprek, *Optoelectronic Devices: Advanced Simulation and Analysis*, Springer, Berlin, 2005
4. O. Painter, R.K. Lee, A. Scherer, et al, "Two-dimensional photonic band-gap defect mode laser", *Science*, **284**, 1999
5. H.G. Park, S.H. Kim, S.H. Kwon, et al, "Electrically driven single-cell photonic crystal laser", *Science*, **305**, 2004
6. H. Altug H, J. Vuckovic, "Photonic crystal nanocavity array laser", *Optics Express*, **13**, 2004
7. S. Strauf, K. Hennessy, M.T. Rakher, et al, "Self-tuned quantum dot gain in photonic crystal lasers", *Phys. Rev. Lett.* **96**, 127404, 2006
8. M. Soljacic, J.D. Joannopoulos, "Enhancement of nonlinear effects using photonic crystals", *Nature Materials*, **3**, 212 2004

# Chapter 9. Microwave experiments for woodpile photonic crystal cavities

Photonic crystal devices for visible light or infrared are usually difficult to fabricate due to the small size and complex procedures. But structures at microwave region are large enough for easy design, fabrication and measurement. One important property for photonic crystal is scaling: the phenomenon at different length scale are the same.[1] So we can take advantage of the easy manipulation aspect at large scale to design, fabricate and measure the response of photonic crystals working at microwave region, and then extend our knowledge to small length scale domains. In this chapter, resonant cavities embedded in the woodpile layer-by-layer photonic crystal structures[2,3,4] are systematically studied at the microwave region.

## 9.1 Instrument setup for microwave experiments

The photonic crystals at microwave region we studied are 3D layer-by-layer woodpile structures with square cross-section dielectric rods made of pure alumina.[5,6,7] These rods (measured refractive index around 3.0) are commercially available and have a width of 0.32cm. The dimensions of the whole crystal are 15.24cm by 30.48cm in width and length with height determined by the number of layers of dielectric rods stacked on top of each other (shown at Figure 9-1 (a)).

We define the $XY$ plane as the plane of each layer in this structure. The stacking sequence repeats every four layers, corresponding to a single unit cell in the stacking direction. The center-to-center spacing between rods is 1.07 cm, giving a filling ratio of 30%. The defect cavity was located in the layer that was almost equally clad above and below in the $Z$ direction. The cavity size is measured in term of $d/a$ ratio where $d$ is the length of rod

removed to form the cavity and $a$ is the center-to-center spacing between adjacent rods (Figure 9-1 (b)). If the structure had 15 layers stacked on top of each other then the defect was made in the 8th layer, we will call it the 7-1-7 configuration.

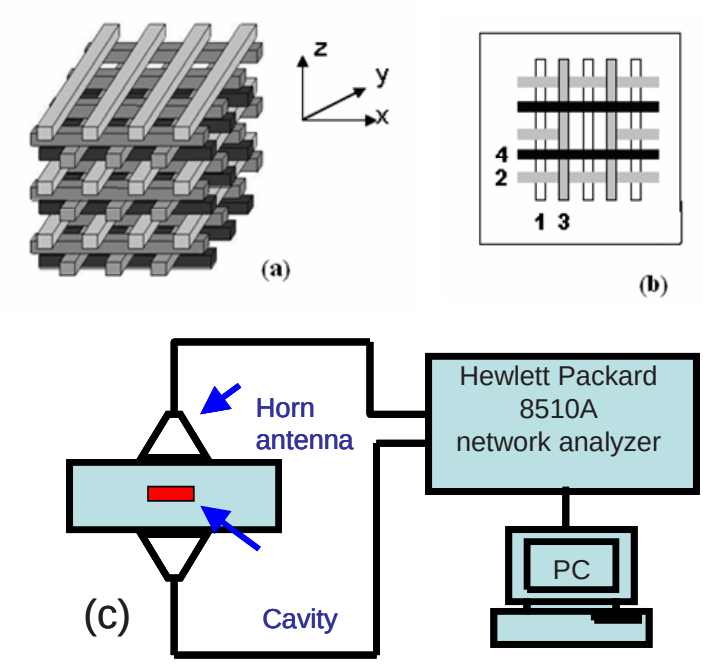


Figure 9-1: (a) Shows the design of three dimensional photonic crystal; (b) Illustrates the defect layer, the removed part has a width $d$ and center to center spacing between rods is $a$;(c) is the experimental setup.

Transmission properties are measured by a Hewlett Packard 8510A network analyzer with standard gain horn antennas to transmit and receive electromagnetic radiation. Figure 9-1 (c) shows the experimental setup. The electric field is polarized in the $XY$ plane for all these measurements. Only $X$ -axis polarized electric field has the resonant feature while $Y$ -axis polarized electric field does not have any resonant mode which is consistent with the TMM calculation result. The loss in the cables and the horns was normalized by calibrating all measurements up to the ends of the horn antennas. The Q value is determined for all the configurations using measured values of peak frequency and full width half maxima (-3dB) points, i.e. $Q = f_{peak} / \Delta f$ .

## 9.2 Resonant frequency and Q value for fixed length cavity

The woodpile photonic crystal with the parameter defined at section 9.1 has directional band gap between around 11 GHz to around 15 GHz. With the introduction of cavity with size $d/a=1$, both microwave experiments and TMM calculation confirmed there will be a resonant mode around frequency 12.3GHz with $X$ -axis polarized incident planewave. Figure 9-2 shows the spectrum of pure woodpile crystal and the resonant peak for 9-1-8 configuration.

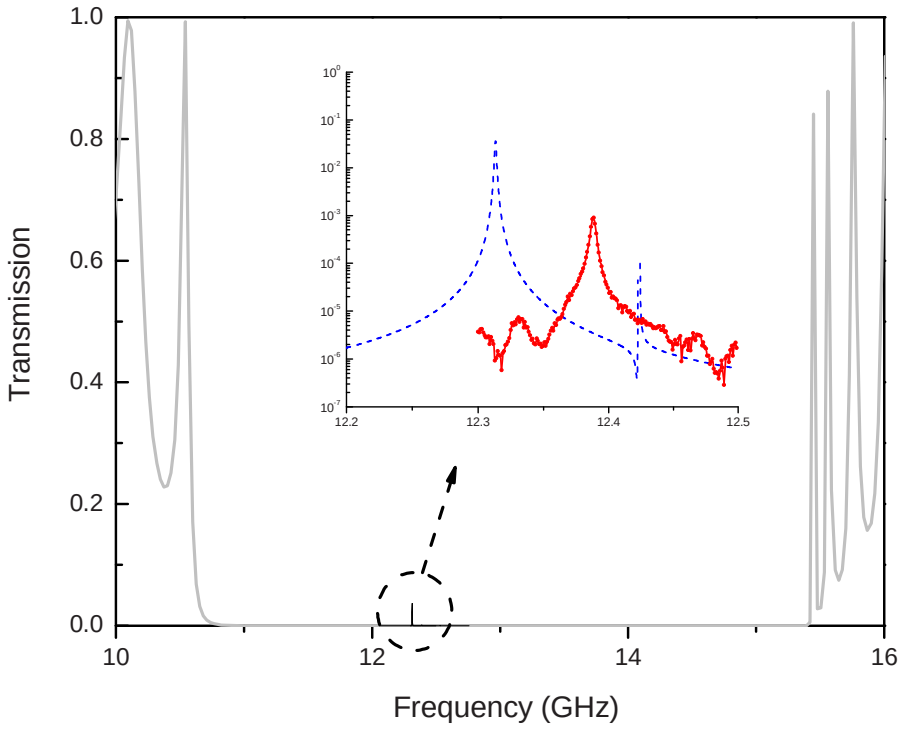


Figure 9-2: The spectrum of 9-1-8 structure as an example: the gray line is the transmission for the perfect photonic crystal with directional band gap between around 11GHz and around 15GHz; the red line is the experimental result and the dashed blue line is the TMM computation result. The inset is the zoom in view of the resonant peaks.

Now we study the trends when the number of cladding layers above and below the cavity layer changes. The resonant frequency increases slightly when stacking layers are increased from 10 to 14 and oscillates and approaches to constant at higher number of stacking layers. The difference between the frequencies is so small that the experimental setup can not give us consistent results on resonant peak values for those configurations over 18 layers. There is a systematic lower resonant frequencies in the calculation compared with experiment (Figure 9-3) which is due to the uncertainty of the refractive index of the rods. In the calculation, the refractive index is set exactly as 3.0, while the refractive index of the alumina rods is measured to be close to 3.0 with uncertainty $\pm 0.1$. A slightly change in the refractive index will result in substantial change in the resonant peak frequency from TMM calculation.

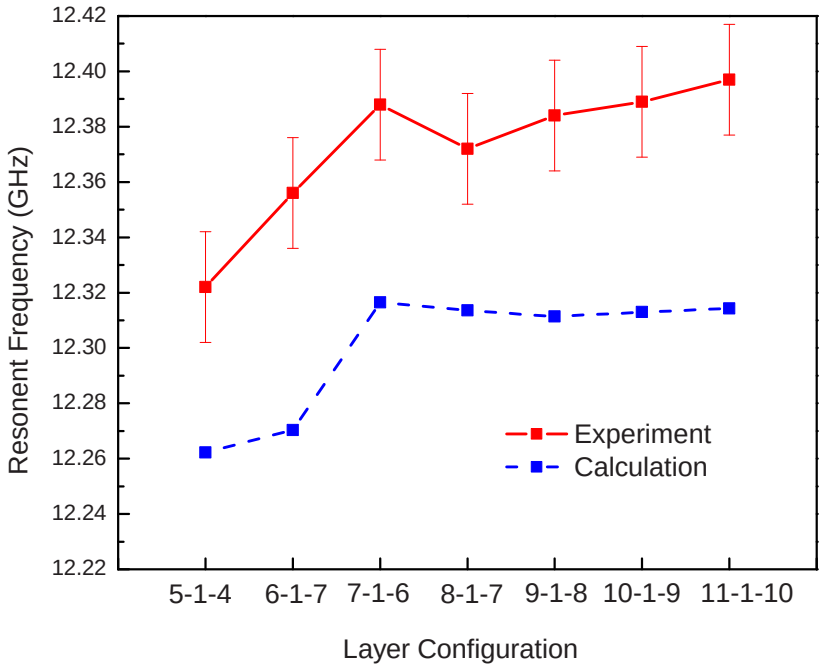


Figure 9-3: Trends of resonant frequencies found experimentally (red solid lines with error bar) and calculated numerically using TMM (blue dotted lines). Resonant frequencies increase slightly and then oscillate approaching to a constant as stacking layers in z-direction increase.

Both experiments and TMM calculations show an exponential increase of $Q$ value when the number of cladding layers increases. The largest overall $Q$ value of 6190 is measured at the 22-layered crystal from experiments, and around 16000 for TMM calculations. The measured $Q$ values are much lower than the calculated $Q$ values. One main reason is the effect of loss in the lateral direction since the cavity is confined by only 6 lattice constants on width and 12 lattice constants in length. This loss is not present in TMM calculation as it considers an infinite photonic crystal in the lateral direction with periodic defects in the super cell lattice.

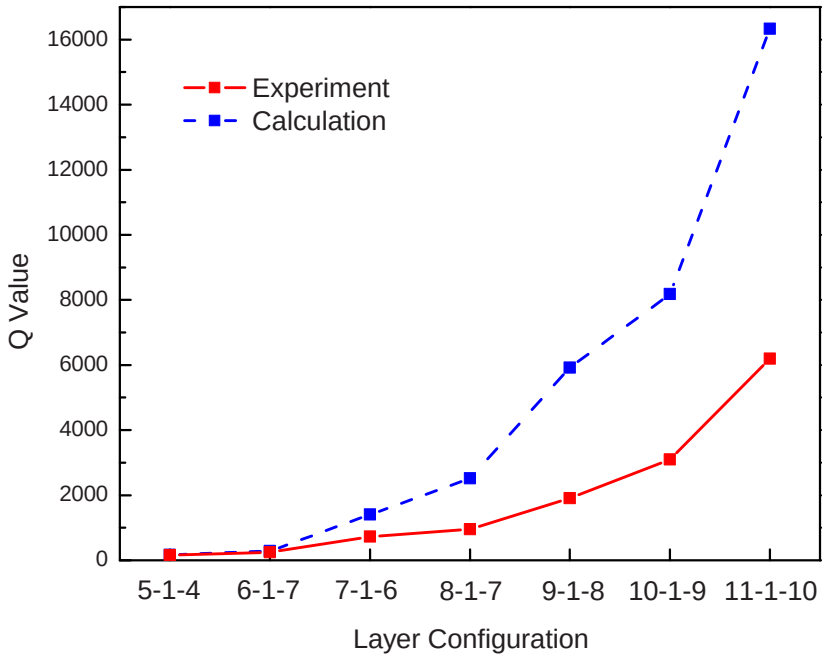


Figure 9-4: Trends in Q values found experimentally (red solid lines with square) and calculated numerically using TMM (blue dotted lines with square): Q value increases exponentially as stacking layers in z-direction increase.

A set of measurements are done to estimate the effect of the sideways loss. It is found that as the cavity moves closer to the edges of the crystal the $Q$ factor reduces almost exponentially. Figure 9-5 shows the $Q$ factor data as cavity moves towards the edge of the crystal for the

22-layered crystal. The red line with squares is the inverse of the measured $Q$ value and the blue line is the exponential increase fit.

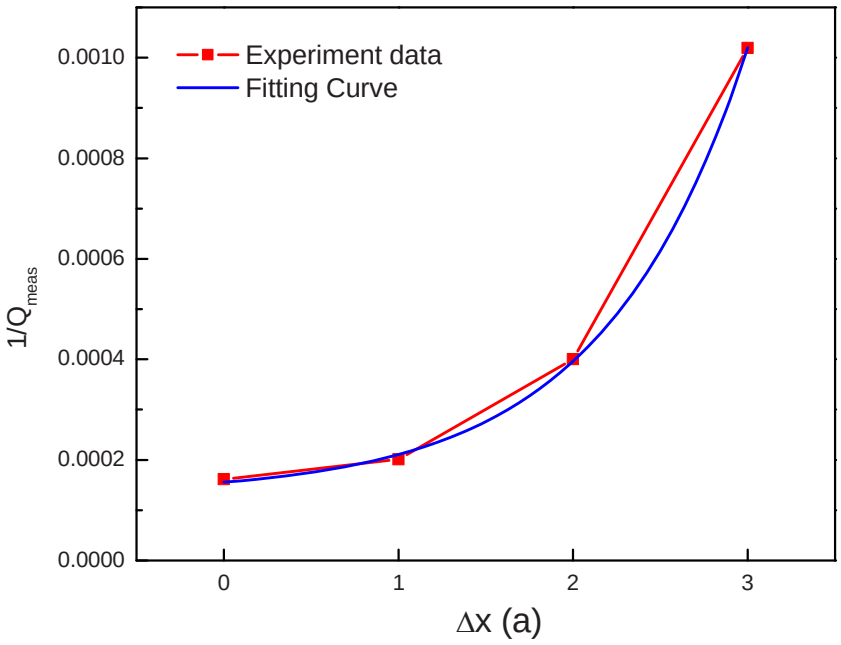


Figure 9-5: The measured Q values decreases exponentially as the cavity is moved closer to the edge of the crystal. $\Delta X$ is the cavity's center position away from the photonic crystal's $XY$ plane's center. The gray line is an exponential decay fitting with fitted result: $Q_{\perp} = 12000$.

Based on Eq. (9.1) with the fitted data, we can get an estimated of $Q_{\perp} = 12000$ which is corresponding to the calculated $Q$ value from TMM. This value is still less than the calculated value of 16000 for this structure but it can be considered a very good match. Loss in the material of the dielectric rods, the mis-alignment in the photonic crystal structure and cavity could be the factors responsible for the lower estimated $Q_{\perp}$.

$$\frac{1}{Q_{meas}} = \frac{1}{Q_{\perp}} + \frac{1}{Q_{//}} \approx A + B \cdot e^{\alpha \cdot \Delta x} \qquad (9.1)$$
$$with: \frac{1}{Q_{\perp}} = A - 2B$$

## 9.3 Effects of cavity size on resonant frequencies

In this section, the cladding layer is fixed to 7-1-6 configuration while the cavity size varies. For microwave experiments, the cavity size is increased from $0.5a$ to $8a$ in steps of $0.25a$. There was no visible mode for a cavity size smaller than $0.5a$. The photonic crystal is very robust regarding the resonant frequencies for microwave experiments. They do not change with slight tilting of the crystal or movement of the horns.

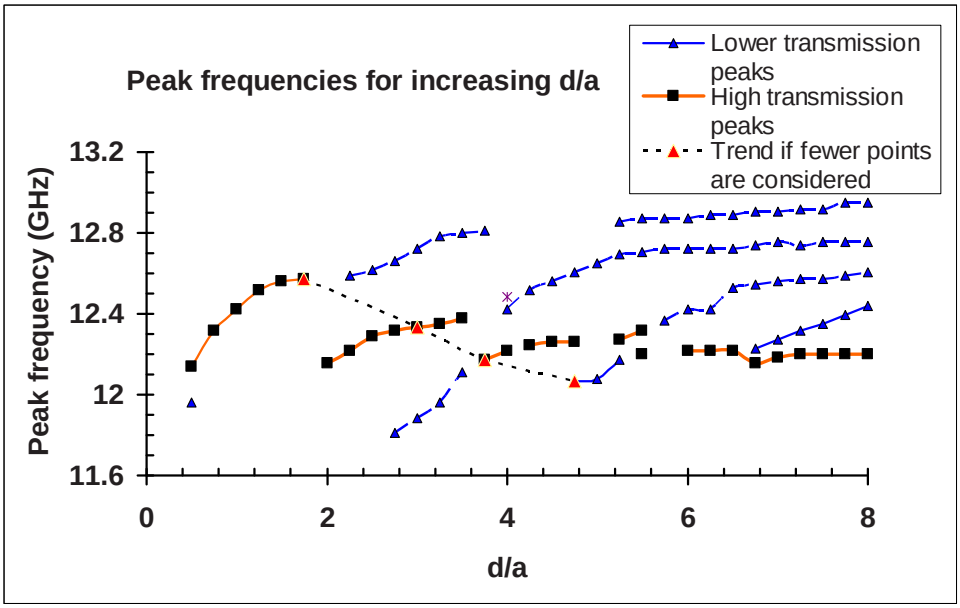


Figure 9-6: Graph showing increasing peak frequencies with defect size. It also shows the diminishing modes and their counterparts arising at a lower frequency and then following the same increasing trend that flattens out for higher cavity sizes. (Courtesy from Preeti Kohli)

The peak frequencies with increasing cavity size do not follow a simple regular pattern. Modes split and reinforce at regular intervals as shown in Figure 9-6. All points in the figure correspond to a resonant peak and points shown in squares are peaks with highest transmission for a particular cavity size. It can be clearly seen that resonant frequencies increase as the defect size increases. Considering defect size increase from $2a$ to $5.5a$ for

example, we can see increasing dominant modes up to defect size $3.5a$ after which the dominant peak shifts to a lower frequency and again starts increasing for size up to $5.5a$.

Before the shifting of the dominant mode at $3.5a$, we can see the new modes arise and becomes dominant gradually. Also as the cavity size increases the rate of increase of resonant frequency reduces and becomes almost flat for defect size close to $7a$. The maximum change in higher transmission peak frequencies on changing defect size from $0.5a$ to $8a$ is only 3.5%. Lower transmission peaks (10-30 db below) vary by 8% over the entire range. The $Q$ values of modes in this configuration range from 500-1000.

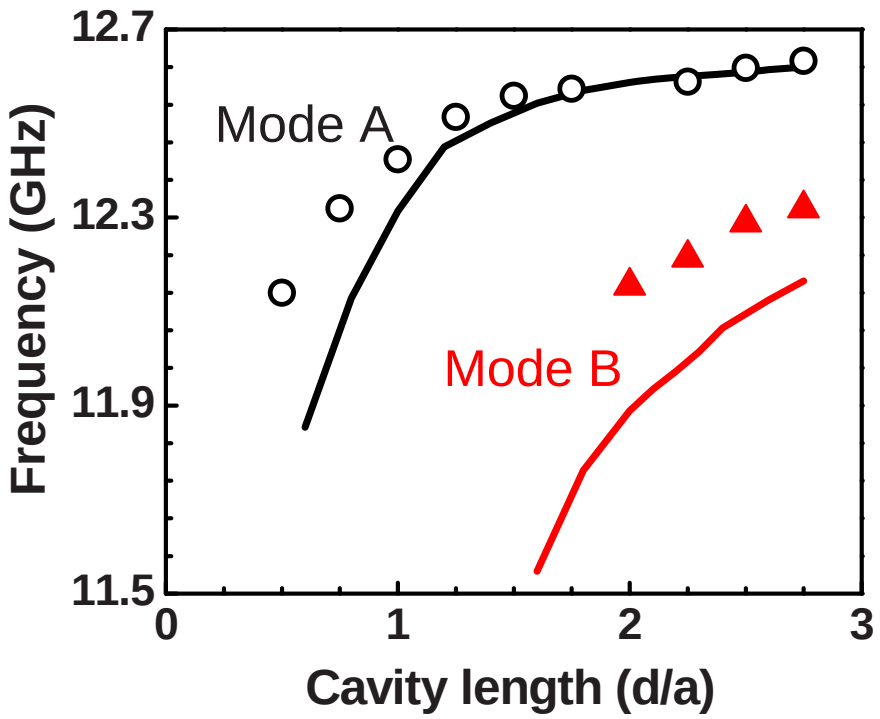


Figure 9-7: calculation results (curves) and microwave experiments (symbols) for increasing cavity size up to $2.8a$: the second mode comes out when the cavity size increases to around $1.6a$, and the trend of TMM calculation agrees well with microwave experiments.

The TMM calculations on the 5 by 5 super cell are done for cavity sizes up to $2.8a$. When the cavity size is larger than $2.8a$, the interference between neighbor cavities are not neglect able due to the periodic boundary condition used in TMM. The trend for frequency increase is same as experiments shown at Figure 9-7. To get a detailed view of the different resonant modes, the electric field mode profiles for those two resonant modes (A and B indicated at Figure 9-7) are plotted at Figure 9-8 for the cavity size of $2a$.

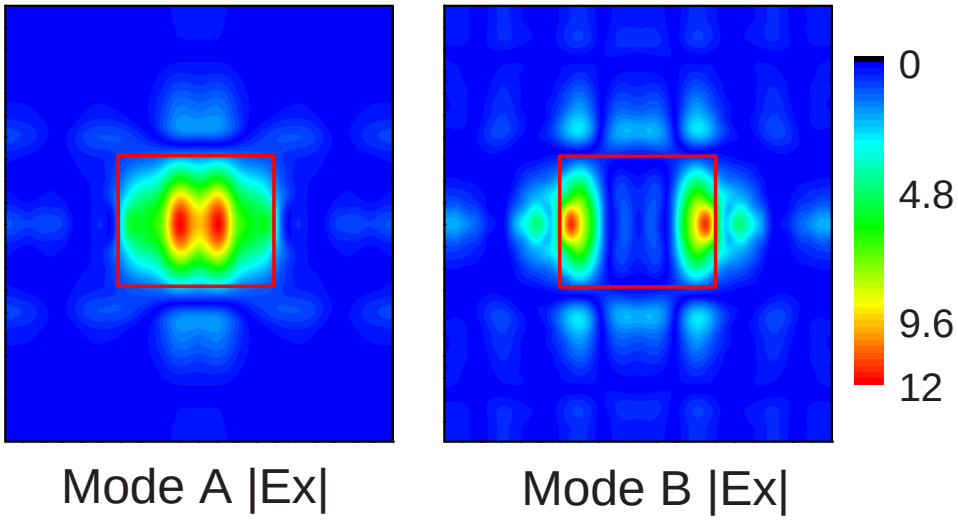


Figure 9-8: Electric field mode profile of two resonant modes with cavity size equals $2a$

An interesting phenomenon should be pointed out for those varying cavity size experiments and calculations. For usual resonant cavity (without the present of photonic crystal as background), the resonant frequency should decrease (or wave length should increase) when the cavity size increases. But with the present of photonic crystal as background, the opposite trend appears: the resonant frequency increases and approaches a constant when the cavity size increased (Figure 9-7) which may due to the interaction of the resonant modes with the photonic crystal background.

**References:**


1. J.D. Joannopoulos, *Photonic crystal – Molding the Flow of Light*, Princeton University Press, 1995
2. K.M. Ho, C.T. Chan, C.M. Soukoulis, R. Biswas and M. Sigalas, "Photonic band gaps in three dimensions: new layer-by-layer periodic structures," *Solid State Commun.* **89**, 413 (1994)
3. E. Özbay, G. Tuttle, M. Sigalas, C. M. Soukoulis, and K. M. Ho, "Defect structures in a layer-by-layer photonic band-gap crystal," *Phys. Rev. B* **51**, 13961 (1995)
4. W. Leung, G. Tuttle, M.M. Sigalas, R. Biswas, K.M. Ho, and C.M. Soukoulis, "Optimizing the Q value in three-dimensional metallic photonic band gap crystals", *J. Appl. Phys.* **84**, 4091 (1998)
5. C. Sell, C. Christensen, G. Tuttle, Z.Y. Li, and K.M. Ho, "Propagation loss in three-dimensional photonic crystal waveguides with imperfect confinement", *Phys. Rev. B* **68**, 113106 (2003)
6. C. Sell, C. Christensen, J. Muehlmeier, G. Tuttle, Z.Y. Li, and K.M.Ho, "Waveguide networks in three-dimensional layer-by-layer photonic crystals", *Appl. Phys. Lett.* **84**, 4605 (2004)
7. P. Kohli, C. Christensen, J. Muehlmeier, R. Biswas, G. Tuttle and K.M. Ho, "Add-drop filters in three-dimensional layer-by-layer photonic crystals using waveguides and resonant cavities", ", *Appl. Phys. Lett.* **89**, 231103 (2006)

# Chapter 10. Future developments and applications of TMM

The planewave based transfer (scattering) matrix method core algorithms (TMM) with spectrum interpolation, higher-order incidence, perfectly matched layer absorption boundary condition, curvilinear coordinate transformation, and active gain material extension have been discussed in the previous chapters. As mentioned in a recently published review article by K. Busch: "there is no single numerical method capable of solving all problems related to periodic nanostructures for photonics".[1] There are many research areas that can not be simulated by TMM. But we can borrow ideas from other fields and try to apply them to our current TMM/GTMM algorithm to extend simulation functions and ability. In this chapter, we briefly discussed what will be the next step expansion of our TMM/GTMM algorithm, and we also briefly predict what areas that photonic crystal concepts can be eventually applied.

## 10.1 Go beyond planewave basis – the localized light orbital

The planewave based transfer (scattering) matrix method is actually a combination of planewave expansion method[2] and real space transfer (scattering) matrix method[3]. To expand the 3D photonic crystal structure into Fourier space by planewave expansion method requires a total planewave number of $N \times N \times N$ which will soon incapable by current computer hardware as $N$ gets larger and larger to simulate more complicated 3D structures. To reduce the 3D structure into 2D structure, the real space transfer (scattering) matrix method slices the whole structure alone the propagation direction. With the idea of "slicing" and the idea of "Fourier expansion", the planewave based transfer (scattering) matrix is introduced to study photonic crystal with total planewave number reduced to $N \times N$. The similar ideas have been introduced in the diffractive optics community as well, where it is called rigorous coupled wave analysis method.

Even with the planewave number reduced to $N \times N$, to study the photonic crystal with defects where super cell is used, the current computer hardware is still limiting. That is the reason why several strategies have been introduced to improve the performance of TMM such as spectrum interpolation. The other limitation of periodic boundary condition assumed by TMM can be compromised by perfectly matched layer absorption boundary conditions. But when comes to disorder systems where much larger super cells are required, our TMM package can not handle them due to both the computer memory limitation and computation time length.

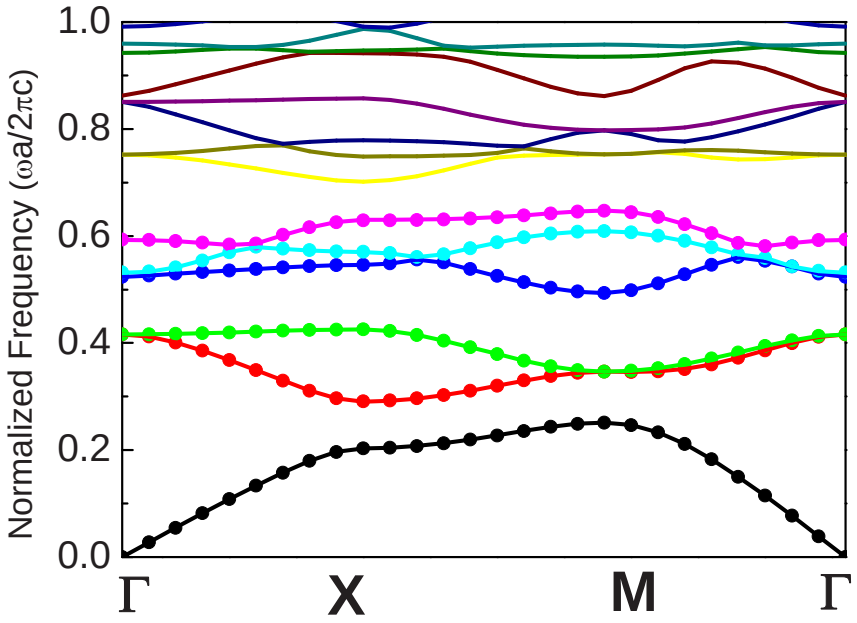


Figure 10-1: The excellent match between band structure generated by localized light orbital basis (dot) and planewave expansion method (solid line) indicates the accuracy of localized light orbital basis.

One solution to above limitation is to replace the planewave basis with more localized basis. Just like in complex electron structure calculations, localized electron orbital is used as basis, we will use the so called localized light orbital as our basis in TMM calculation. Preliminary results have been demonstrated that the localized light orbital is working while there are still

several issues to be tackled. Figure 10-1 shows the band structure of a classical 2D photonic crystal composed by square lattice dielectric cylinders, the localized light orbital basis results agree well with the planewave expansion method.

Similar approaches such as Wannier-function method and Green's function method have been proposed to study localized defects photonic crystal structures (for example: resonant cavity and waveguide).

## 10.2 Future applications of photonic crystal concepts

In the section, various possible applications from photonic crystal concept are discussed, for example: energy saving solution, novel optical instrument, and special light sources. Some of those applications may need several years or decades to become reality, while others are already round the corner to debut into our everyday life.

Energy is a hot topic and also a hard topic in current research. With the consumption of fossil fuel, we are damaging our fragile environments. Global warming is not just a theory; it is already coming to us. Energy is essential to a nation as well as to an individual person. But our current energy source (fossil fuel) is not unlimited and is not clear to our environments either. Photonic crystal devices can play into this area by two means: saving energy and finding alternatives.

One part of the energy consumption is used at everyday light sources, for example household light and traffic light. Currently, the efficiency (ratio of light energy generated to electrical energy used) is very low, for example: less 10% for tungsten filament light and around 20% for halogen bulbs. The rest of the electric energy is used to generate electromagnetic wave with wavelength other than visible light (such as infrared) and eventually turns to heat. We know that photonic crystal can provide a band gap, and no electromagnetic wave within the

band gap can propagate through. One way to apply this idea is to design a photonic crystal thin film with the band gap at the wavelength longer than visible light. Then the thin film can be deposited at the inner surface of the light bulb. For visible light, there will be no effect at all, but all infrared radiations are reflected to the filament and re-absorbed by the filament. By this way, we can recycle those infrared radiations to heat the filament and in turn increases the light bulb efficiency.

Besides increasing the light bulb efficiency, photonic crystal can also be used to improve the light source quality. Human eyes have different response sensitivity to visible light of different wavelengths (or colors). A photonic crystal structure can be designed with the consideration of human eyes response to generate special tailored spectrum for light bulbs. In fact, the tungsten filament with layer-by-layer structure has been reported from Sandia National Laboratory to have the ability to convert heat into light which could raise the efficiency of an incandescent electric bulb from 5 percent to more than 60 percent.[5,6]

Now let’s come to the applications of photonic crystal for alternative energy sources. The ultimate energy source for the earth is from the sun by means of electromagnetic radiation. Direct solar energy is a promising alternative energy source to fossil fuel. But there are still some difficulties for solar cell research and industry, and solar energy currently only accounts a very small portion of total energy consumption. One difficulty lays in the efficiency of the solar cell which is very low in term of the practical application. Or the cost measured in unit of dollar per watt for solar cell is too high and we simply can not afford it. The plants have much better ability to harvest sun light than our solar cells. The photonic crystal can be designed to effectively collect sun light to increase the efficiency of solar cells and in turn drop the cost and make solar energy possible for everyone and everywhere. One proposed idea is to design a film like photonic crystal solar cell which can be painted at the outside the building to provide electricity for the building.

As we discussed at Chapter 7, photonic crystal structures can be used in optics to control the propagation of light just as conventional optical instruments such as optical lenses. One revolutionary idea is to use photonic crystal as conventional lenses to control light, but with better performance and more compact size. The professional photographers usually carry huge cameras, and the major part of those cameras is the lens. To get vivid detail in the picture, a set of conventional lenses must be used to correct the chromatic and other aberrations which make the camera huge and expensive. *Canon* has applied diffractive optics components on its professional cameras to reduce the chromatic aberrations and reduce lenses weight and cost.[7] In the future, the digital camera lenses and projector lenses maybe flat and very compact with the advantage of photonic crystal design.

The concept of photonic crystal can be used in other area to provide special light sources and as waveguide. Low threshold laser may be commercially fabricated within the photonic crystal cavity. Photonic crystal fiber has already in commercially production with its better performance compared with conventional fiber. The ultimate integrated optical circuits maybe achieved one day with the photonic crystal structures as the building block. I believe the 21$^{st}$ century will be a century of photons, and photonic crystal will be a breakthrough in our everyday life.

**References:**


1. K. Busch, G. Freymann, S. Linden, S. Mingaleev, L. Tkeshelashvili, and M. Wegener, "Periodic nanostructures for photonic", *Physics Reports*, **444**, 101 (2007)
2. K.M. Ho, C.T. Chan, and C.M. Soukoulis, "Existence of a photonic gap in periodic dielectric structures", *Phys. Rev. Lett.* **65**, 3152 (1990)
3. J. B. Pendry, "Photonic Band Structures," *J. Mod. Optic.* **41**, 209 (1994)

4. Z. Li and L. Lin, "Photonic band structures solved by a plane-wave-based transfer-matrix method", *Phys. Rev. E* **67**, 046607, (2003)
5. J.G. Fleming, S.Y. Lin, I. El-Kady, R. Biswas, and K.M. Ho, "All-metallic three-dimensional photonic crystals with a large infrared bandgap", *Nature*, **417**, 6884, (2002)
6. http://www.sandia.gov/media/NewsRel/NR2002/tungsten.htm webpage created May 2002, accessed October 2007
7. http://www.usa.canon.com/consumer/controller?act=CanonAdvantageTopicDtlAct&id=2632 webpage accessed October 2007